Photon number resolving systems and instrumentation

Mala Sadik

Doctor of Philosophy (PhD)

Aston University

September 2022

M. Sadik, PhD, Thesis, Aston University, 2023

Abstract

Time correlated single photon counting (TCSPC) is a technique used in many applications such as light detection and ranging, quantum key distribution, medical imaging and more. One inherent problem of this technique is the 10% limit on the detector count rate to avoid distortion in measurements caused by the pile up effect. Essentially, when a conventional single photon avalanche photodiode (SPAD) detects a photon, it is unable to see another photon until its deadtime completes, which gives rise to early photons having a higher probability of detection if the probability of detecting a photon is too high.

Photon number resolving detectors offer an alternative to SPAD and be thought of as a two dimensional array of passively quenched SPADs with the outputs summed together. Such detectors offer photon number resolving capabilities (the output pulse amplitude is proportional to the number of incident photons) as each photon will land in a different place in the two-dimensional array. This comes at the expense of increased noise, as the dark count of all detectors will be present on the output in addition to other problems such as optical cross talk.

This might preclude such detectors from quantum experiments, but such detectors could offer significant advantages in LiDAR systems, where extended dynamic range and photon number resolving capabilities could increase the acquisition rate by collecting more light and by allowing such systems to operate at higher mean photon levels.

In this work silicon photomultipliers are characterised for their number resolving capabilities and used in photon counting. The SiPMs are shown to have capable single photon sensitivity and can resolve the photon number. Subsequently, a novel real-time instrument has been developed to acquire data. Finally, a comparison has been made between SiPM and SPAD LiDAR, showing that SiPMs can retrieve more photons per excitation pulse and offer greater dynamic range.

M. Sadik, PhD, Thesis, Aston University, 2023

Acknowledgements

I acknowledge that this thesis took a long time to write.

Table of Contents

M. Sadik, PhD, Thesis, Aston University, 2023

M. Sadik, PhD, Thesis, Aston University, 2023

List of Abbreviations

ADC	Analog to Digital Converter
ASIC	Application Specific
CPLD	Complex Programmable Logic Device
CSV	Comma Separated Values
DAC	Digital to Analog Converter
DAPD	Discrete Amplification Photon Detector
DLL	Delay Locked Loop
DNL	Differential Non Linearity
DOT	Diffuse Optical Tomography
ECL	Equivalent Coding Line
FIFO	First In First Out
FLIM	Fluorescence Lifetime IMaging
FPGA	Field Programmable Gate Array
FWHM	Full Width Half Maximum
INL	Integral Non Linearity
I/O	Input/Output
IRF	Instrument Response Function
LiDAR	Light Detection and Ranging
LUT	Look Up Table
LVDS	Low Voltage Differential Signalling
MEMS	Micro Electromechanical System
ND	Neutral Density
OCXO	Oven Controlled Crystal Oscillator
PCB	Printed Circuit Board
PDE	Photon Detection Efficiency
PET	Positron Emission Tomography
PLL	Phase Locked Loop
PMT	Photomultiplier Tube
PVT	Process, Voltage and Temperature

QKD	Quantum Key Distribution
SCDT	Statistical Code Density Testing
SiPM	Silicon Photomultiplier
SNR	Signal to Noise Ratio
SPAD	Single Photon Avalanche Diode
SPD	Single Photon Detector
SSP	Single Shot Precision
TAC	Time to Amplitude Converter
TCPC	Time Correlated Photon Counting
TCSPC	Time Correlated Single Photon Counting
TDC	Time to Digital Converter
ToF	Time of Flight

List of Figures

M. Sadik, PhD, Thesis, Aston University, 2023

M. Sadik, PhD, Thesis, Aston University, 2023

M. Sadik, PhD, Thesis, Aston University, 2023

List of Tables

M. Sadik, PhD, Thesis, Aston University, 2023

1.0 Introduction

1.1 Background

Time correlated single photon counting (TCSPC) is a widely used technique to statistically measure optical waveforms in applications including those of light detection and ranging (LiDAR), fluorescent lifetime imaging (FLIM), quantum key distribution (QKD), and diffuse optical tomography (DOT). Due to its nature being a statistical measurement, TCSPC requires recording many events before the measurement can be deemed statistically valid. Traditionally any detector capable of detecting a single photon can be used with TCSPC with the single photon avalanche diode (SPAD) being an especially popular choice.

In recent years, detector arrays based off SPAD technology called silicon photomultipliers (SiPMs) have started to be used more widely especially in applications of FLIM. These detectors consist of a passively summed SPAD array and due to this structure, they are capable of photon number resolving. They provide information on both the time of arrival and the number of photons in an event. The concept of TCSPC provides limitations on the number of photons able to be detected within a single excitation pulse due to dead time limitations of single photon detectors. However, for an array-based photon number resolving detector such as the SiPM, dead time effects are less apparent, as each incident photon is likely to land on a different part of the array, which is not currently recovering from a break down. Modifications to the TCSPC technique are presented to take advantage of photon number resolving detectors, resulting in the time correlated photon counting (TCPC) technique, which overcomes the limitations posed by traditional SPAD based setups.

The aim of this thesis is to experimentally verify whether there is a benefit in using TCPC with a photon number resolving detector over traditional TCSPC.

1.2 Structure of the thesis

Chapter 2 provides a review of the fundamental concepts relating to the work undertaken in this thesis. Firstly, an overview of time to digital converters (TDCs) is given along with methods for implementing and characterising TDCs. TDCs form the basis of most modern-day photon

counting instruments [1-3] and are used to timestamp when a photon arrives. The concept of time correlated single photon counting is reviewed along with the issues with the technique and mitigation methods. From this, a comparative overview of single photon detectors is provided with a focus on performance metrics. Finally, an introduction into various light detection and ranging (LiDAR) systems is provided as it was the original target of this work, to exploit photon number resolving detectors to increase the acquisition speed of LiDAR systems.

Chapter 3 explores the work undertaken to characterise an onsemi MicroRB-10035 SiPM at a range of overvoltages to provide an insight into its photon number resolving capabilities. Details of the hardware developed for this task are given. The noise in the detector has been characterised along with its performance in TCSPC when used with varying levels of light. Finally, the amplitudes of the SiPM pulses are analysed for use in multi photon detection. The impact of filtering the detector's output is also analysed to ensure that multi photon events can be easily resolved.

Chapter 4 details the development of a novel real time TCPC system for photon counting applications using photon number resolving detectors. The instrument is implemented on a field programmable gate array (FPGA) with additional circuitry used for the quantisation of the input signal's amplitude. A performance review of the system is given along with an initial experimental comparison between TCSPC and TCPC when using a SiPM with the instrument.

In chapter 5 an experimental comparison between SiPMs and SPADs is provided in applications of photon counting LiDAR. The results of the comparison between the TCPC measurements with the SiPM and TCSPC with the SPAD and the SiPM are presented, analysed, and discussed.

2.0 Literature review and technical background

2.1 Time-to-digital converters

Time to digital converters (TDCs) are instruments used to measure the time difference between events, typically the rising edges of signals denoted as START and STOP. They are used in several applications, including those of time correlated single photon counting (TCSPC) [4, 5], Quantum key distribution (QKD) [6-8], Light Detection and Ranging (LiDAR) [9], Positron Emission Tomography (PET) [10, 11], Digitals Phase Locked Loops (PLLs) [12] and Fluorescence Lifetime Imaging Microscopy (FLIM) [13, 14].

2.1.1 Implementation options

One of the first things to consider when designing a time-to-digital converter is the architecture to be used for implementation. While various methods for measuring time in a digital circuit exist, they each come with their own advantages and disadvantages in terms of cost, precision, and design flexibility. The goals of this research require a TDC with a time resolution in the picosecond (ps) range at a suitable cost with a short turnaround time. In addition to this, the implementation choice needs to be user programmable, to allow for signal processing etc to be undertaken in hardware. Taking this into consideration, the following options of implementation are presented:

- Complex Programmable Logic Device (CPLD): A low-cost type of field programmable logic device that is constructed of AND/OR gates [15]. They are configurable and suited for time-critical applications. However, they possess a low capacity of logic resources which would not serve the requirements of this work.
- Field Programmable Gate Array (FPGA): FPGAs were chosen as the implementation option for the TDC in this work. They offer a considerable upgrade over CPLDs in terms of the number of resources they have while still offering a relatively low cost. A more in-depth overview of FPGAs and their use for implementing TDCs are detailed further on in this section.
- Application Specific Integrated Circuit (ASIC): ASICs offer the best potential performance as there is a greater amount of control over a logic design. However, they are costly to design and manufacture with considerable turnaround times.

Because of this, ASICs are deemed not suitable for this work and not discussed any further.

FPGAs are programmable logic devices consisting of a two-dimensional array of interconnected user-programmable logic blocks and I/O circuitry. These logic blocks can route signals to any other logic block or I/O circuitry using switch matrices placed adjacent to each block. Inside each logic block is two slices, with each slice containing four Look-Up Table(s) (LUT), eight flip-flops and a carry chain connected through multiplexers and XOR gates. The carry chain is normally used for arithmetic circuits, and it provides a vertical signal path going through all slices in a particular column. FPGA-based TDCs in the literature typically make use of the carry chain in their implementation, treating them as non-inverting buffers (discussed further in section 2.1.3.2).

2.1.2 Time to amplitude conversion

Traditionally, a combination of analogue and digital circuitry has been used to implement precise time to digital conversion, with two methods being prevalent [16]. The first of these methods is the time expansion or time amplification technique [16-19] shown in Figure 1.
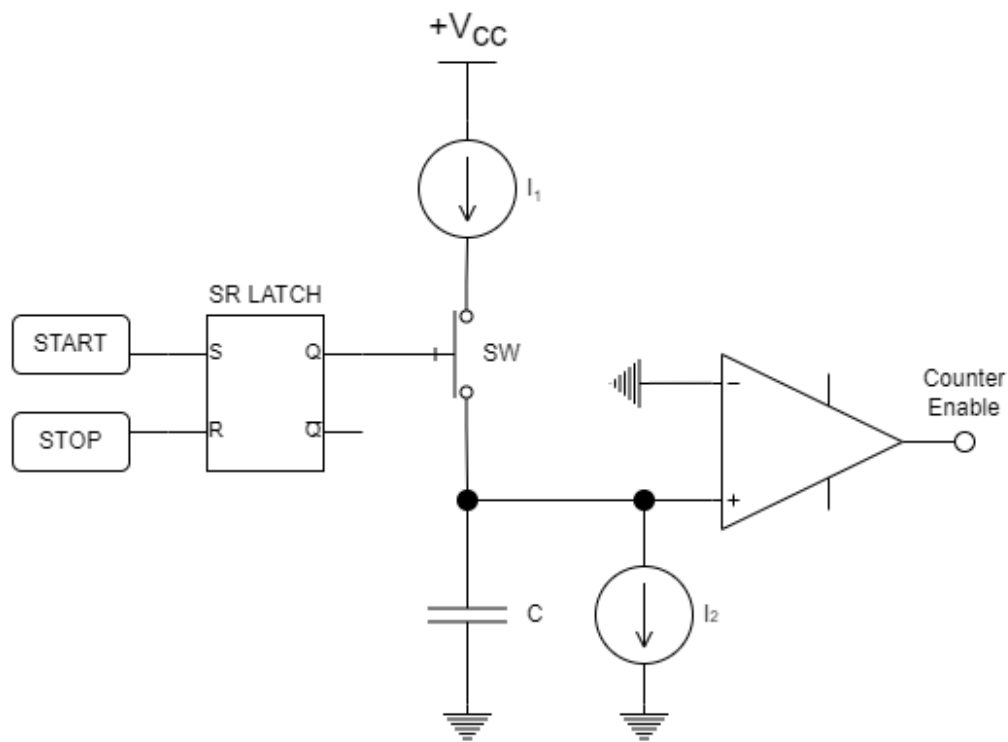
Figure 1 Time expansion TDC

4

During the time interval $T = T_{START} - T_{STOP}$, a capacitor C is charged using a constant current source I_1 as the current is drained by a much smaller constant current sink I_2 such that $I_2 \ll I_1$. This method stretches out the discharging time of the capacitor by $T_r = TK$, where the stretching factor K is defined as

$$K = \frac{I_1 - I_2}{I_2} \tag{2.1}$$

A comparator then enables a simple counter for the duration of $T + T_r$ which provides an effective resolution of $LSB = T_0/(K + 1)$ with T_0 being the period of the counter. With a count number of n, the time difference can then be calculated as $\Delta T = n \cdot T_0/(K + 1)$.

A different method for time resolution using a mix of digital and analogue circuitry is the time-to-voltage conversion or time-to-amplitude conversion (TAC) [20, 21]. In this method, the time is first converted into voltage in the capacitor by linearly charging it with a constant current source for the time $\Delta T = T_{START} - T_{STOP}$. The voltage is then held until an analogue to digital converter (ADC) can be used to read the voltage across the capacitor. A simplified diagram depicting a TAC can be seen in Figure 2.
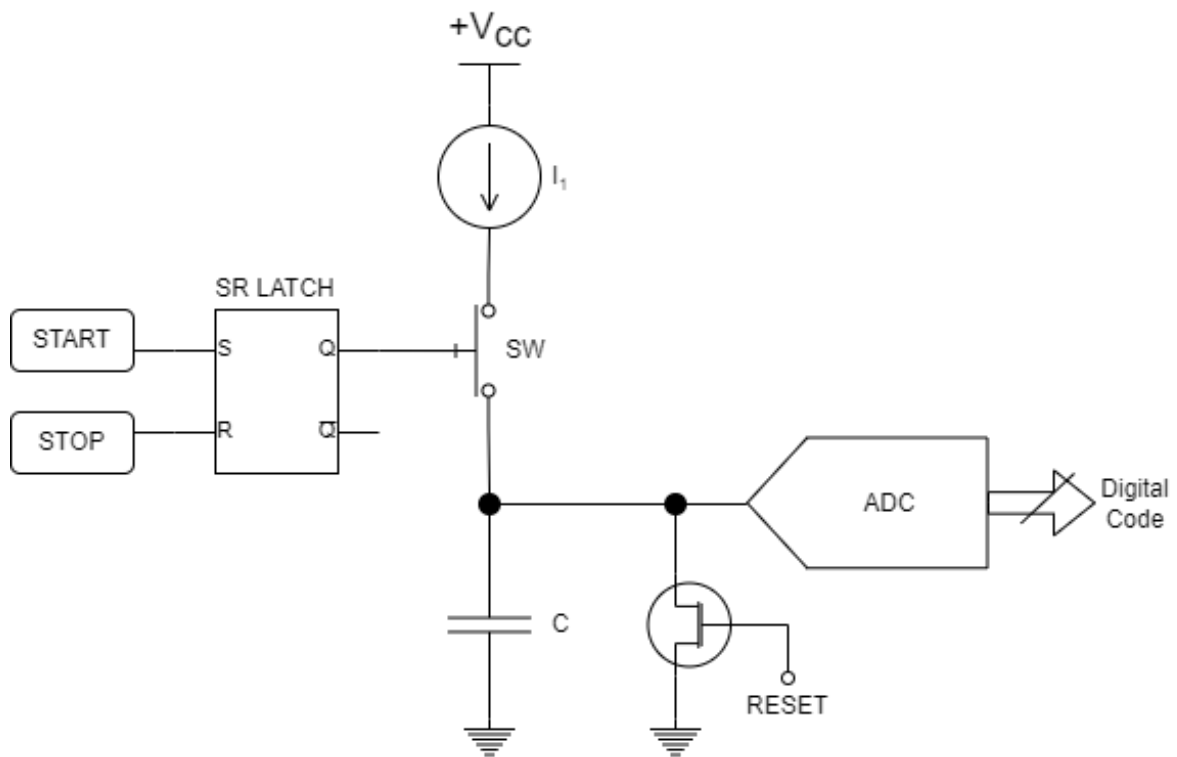
Figure 2: Time to amplitude converter simplified circuit

M. Sadik, PhD, Thesis, Aston University, 2023

The voltage across the capacitor, in this case, is proportional to the time interval as defined by:

$$V = \frac{T}{C} \cdot I \tag{2.2}$$

2.1.3 Digital time measurement

The work conducted in this thesis makes use of FPGA-based TDCs, due to their flexibility and relative speed of development in comparison to custom analogue circuits. Therefore, the focus will be given to methods of digital time measurement/TDC implementations using FPGAs.

2.1.3.1 Counter

The simplest way of measuring time in a digital circuit consists of a counter that counts the number of clock cycles between 2 events happening. This method is limited by the clock speed of the measurement device as it only registers events that occur after a clock pulse in the next clock cycle. The measurement uncertainty for such a system is equal to $\pm T_{CLK}$ [22]. To increase the time resolution of a TDC using the counter method would require increasing the clock speed of the system. Another way is to use a separate counter that is clocked on the opposite edge of the clock giving a measurement uncertainty of $\pm 1 \frac{T_{CLK}}{2}$. For example, in a counter based TDC, a clock speed of 1GHz gives a time resolution, meaning the smallest change in the time it can detect, of 1ns. Whereas a dual counter based TDC with the same clock speed would achieve a resolution of 500ps.

2.1.3.2 Delay-line based time to digital converters

A commonly used method for making TDCs on an FPGA is the delay line method [23-30]. In this method, a chain of non-inverting buffers with fixed propagation delays is used in the signal path to provide a delayed input to flip flops. An example of this is shown in Figure 3, where the input passes through the chain of buffers into the respective D input of a D-type flip flop for the corresponding sampling bin, with the clock being distributed to all the flip flops at the same time.
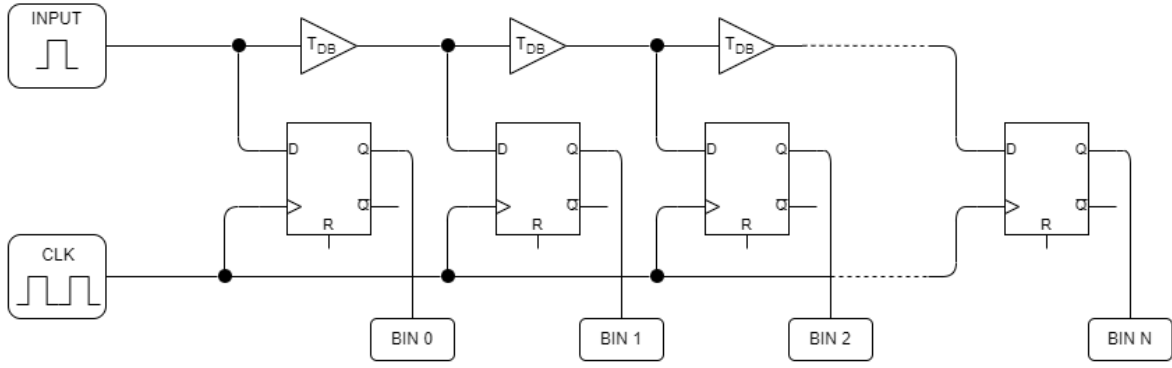
Figure 3: Diagram of Single delay line TDC showing the buffers used as delay elements on the input signal before each sampling bin

At each sampling bin, the input is delayed by $B \times T_{DB}$ where T_{DB} is the buffer delay and B is the bin number. For the delay line to cover the clock period T_{CLK} the number of sampling bins required is $N \geq T_{CLK}/T_{DB}$. The outputs of the flip flops in each clock cycle are used as a N-bit vector, commonly known as thermometer code [30], to determine the rising edge transition of the input with respect to the sampling clock edge. This bit vector is normally passed through a priority encoder to encode the transition position in a vector of size $log_2(N)$ bits rather than N bits.

In FPGA fabric, the carry chain is often used as the non-inverting buffers in the delay line [31, 32] with resolutions as low as 10 ps being possible [33]. However, the carry chain comes with its own problems as it introduces non-linearities in the delay line [33]. This is caused by "ultra-wide bins", where the propagation delay between the carry chain elements within SLICES of the FPGA is much shorter than the propagation delay between SLICES. Each SLICE in an Artix 7 FPGA has 4 carry chain elements that can be used for the delay line. The impact of these can be partially mitigated by using methods such as averaging (section 2.1.6.1) or wave union (section 2.1.6.2) to improve the linearity.

2.1.3.3 Vernier delay lines

Vernier delay lines use a technique which is like that of single delay lines where the input goes to a chain of flip flops through a series of non-inverting buffers. However, to achieve resolutions smaller than that of the buffer delay T_{DB}, vernier delay lines introduce a series of buffers on the clock signal as well, which puts a delay of T_{CB} in the clock path where $T_{DB} > T_{CB}$ [16, 34]. An

example of this is shown in Figure 4. The resolution of this system is now determined by $T_{RES} = T_{DB} - T_{CB}$. Because of this, the number of sampling bins required to cover the clock period also increases and is now determined by $N = \frac{T_{CLK}}{T_{DB} - T_{CB}}$.
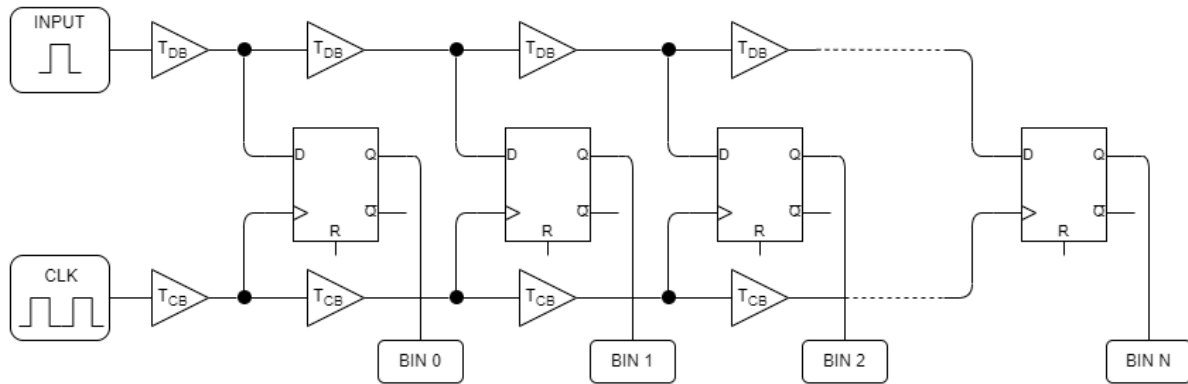
Figure 4: Diagram of Vernier Delay Line TDC showing the buffers used as delay elements for both the input signal and clock signal before each sampling bin where T_{CB} > T_{DB}

This means the number of resources required to implement a vernier delay line are also greater. In a FPGA the size of the buffer delays is difficult to control [35], this along with the impact on resolution due to routing delays introduced by the FPGA make implementing a vernier delay line on a FPGA difficult.

2.1.3.4 Vernier oscillators

Vernier oscillators utilise the same principle as vernier delay lines, however, to mitigate the large resource requirement of the vernier delay line, vernier oscillators use two controllable oscillators with close but dissimilar frequencies F_1 and F_2 where $F_1 < F_2$ [16, 36]. The resolution is determined by $T_{RES} = T_1 - T_2$ where $T_1 = F_1^{-1}$ and $T_2 = F_2^{-1}$. A simplified example of a vernier oscillator system is shown in Figure 5.

M. Sadik, PhD, Thesis, Aston University, 2023
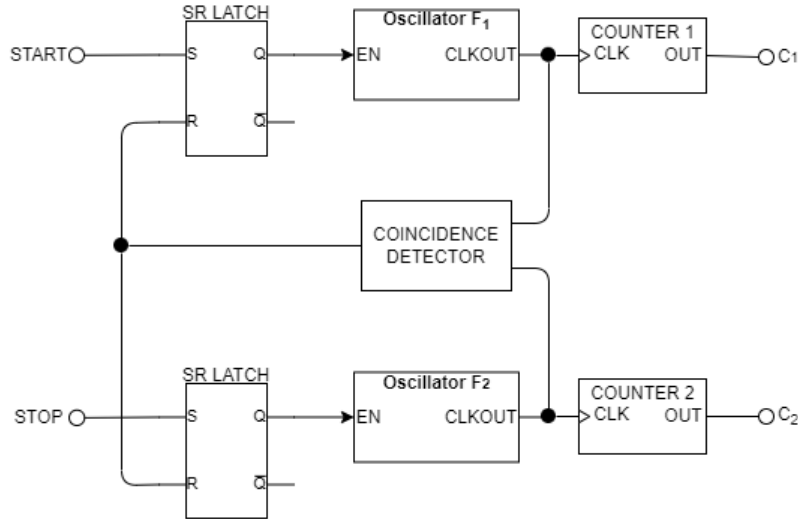
Figure 5: Diagram of Vernier Oscillator TDC structure showing two SR latches that enable/disable oscillators controlled by the START and STOP signals with F₁ < F₂. The oscillators drive separate counters to measure the time for each signal with the latches being reset by a coincidence counter looking for coincidences in the positive going clock edges of the oscillators. Once the SR latch is reset and the oscillators are disabled, the counter values are read out and converted in to the ΔT of the measurement.

The START and STOP inputs are routed to SR latches whose outputs turn the oscillators on and off. The oscillator outputs when turned on drive counters C_1 and C_2, enabling them to increment at rates of F_1 and F_2 respectively. The two oscillator outputs also go into a coincidence detector that looks for coincidences in the positive going clock edges. At some point after the STOP pulse has arrived, a coincidence between rising edges will be found, which resets the SR latches, which in turn stops the oscillators and the counters. At this point the time difference can be calculated as per:

$$\Delta T = (C_1 - 1) \cdot T_1 - (C_2 - 1) \cdot T_2 \qquad (2.3)$$

While a vernier oscillator based TDC can be implemented in a FPGA and achieve small resolutions, this comes at the cost of a long dead time with [37] reporting a resolution of 1.58ps with a dead time of 598ns. Despite offering good resolution, the dead time is the key problem with vernier oscillator based TDCs as it is a digital time expansion technique. A dead time of 598ns would limit the usable count rate to 1.67 MHz, assuming all input edges land in subsequent measurement cycles.

2.1.3.5 Nutt Interpolation

Interpolation is commonly used in high time resolution TDCs to increase their measurement range. Nutt interpolation, which was first mentioned in [38], does this by combining a coarse counter driven by the reference clock with a fine time digitizer such as a delay line that covers the system's clock or longer. A simplified diagram showing how Nutt interpolation works is shown in Figure 6. When an input arrives on the START channel, a fine time digitizer is used to measure the time T_{START} of the input with respect to the next rising edge of the system clock and at the same time, a counter driven by the system clock is started.
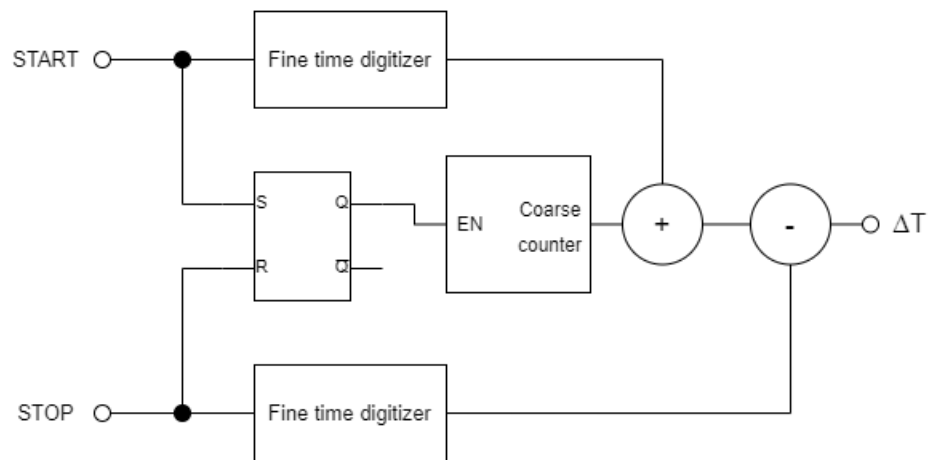
Figure 6: Block diagram of Nutt Interpolator showing the fine time digitizers on the inputs that can measure times smaller than the system clock being used to measure the time of the input with respect to the next rising edge of the system clock and a coarse counter driven by the system clock that is used to increase the measurement range.

When an input on the STOP channel arrives another fine time digitizer is used to measure the time T_{STOP} with respect to the next rising edge of the system clock and the counter is stopped. The coarse time T_{COARSE} is equal to the product of the resultant counter value and system period T_{CLK}. Once the outputs of the fine time digitizers and the coarse counter are known, the time difference between START and STOP can be calculated from:

$$\Delta T = T_{START} + T_{COARSE} - T_{STOP} \tag{2.4}$$

M. Sadik, PhD, Thesis, Aston University, 2023

The majority of FPGA delay line based TDCs make use of coarse (clock counter) and fine time (delay line) interpolation to combine the resolution of the delay line with the measurement range of a counter [28, 29, 39].

2.1.4 Time to digital converter performance metrics

To properly determine the resolution, accuracy, and linearity of a TDC, several metrics of the TDC must first be characterised. These metrics along with their uses are detailed in the following sections.

2.1.4.1 Accuracy, Resolution, offset error, and gain error

The resolution of a TDC is the smallest change in time that a TDC can detect and is dependent on the architecture of the TDC used. The accuracy of a TDC is defined as the difference between the measured value from the actual value. Offset error in a TDC refers to the shifting of the transfer function. Gain error is defined as the full scale error minus the offset error [40] as shown in Figure 7. The full scale here is measured at the last TDC bin on the transfer function curve and compared against the ideal transfer function.
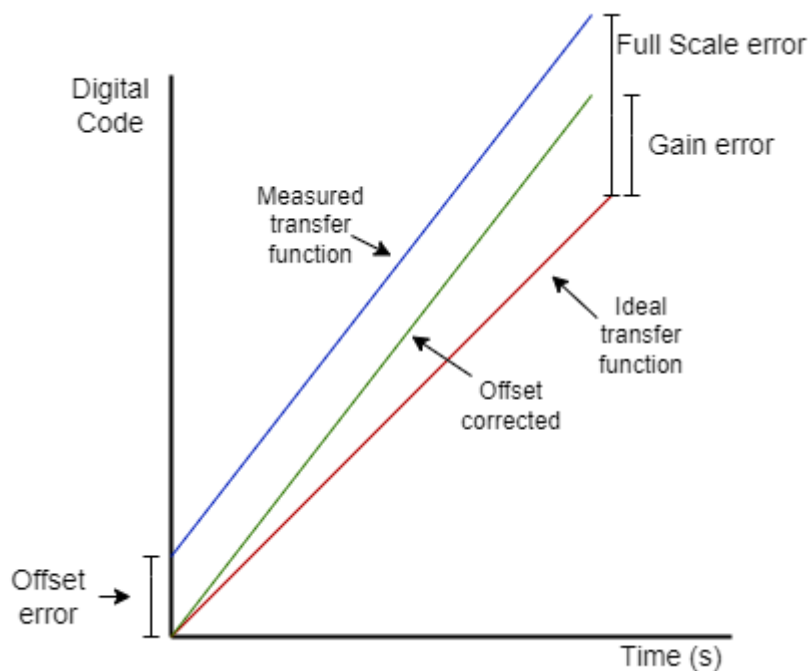
Figure 7: Diagram showing offset, gain and full scale error from the ideal transfer function

2.1.4.2 Single-Shot Precision

Single-shot precision (SSP) is defined as the standard deviation of the measurement results when measuring a constant time interval [14] and gives an insight into the TDCs capability to accurately time stamp any input. To determine the SSP of a TDC, an autocorrelation can be performed where an input signal is presented to both the START and STOP inputs of the TDC via a power splitter to match impedances. The full width at half maximum (FWHM) of the resultant gaussian distribution is directly proportional to the SSP of the TDC such that $FWHM = 2\sqrt{2\ln 2} \cdot \sigma$ or $FWHM = \sim 2.35 \cdot \sigma$. In the literature, the SSP may be quoted in terms of either standard deviation or FWHM.

2.1.4.3 Differential non-linearity

Differential non-linearity (DNL) and integral non-linearity (INL) are quantitative measurements of a converter's linearity [41-43] with respect to ideal and are also known as dynamic converter errors, as the error is not constant across the converter's transfer function. Linearity errors can lead to distortion in the measurement results of a converter and therefore should be kept to a minimum. DNL is the measurement of the deviation of a converter's bin size for a particular bin from the ideal bin width, T_{LSB}. The DNL of a particular bin i can be calculated from the measured bin width T_B as in:

$$DNL(i) = \frac{T_B(i)}{T_{LSB}} - 1 \tag{2.5}$$

2.1.4.4 Integral non-linearity

INL is the deviation of a converter's actual transfer function from ideal. The ideal transfer function should be a linear line. The INL represents the bin specific deviation from this ideal line where the non-linearity of bin i is the sum of all previous DNL errors as shown in:

$$INL(i) = \sum_{k=0}^{i} DNL(k) \tag{2.6}$$

M. Sadik, PhD, Thesis, Aston University, 2023

2.1.5 Delay line calibration

2.1.5.1 Direct calibration

One approach to delay line based TDC calibration involves using a variable precision delay generator to iteratively characterise the bin widths in the delay line. The variable delay generator must have a resolution smaller than that of the least expected bin size for this method to be viable as well as be able to cover a range greater than that of the clock period T_{CLK}. A signal that is phase referenced to the system clock and slow enough to be used as an input to the TDC can be generated from a counter. This signal can then be passed through to the input of the variable precision delay generator and from there to the input of the TDC. Once the system is setup the calibration process can begin. First the variable delay is slowly increased until a transition to the next bin occurs, then the bin width is found by taking the difference between the time of the transition to the next bin and the starting point. This process is repeated until the entire delay line has been characterised, at which point the measured bin widths can be used to calculate the linearity errors of the TDC. This approach to delay line characterisation may prove to be difficult with a high resolution TDC as variable delay generators are limited in their resolution and a costly addition to the system. In addition to this, signal jitter will also make finding the precise bin boundaries more difficult, although a statistical approach could be taken. For a high resolution TDC a statistical method of characterisation as discussed in the following section may be more suitable.

2.1.5.2 Statistical code density testing

Statistical code density testing (SCDT) is a method used to characterise the linearity of a converter with high precision using statistical analysis. Although originally used as a means of characterising the linearity of ADCs [44], SCDT has since been adapted to be used to calibrate and characterise digital delay line based TDCs [35, 45].

The SCDT is performed assuming that all the bins in the converter are ideal and have an equal bin width of $T_{CLK} \div N$, where N is the number of bins and T_{CLK} is the clock period. An independent clock source is presented to the input of the converter with a frequency F_{CAL} that is asynchronous to the system clock. In an ideal converter every bin is expected to have an equal likelihood of

M. Sadik, PhD, Thesis, Aston University, 2023

experiencing a bin hit, hence a histogram of the resultant bins should ideally be a uniform distribution. However, in non-ideal conditions, larger bins are more likely to experience a hit and therefore will appear more often in resultant histograms. The bin width of bin i is directly proportional to the bin count in the resultant histogram as shown in equation (2.7) where $W(i)$ is the bin width in seconds, $H(i)$ is the bin count in the histogram, and Y is the total number of hits used in the histogram.

$$W(i) = \frac{H(i) \cdot T_{CLK}}{Y} \tag{2.7}$$

The measured bin widths can then be used to calculate the DNL and INL of the converter as shown in section (2.1.4). Because SCDT is a statistical measurement a minimum number of hits are required for the result to be statistically valid. In [46] the author derives the following equation to determine the number of bin hits required for a certain tolerance to be:

$$Y \geq \left(\frac{z_{\frac{\alpha}{2}}}{\beta}\right)^2 \cdot (N - 1) \tag{2.8}$$

where $z_{\alpha/2}$ is the area under the standard normal distribution curve of $\alpha/2$, β is the tolerance and N is the total number of bins in the converter.

2.1.6 Field programmable gate array delay line time to digital converter improvement techniques

2.1.6.1 Averaging

One way to improve a TDC's precision without affecting dead time is the averaging method. The averaging TDC makes use of multiple delay lines running in parallel with the input signal going to the input of all the delay lines [47, 48]. Their outputs are then calibrated and averaged in post processing to give the result. Using this method there is a noticeable improvement in resolution and precision of the TDC over a single delay line based TDC. Improvement will be proportional to $\sqrt{N}$, with N being the number of delay lines used.

Code density calibration is used to determine each delay line's transfer function such that a specific hit can be converted into a time of $B(m, i) \rightarrow T(m, i)$, where B is the bin for a particular

delay line i and T is the time for the particular bin of delay line i. Each calibration lookup table for the delay lines also contains an offset for each delay line which is added during the calibration stage. This is done to mitigate the relative delay shifts between the delay lines. The offset is obtained with respect to delay line 0 by applying a series of random pulses to the converter.

While the averaging method provides a noticeable improvement in the TDC performance it tends to be resource heavy and therefore may not be a viable option for many applications. Each delay line used for the averaging TDC can be thought of as an independent TDC and therefore instead of one TDC with improved performance it may be more appropriate to implement a TDC with multiple channels with the same basic performance of a single delay line. Despite the advantages, this method is not FPGA resource efficient and using the technique will limit the number of timing channels that could be fitted within an FPGA.

2.1.6.2 Wave union

The wave union method is a technique used to improve the resolution and linearity of delay line based TDCs that are implemented on FPGAs. Fundamentally, it operates by performing multiple measurements on an input rising edge in a singular delay line. On FPGAs, there is no way to control the delay propagation presented by the delay buffers used which means that each buffer will have a different delay time due to process, voltage, and temperature (PVT) differences. In addition to this, carry chain based TDCs on FPGAs also suffer from a phenomenon known as ultra-wide bins where the propagation delay between slices is far greater than the propagation delays within the slice. The wave union approach initially introduced in [33] consists of two separate methods both aiming to improve the performance of the FPGA delay line with different trade-offs. The two methods are outlined below.

Method A

The wave union method A presents a pattern of multiple edges into the carry chain delay line. This is achieved by storing three rising edge transitions prior to running the delay line and then waiting for the rising edge of the input to trigger the stored transitions to propagate through the delay line. In a conventional delay line, the edge position is used to determine the time of the input pulse relative to the clock edge, however, in the wave union method A two edge positions are generated which are then summed together. The pattern being propagated is designed such

that the separation between the edges is greater than that of the ultra-wide bins. With this the ultra-wide bins are sub divided and the linearity of the converter is improved as the two rising edges of the pattern are unlikely to both land on ultra-wide bins at the same time. A code density calibration can then be done to convert the summed bin codes into time. The original author demonstrates an improvement in the linearity, resolution and SSP using this method. The linearity is improved from 1.75 to 1.17, the resolution improved from 60ps to 30ps, and the SSP went from 40ps to 25ps RMS. This method increases the dead time of the TDC by one clock cycle.

Method B

Method B provides further performance improvements over method A but at the cost of an increased dead time. The pattern launcher from method A is replaced with a controllable ring oscillator which is controlled by the input signal. This gives the ring oscillators output a phase relationship with the input, which is essential to determine the timing information. The ring oscillator is designed such that it oscillates at a frequency slightly greater than that of clock period. An N_{CAP} number of edge transitions are captured within each successive clock cycle where each cycle contains a single rising edge transition produced by the ring oscillator [49]. The original author demonstrated an improvement of the SSP from 40ps to 10ps using method B with $N_{CAP} = 16$, as well as presenting an effective bin width of 2.44ps. However, the dead time was increased from 2.5ns of a plain carry chain TDC to 45ns when using the wave union method B.

2.1.6.3 Equivalent coding line

The equivalent coding line (ECL) is another method of combining multiple delay lines inside an FPGA to improve the performance using post processing [50, 51]. Multiple delay lines are created inside an FPGA and characterised. Their characterisation transfer functions are then used to acquire the bin widths in the clock period T_{CLK} and are denoted as $W_1(i)$ to $W_M(i)$, with M being the number of delay lines being used. Although created equally, each delay line built using the FPGA carry chain can be considered independent from the other lines. This is due to PVT variations creating inherent differences within the FPGA fabric.
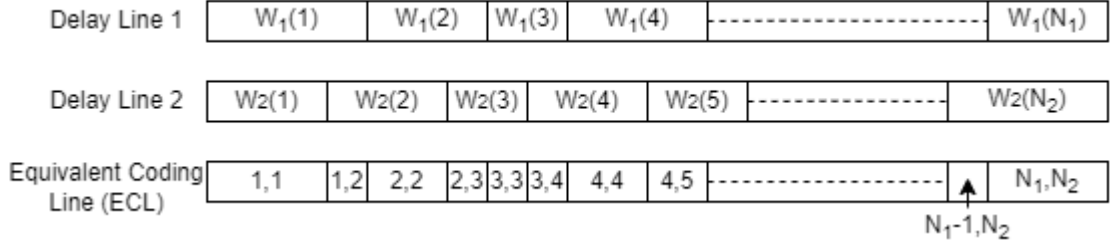
Figure 8: Diagram of Equivalent coding line delay line concept showing the boundaries of multiple delay lines being used to form a single delay line with smaller bin widths

The ECL aims to use these variations in the delay lines to form a single delay line. In Figure 8 an example of an ECL is shown formed of two delay lines. The boundaries of the two delay lines are used to make up the ECL where the bins are addressed relative to the bin codes of the two delay lines. In a delay line, knowing the bin widths, the time of a bin hit relative to the previous clock edge can be calculated by summing the current bin width W_M and the width of all the previous bins as seen in:

$$T_M(B_M) = \sum_{k=1}^{i} W_M(k) \tag{2.9}$$

Given the two bin addresses B_1 and B_2, the time recorded by the ECL can be calculated by:

$$W_E(B_1, B_2) = p \cdot T_1(B_1) + (1-p) \cdot T_2(B_2) \tag{2.10}$$

Where p is equal to 1 if the time measured by the first delay line is less than or equal to that of the second, otherwise it is equal to 0.

$$p = 1 \ if \ \sum_{k=1}^{B_1} W_1(k) \leq \sum_{l=1}^{B_2} W_2(l) \tag{2.11}$$
$$else \ p = 0$$

The total number of bins in the ECL is determined by $N_E = N_1 + N_2 - 1$.

M. Sadik, PhD, Thesis, Aston University, 2023

2.2 Time correlated single photon counting

2.2.1 Introduction

Time correlated single photon counting (TCSPC) is a measurement technique used to record optical waveforms with high accuracy by using repetitive measurements [14]. It is used in applications of photon counting light detection and ranging (LiDAR) [52], diffuse optical tomography (DOT) [53, 54] and fluorescent lifetime imaging microscopy (FLIM) [55, 56]. TCSPC uses time measurements between a single photon detector periodically illuminated by a laser and the laser reference signal to build a histogram of photon distribution which represents the optical waveform being measured. This section details various TCSPC schemes used for measurements.

2.2.2 Single start single stop

The classic approach to TCSPC known as the single-start single-stop or forward mode [5] is where the time difference is measured between two signals START and STOP as shown in Figure 9. Traditionally, the STOP channel is the single photon detector with the START channel being the reference signal from the laser driver. For any START tag i, the time difference to the subsequent STOP tag is utilised as in:

$$\Delta T(i) = T_{STOP} - T_{START}(i) \tag{2.12}$$

The time differences are then histogrammed with the process being repeated millions of times until a histogram that sufficiently represents the system IRF is obtained. Note that in forward mode TCSPC, typically only one STOP can be measured per measurement cycle.
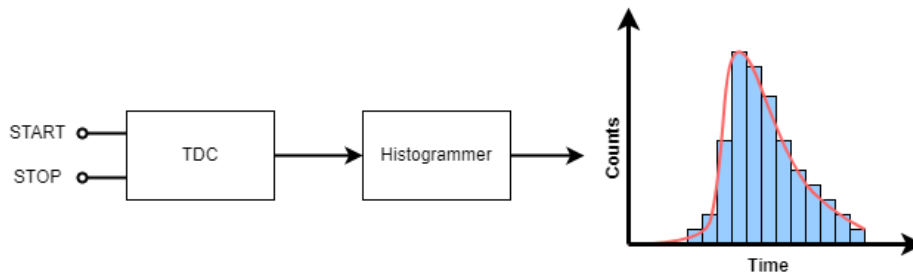
Figure 9: TCSPC measurement setup

One drawback of this method is the limitation to the acquisition rate, caused by the pile-up effect [57-59]. This problem comes from the fact that the single photon detectors typically used experience a dead time, where upon successfully detecting a photon, the detector will be unable to detect subsequent photons until the dead time ends, with typical detectors such as the iD100 experiencing a dead time of around 20ns [60]. If the light intensity (or mean number of photons per excitation cycle) is too high, it is possible for there to be more unrecorded photons within the signal period which would be lost causing a distortion in the measured optical waveform. Therefore, to mitigate pile-up and ensure the entire optical waveform is randomly sampled, the photon detection rate is reduced to be a percentage of the excitation pulse rate, normally around 10% [57, 61]. This lowers the photon detection probability, meaning for every ten START pulses there may only be 1 STOP pulse or successfully detected photon.

The deadtime of the TCSPC system in forward mode depends on the excitation rate of the laser. If a START pulse arrives before the TDC of the START channel has reset, then that entire START period may be skipped with any photons arriving within this period not being counted. To avoid this issue, many systems opt to run in reverse mode [62], where the START and STOP inputs are swapped. With this configuration the time differences are measured between the detector STOP pulses to the subsequent laser START pulse. This allows for the system to be run at higher rates due to the TDC not needing to reset for every START event, hence, lowering the impact of the dead time on the system.

19
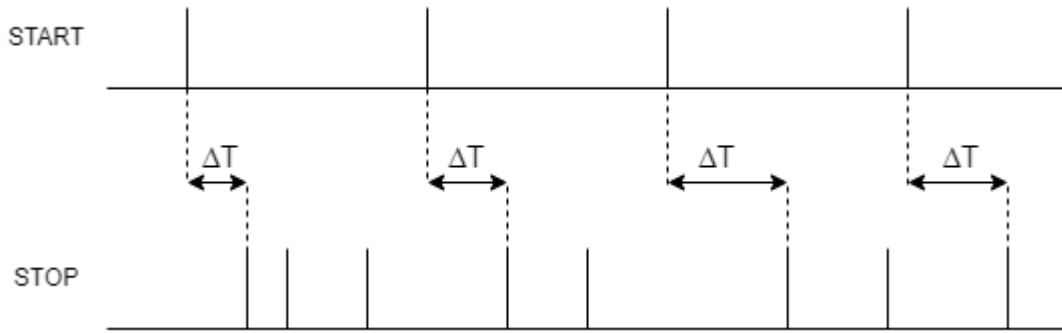
Figure 10: Forward mode Single start single stop TCSPC – note the number of stop pulses is exaggerated here for showing delta measurements.

2.2.3 Single start multi stop

The classic single-start single-stop system can be further expanded upon to include multiple stop measurements, forming a single-start multi-stop TCSPC system. In this approach multiple stop events following a single start event are recorded and the time between each of the events and the start event are measured and added to the histogram [63]. For any START tag i, the time difference to the subsequent STOP tags is calculated by:

$$\Delta T(i,j) = T_{STOP}(j) - T_{START}(i) \qquad (2.13)$$

Where j is an integer representing the STOP tag being used. The multi-stop approach has higher efficiency over the single START approach in applications where a low repetition rate is used as more information can be added to the histogram per START event.

2.2.4 Impact of the pulsed light source

The measured response of a single photon detector (SPD) is usually a convolution of the light source and the response of the SPD [59, 64]. Therefore, to accurately measure the response of an SPD, the laser used should emit pulses of width shorter than the IRF of the SPD so as not to distort (or in most cases, widen) the measurement. In other terms, if the optical pulse of the laser is longer than the IRF of the detector then the resultant measurement will be a measurement of the optical pulse's shape, rather than the IRF or jitter of the detector.

2.4 Single photon detectors

2.4.1 Introduction

Single photon detectors are devices which are sensitive to single photons and generate a pulse for a detected photon. They typically possess good time resolution making them useful for a variety of applications [65, 66]. Single photon detectors typically have a particular set of metrics as follows:

- Dark count rate: The number of detector output pulses when no incident light is present, this is caused by thermally generated noise.

- Dead-time: The time it takes until another photon can be detected after a successful detection.

- Photon Detection Efficiency (PDE): The efficiency of the detector defined as the ratio of the detector count rate to the number of incident photons.

- Instrument Response Function (IRF): Each detector will exhibit a certain amount of time noise or jitter from when an incident photon arrives at the detector to when the output pulse is generated. The width of the distribution of incident photon to output pulse generation (commonly referred to as IRF for detectors) is commonly given as the standard deviation of the distribution σ or the full width half maximum (FWHM). Hence, smaller distributions indicate a detector is introducing less jitter into the system.

- After pulsing probability: The probability that a detected incident photon will cause a secondary delayed event.

- Optical cross talk probability (for silicon photomultipliers and similar detector arrays): When an incident photon causes a detection in a microcell, light is produced during the breakdown [67]. For an array-based detector such as a SIPM, the light created during detection can cause another microcell in the array to produce a time correlated false output pulse [45, 68].

- Vbias / operating point above breakdown: The breakdown voltage is the voltage at which an incident photon can cause an avalanche in a diode-based detector. These detectors are normally operated above their breakdown voltage where higher values of voltage above breakdown can provide an increase in detection efficiency at the cost of higher noise values.

2.4.2 Photomultiplier tubes

Photomultiplier tubes (PMTs) are a form of vacuum tube technology which are used as single photon detectors due to their sensitivity to single photons [69, 70]. They are used in a variety of applications such as nuclear physics experiments, photon counting, and electromagnetic spectroscopy to name a few. Along with being sensitive to single photons, the PMT also has photon number resolving capabilities and as such can be used to determine the intensity of the light entering it in any particular instant. Photons enter the PMT through an input window which is directed at the cathode. The photons on the cathode's surface have a probability of exciting electrons into the vacuum, with these excited electrons being called photoelectrons. These photoelectrons in the vacuum are focused with an electrode onto a plate which acts as an electron multiplier known as a dynode. The PMT typically has several of these dynodes in series which is how it achieves high gain amplification. The electrons from the last dynode are collected on the anode of the device and at this point a current spike can be measured across the PMT, which is proportional to the number of incident photons.

2.4.3 Single photon avalanche diodes

Single photon avalanche diodes (SPADs) are a type of solid-state photodetector that are sensitive enough to detect a single photon. They have the advantage of a lower operating voltage and higher photon detection efficiency (PDE) in comparison to PMTs [71] which is why they are favoured over PMTs in applications such as photon counting [41, 72] and fluorescent lifetime imaging microscopy (FLIM) [55, 56]. The SPAD is operated with a reverse bias above its breakdown voltage, this is known as Geiger-mode operation. In Geiger-mode a single photon can cause an avalanche effect in the SPAD which results in a current spike that can be measured [73]. They are typically used along with quenching electronics to shorten the reset time of the photodiode once a photon has been detected [74-77]. An equivalent electrical circuit for the SPAD is shown in Figure 11 where switch S closes during the process of a photon induced breakdown.
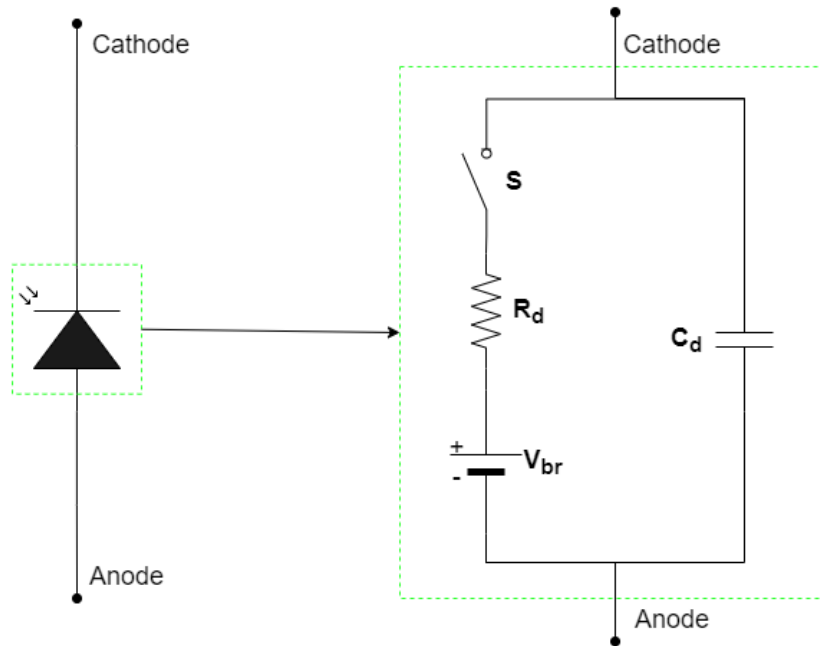
Figure 11: SPAD equivalent circuit, R_d is diffusion resistance, C_d is diffusion capacitance, and V_{br} is breakdown voltage

The quenching circuits come in one of two forms: passive quenching and active quenching [75, 77]. In a passive quenching circuit, a pair of resistors are used along with the SPAD where one resistor is used as a load (R_L) to limit the current while the other is used as an impedance coupler/sensing resistor (R_S). The passive quenching circuit has different configuration modes depending on where the resistors are placed, these can be seen in Figure 12. Note that the current-mode output is typically preferred, due to the sharp rising edge which reduces detector timing jitter.

M. Sadik, PhD, Thesis, Aston University, 2023
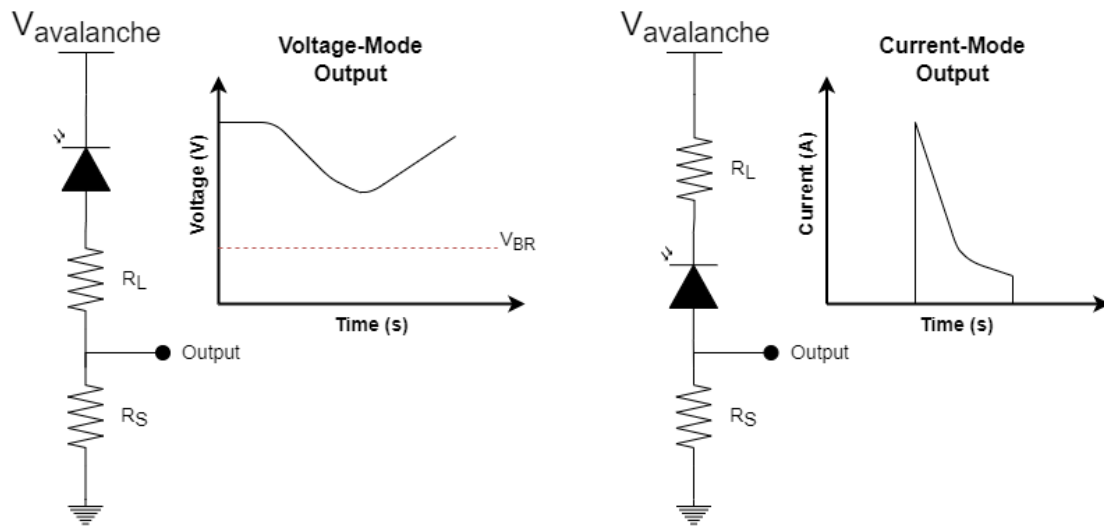
Figure 12: Passive quenching configurations showing (left) voltage mode circuit and output. (right) current mode and output shape

In an active quenching circuit, upon a successful detection the voltage across the SPAD is reduced to under the breakdown voltage to stop the avalanche process. A supplementary reset circuit is then used to increase the voltage up to the bias voltage. As active quenching is not explored in this work, the concept will not be discussed further.

2.4.4 Silicon photomultipliers

Silicon photomultipliers (SiPMs) are a type of solid-state photodetector based on the SPAD [68, 78]. They are composed of an array of SPADs, which are referred to as microcells, whose anodes and cathodes are all connected to each other, with each individual microcell having a passive quenching resistor as depicted in Figure 13. The construction and structure of SiPMs also allows them to have a lower operating voltage as compared to typical SPADs [60, 79, 80], with breakdowns in the region of 35V not being uncommon. They are insensitive to magnetic fields along with having the time resolution of a SPAD which makes them popular in medical applications like positron emission therapy (PET) [81, 82].

M. Sadik, PhD, Thesis, Aston University, 2023
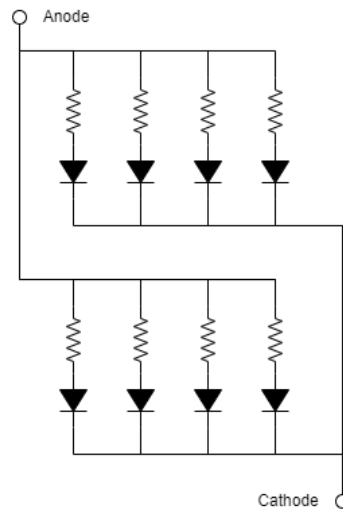
Figure 13: Example structure of SiPM

While possessing favourable features, many versions of the SiPM come with the downside of high correlated noise in the form of optical crosstalk and afterpulsing [45]. Crosstalk happens when an avalanching microcell causes an avalanche in another microcell due to the microcell emitting light during breakdown which is detected by other microcells, while afterpulsing happens when a photon causes an avalanche from a microcell followed by a secondary delayed avalanche in the same microcell. One quality of SiPMs that differentiates them from normal SPADs is the fact that they can resolve the number of incident photons. When they are reverse biased above breakdown and a single photon is detected by a microcell, a current spike is generated as it does in an SPAD, however, when two or more microcells are triggered, the current spike generated becomes proportional to the number of photons detected. Essentially the SiPM can be considered as an array of passively quenched SPADs with the outputs passively summed together. Hence, they can be run at higher pulse rates [83] while offering photon number resolving capability at the expense of an increased dark count which will scale with the detector size/number of microcells. However, as a SiPM is essentially a summed array of passively quenched SPADs, the dark count rate will scale with the number of microcells, which is the major downside with respect to conventional SPADs.

State of the art SiPMs can exhibit relatively low noise factors with dark counts as low as 30khz and crosstalk and afterpulsing probabilities of less than 1% being reported for a 1mm x 1mm SiPM with 2880 microcells from manufacturer onsemi [80]. These SiPMs exhibit good timing performance with a signal pulse width of 0.6ns and rise time of 0.3ns at the cost of a low PDE at

M. Sadik, PhD, Thesis, Aston University, 2023

only 14%. However, at larger sizes for the SiPMs (3mm x 3mm) the manufacturer reports PDEs up to 35% at an overvoltage of 2.5V. The downside of the larger SiPMs is the higher noise factors with a dark count rate of 300kHz and higher crosstalk probability of 10%. The timing performance is also affected with the 3mm x 3mm SiPM exhibiting a signal pulse width of 1.5ns with a rise time of 0.6ns on its fast mode output.

A proprietary fast mode output is present in addition to the standard output on SiPMs by manufacturer onsemi (formerly SensL). This fast mode is coupled to the individual diode through low capacitance and offers a faster rise time along with a shorter pulse width over the standard output mode [84, 85]. An example of the fast output terminal is shown in Figure 14.
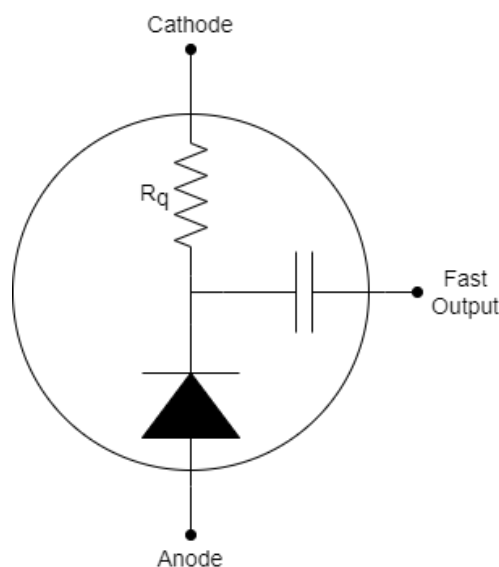
Figure 14: Silicon photomultiplier microcell with built in quenching resistor and a capacitively coupled fast output terminal

In [86] the author characterises a SiPM for multiple simultaneous detections showing that the amplitude of the electrical output pulse of the SiPM to be proportional to the number of detected photons. The time correlator presented in [87] is the only literature example of using photon number information in an acquisition and measurement system. However, all the systems to date post-process digital oscilloscope data (time series of detector voltage) and therefore no measurements are completed in real-time. This unique feature of SiPMs has not been fully utilised in the literature and therefore remains an area of interest and is the main focus of this work.

M. Sadik, PhD, Thesis, Aston University, 2023

2.5 Light detection and ranging

2.5.1 Introduction

LiDAR is a method for measuring distance to a target using a pulsed laser and a photon detector based on the principle of time-of-flight (ToF) [88, 89]. By measuring the time taken for a round-trip of the optical pulse, the distance to the target can be calculated by multiplying half the round-trip time by the speed of light (299,792,458 m/s). There are two types of ToF LiDAR systems [89]: scanning LiDAR and flash LiDAR. In scanning techniques, the system uses a single photon detector, typically a SPAD, and a mechanical rotating platform to take measurements in quick succession providing up to 360 degrees of view. A collimated laser beam is used to scan the illuminated field of view one point at a time.

Flash LiDAR [90] does not make use of any moving parts and instead uses a laser with a wide diverging beam and an array of sensors to measure a scene in one laser excitation cycle. Removing the rotary mechanics reduces the maximum field of view of the system but allows for more rapid acquisition of data at the expense of a reduced signal to noise ratio [91]. Flash LiDAR systems typically make use digitally controlled mirrors using micro-electro-mechanical system (MEMS) technology [91, 92] with these MEMS mirrors helping to steer the light allowing a wider angle to be measured by the flash LiDAR system. However, the amount of steering they provide is low, typically only around 20-30 degrees [93, 94].

2.5.2 Biaxial and coaxial light detection and ranging

A LiDAR system for ranging in free space can be categorised into one of two optical configurations: biaxial and coaxial [95, 96]. They differ in their optical setup where in coaxial LiDAR the same optical delivery path is used for both the laser and the detector, whereas in biaxial LiDAR the receiving optics are placed adjacent to the emitting optics as depicted in Figure 15 a) and b) respectively. A coaxial LiDAR setup can be cost effective and save on space and weight by removing the need for a secondary optical setup for the receiver. However, the amount of backscatter picked up by the detector is increased causing optical crosstalk which can possibly saturate the detector. The effect of backscatter in a coaxial system can be partially mitigated by

gating the photodetector, where the photodetector is made to only be photosensitive during a small window of time, although this adds further complexity into the system.
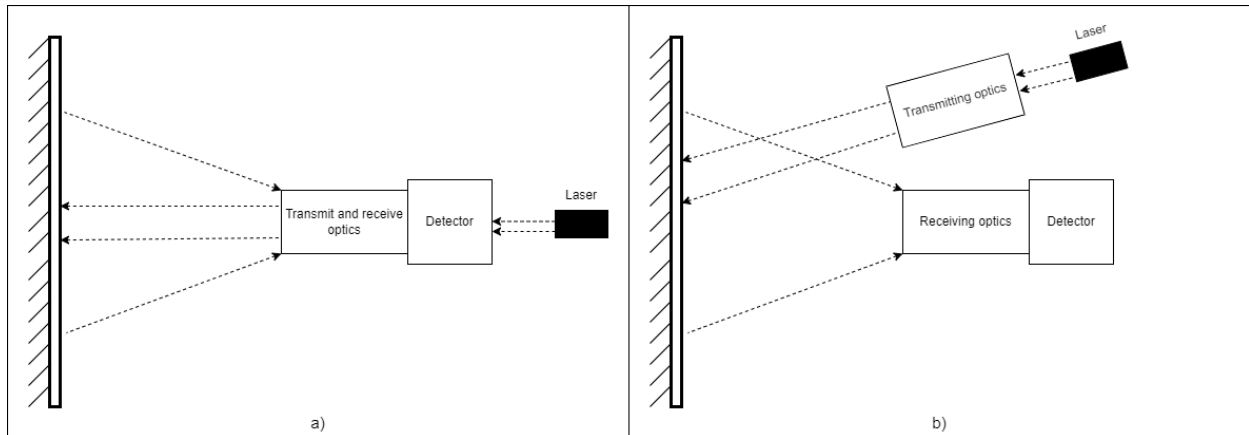
Figure 15: a) Coaxial LiDAR setup. b) Biaxial LiDAR setup

In a biaxial setup the issue of optical crosstalk is eliminated due to the use of a separate optical path for the detector. However, separating the optics for the emitter and receiver leads to less optical efficiency due to lower measured light levels while the measurement itself can only be performed starting from a certain range where the optical path of the emitter and receiver overlap.

2.5.3 Phase shift LiDAR

Phase shift LiDAR is a common technique that differs from ToF LiDAR in how it is operated. In this technique the laser pulse is sinusoidally modulated, and the phase of the returning signal is measured [97-99]. The phase of the laser pulse is measured at the start of a measurement and the difference with the return signal phase is measured and calculated. Knowing the measured phase difference $\emptyset$, and the modulation frequency f_m, then the round trip time of flight t, is calculated as:

$$t = \frac{\emptyset}{2\pi f_m} \tag{2.14}$$

The distance to the target is then calculated as the product of the time of flight and the speed of light. However, such a system suffers from range ambiguity [100], where if the phase difference exceeds 360°, the apparent round-trip time will wrap back around 0 causing ambiguity to resultant time/distance measurements.

2.5.4 Single photon counting light detection and ranging

Photon counting LiDAR uses TCSPC to measure the round trip delay of a laser pulse emitted from the system, reflected off the object, and collected by the receiving optics. Due to multiple measurements being needed to acquire a statistically valid histogram this method is considered slower than other methods of LiDAR in ranging where a single measurement is often enough to resolve the time [89]. However, due to the high sensitivity and excellent time resolution of TCSPC it is popular in applications where low light level returns are expected. The author in [101] demonstrates a photon counting LiDAR solution that operates at ranges up to a few kilometres by using laser sources of varying wavelengths. To increase the range of photon counting LiDAR systems, the authors of [102] and [103] propose high-speed systems that use laser pulses of multiple repetition rates to extend the unambiguous measurement distance and achieve faster detection rates. Unambiguity here refers to exceeding the amount of time the TDC can measure which causes the time to wrap around to 0. Furthermore, Yu [104] proposes a macro-pulse photon counting ranging method to allow for fast detection of moving targets. This was based on the work done by Takeuchi in [105] where a pseudo random coded lidar system was demonstrated that achieves fast detection and improved signal to noise ratio.

2.6 Conclusion

In conclusion, this chapter starts with an overview into various methods for implementing TDCs on FPGAs as well as improvement techniques used to improve the linearity and resolution of FPGA based TDCs. The calibration of such TDCs is discussed with methodology on how they are performed. As this work focuses on SiPMs, a background on them and other single photon detector technologies is provided outlining their differences. The principle of TCSPC is discussed along with 2 separate methods of implementation, the single start single stop and single start multi stop methods. Finally, LiDAR is discussed along with some methods of implementation as well as the different optical setups used in free space ranging.

3.0 Silicon photomultipliers as single photon number resolving detectors

3.1 Introduction

This chapter evaluates a typical SiPM's suitability for time correlated photon counting applications. SiPMs consist of an array of SPADs with their outputs passively summed. Note that TCPC is mentioned here (rather than TCSPC) due to the system no longer necessitating a mean photon number of <=0.1. This chapter will first introduce a model developed to evaluate the possible performance advantage of the SiPM in comparison to conventional SPADs. Subsequently, the detector and experimental setup are discussed, followed by measurements of a SiPM's performance and characteristics.

3.2 Modelling and analysis

3.2.1 N-photon detection probability

Following the work performed by the author in [86] , the theoretical probability of the detection of n avalanches was modelled. This is shown in Figure 16, where the Poissonian statistics for multi photon detection for the SiPM can be observed in addition to the model developed in [86] for varying mean photon numbers. This is model includes the value of optical crosstalk that would be present in a real typical SiPM. The probability $p(n)$ of having n avalanches (including those caused by crosstalk) is defined by the author as being:

$$p(n) = \frac{p_{th}(n) + (n-1)p(n-1)p_{ct}}{1 + np_{ct}}, \quad n > 0 \tag{3.1}$$

Where $p_{th}(n)$ is the theoretical probability of n avalanches occurring and p_{ct} represents the crosstalk probability of the entire detector where a breakdown event in one microcell could also trigger a breakdown in an adjacent microcell. As equation 3.1 is a simple model which only accounts for an avalanche in the SiPM triggering only a single additional breakdown, it cannot represent a real SiPM where an avalanche event may trigger more than one additional breakdown with those additional crosstalk breakdowns also having the probability of causing additional breakdowns. With higher values of p_{ct} the probability of crosstalk breakdowns in the model

increases, however, if the value of $p_{ct} > 1$ then every time a microcell of the SiPM breaks down it induces a crosstalk breakdown and due to the nature of equation 3.1 being recursive this means that every time an avalanche occurs in a single microcell of the SiPM all the other microcells in the SiPM would have breakdowns. The application of equation 3.1 can be seen in Figure 16 where it is represented by the solid lines with the dashed lines being generated from a conventional Poissonian probability mass function. This model does not account for crosstalk induced breakdowns triggering more than one additional crosstalk induced breakdown and the value of p_{ct} is set to 9.7%, the same as in [86].
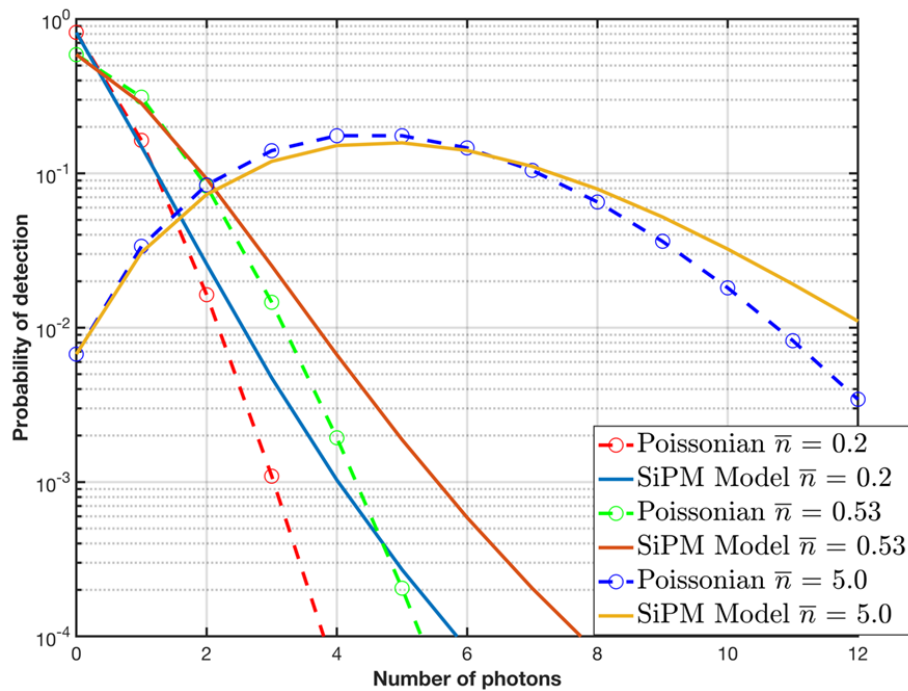
Figure 16: Modelling of SiPM photon detection statistics using Poissonian statistics and the model developed in [86] for varying mean photon numbers with the crosstalk probability (P_{ct}) being 9.7%

3.2.2 Decoded N-photon event model

The modelling of the poissonian statistics were taken a step further with the decoded number of photons per pulse being plotted for both a SiPM and a SPAD, using the model in [86]. In this modified SiPM model, it is assumed that the SiPM and its associated instrumentation can resolve up to 4 photons with optical crosstalk also being included. This is shown in Figure 17 where the SiPMs can be seen to detect up to 4 photons per pulse at a mean photon number of 4 and higher. It is a similar case for the SPAD as it also reaches its maximum photon detection output at a mean photon number of ~4. The SiPM model may appear more likely to detect photons, but this

M. Sadik, PhD, Thesis, Aston University, 2023

is due to optical crosstalk being modelled. However, this modelling comparison to a SPAD proves that fundamentally there is an advantage in using the photon number resolving ability of the SiPM.
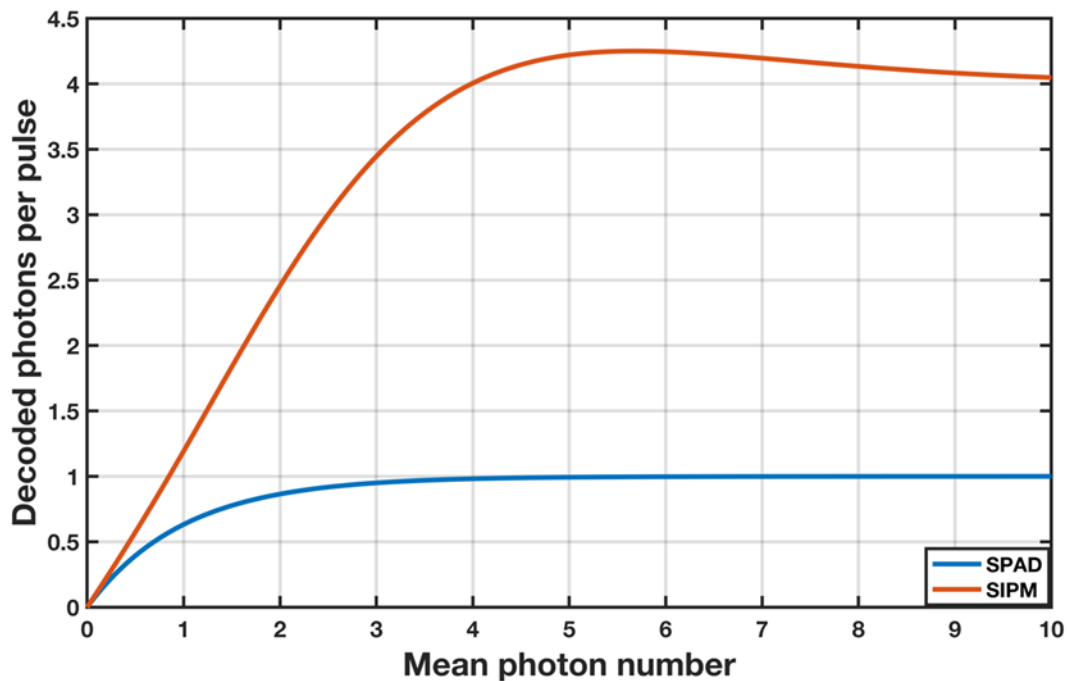
Figure 17: Simulation of decoded photons per pulse for SiPM and SPAD based off poissonian statistics. The simulation shows the SPAD starting to saturate at around a mean photon number of 1 and being fully saturated around a mean photon number of 4. The SiPM stays linear for longer than the SPAD until it approaches a mean photon number of 3 at which point it starts to saturate. Note the gradient of the SiPM is greater than the gradient of the SPAD before the SPAD starts to saturate due to the added optical crosstalk probability of 9.7%

3.3 Experimental characterisation

3.3.1 Introduction

This section outlines the various experiments performed on an onsemi MICRORB-SMA-10035 SiPM [79], a detector 1mm x 1mm in size consisting of 620 microcells, to characterise its performance as a single photon number resolving detector. Unlike a SPAD pulse where the output amplitude is always constant, the amplitude of a SiPM pulse scales depending on the number of photons detected within that pulse. This occurs due to multiple microcells triggering at the same time, each one adding to the output an amplitude equivalent to a single photon event [68].

A Tektronix MDO4104C digital oscilloscope [106] capable of sampling at 5GS/s with a 1GHz bandwidth was used to record the SiPM pulses into a comma separated values (CSV) file which was then analysed using MATLAB scripts on the PC side. The following sections detail the testing platform developed for the SiPM module as well as the results from the various experiments performed.

3.3.2 Experimental setup

As the onsemi MICRORB-SMA-10035 SiPM comes as a barebones module, to begin characterising the detector an enclosure was used to seal off ambient light and only let in light focused on the SiPM die. For the housing, a hermetically sealed aluminium enclosure was fitted with a Thorlabs Fiber Port [107] such that the SiPM was placed roughly in the optical path of the fiber port's collimated output. A 3D printed part was designed, printed, and used to secure the SiPM module to the enclosure. To then align the optical path as well as possible, a continuous wave light source was coupled into a multimode fibre to the input of the fibre port such that the light was clearly visible on the output using the naked eye. The optical path of the fibre port was then adjusted using the two XY axis screws on the side while measuring the count rate of the detector in real time until it was tuned to the highest achievable count rate.
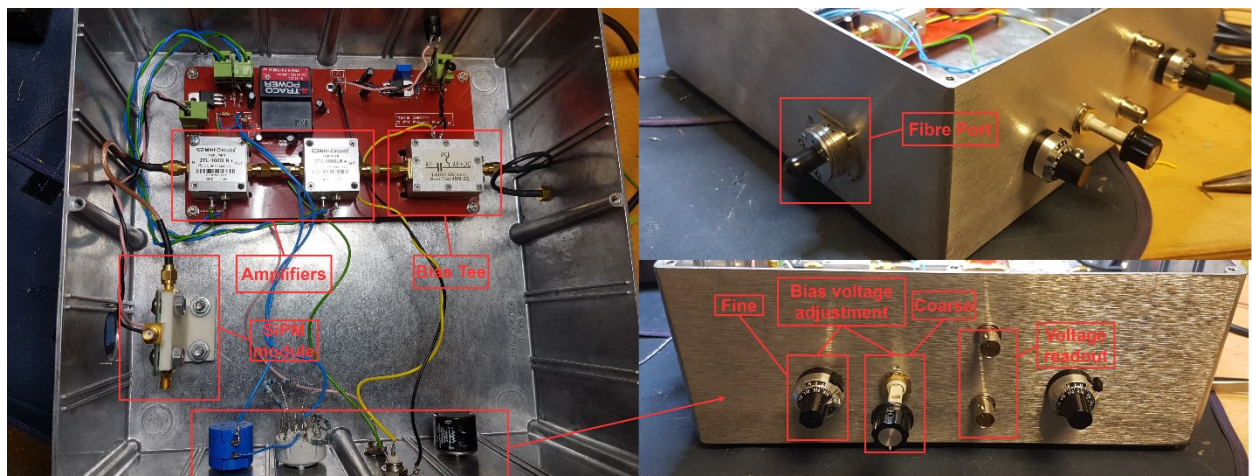
Figure 18: Picture of SiPM box showing internals, fiber port and front panel controls

Aside from being used as a light proof box for the exposed module, the enclosure also housed the necessary electronics to operate the SiPM. This included 2 amplifiers, a bias tee, and 2 separate power supplies. One of the power supplies was used to provide the negative going bias voltage needed for the SiPM using an adjustable high voltage linear regulator [108]. The regulator

was adjusted using a multi-turn potentiometer for fine steps and a resistor network on a rotary switch was used for coarse adjustments, both of which were placed on the outside of the enclosure to allow for the bias voltage to be easily adjusted.
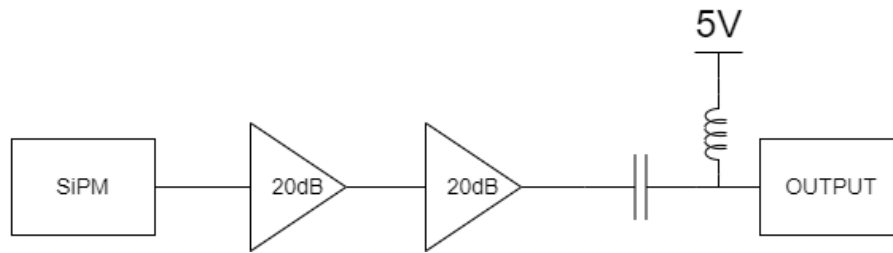
Figure 19: Diagram showing the signal path of the SiPM, the signal is amplified then offset with a bias tee

The second power supply provided 15V for the pair of Mini-Circuits ZFL-1000LN+ [109] low noise amplifiers, used to raise the low amplitude [79] of the SiPM pulses, which are typically a few mVs. In addition to this, it also powered a bias tee at 5V through a 7805 linear regulator to provide a DC offset for the detectors negative going pulses. An SMA connector placed on the side of the enclosure was used for the detector readout and was internally connected to the bias tee. A diagram showing the complete signal path of the SiPM is shown in Figure 19.

3.3.3 Silicon photomultiplier bias above breakdown vs dark count rate and optical crosstalk

When powering the SiPM, the overvoltage applied affects the noise parameters present within a SiPM such as the optical crosstalk and dark count rate. To determine these parameters for the SiPM module used in this work, the output of the SiPM was measured using an oscilloscope while the bias voltage above breakdown was adjusted. In the datasheet for the module [79], a typical overvoltage value of 7V and a max value of 10V above breakdown is recommended. The SiPM module used came with a measurement of the breakdown bias voltage at 26.4V, and so the overvoltage values between 33.4V-36.4V were tested with the SiPM.

One of the main contributors of noise in a SiPM is the dark count, where unlike SPADs that typically experience dark counts in the range of tens to hundreds of Hz, the dark count rates of SiPMs are typically in the MHz range, as the output is the sum of all the microcell outputs. The dark count rate was measured by collecting SiPM data in a lightproof environment for the various

M. Sadik, PhD, Thesis, Aston University, 2023

overvoltage values over a certain integration time. The dataset at each overvoltage value was analysed to determine the total number of counts within that dataset. This number was then divided by the integration time to obtain a value for the dark count rate at that overvoltage. Figure 20 shows the measured dark counts and from this we can see that the rate increases almost linearly with the increase of the overvoltage.
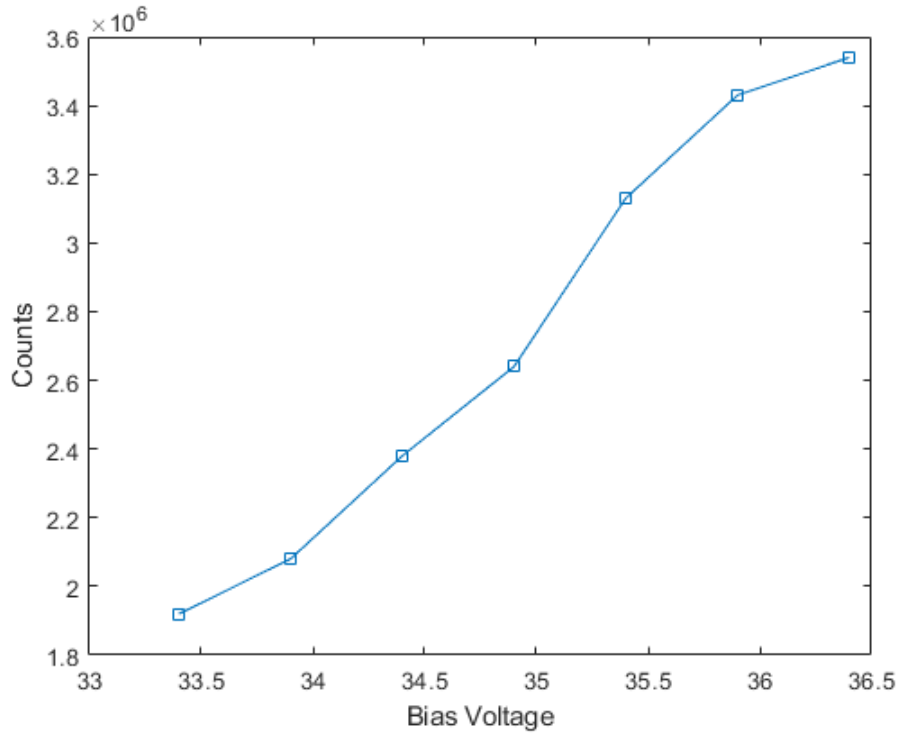
Figure 20: Dark count rate of the SiPM measured at various bias voltages

Another major source of noise in a SiPM is the optical crosstalk, which is defined as the probability of an avalanching microcell causing an avalanche on another microcell. This process happens almost instantaneously and as such a single incident photon may generate a signal equivalent to a 2-photon event or higher. Furthermore, an estimation of the crosstalk can be obtained by measuring the ratio of the count rate of multi photon events (signal amplitudes higher than single photon events) to the total count rate while the detector is kept in the dark [45] as of:

$$crosstalk\ (\%) = \frac{dark\ counts\ of\ N_{photon} \geq 2}{total\ dark\ count\ rate} \times 100\% \tag{3.2}$$

This means that the same datasets as the ones used for measuring the dark counts can be used to estimate the optical crosstalk. The equation is valid if the value of the total count rate in the

M. Sadik, PhD, Thesis, Aston University, 2023

SiPM is greater than 0. A time gate of 200ps is used to distinguish a peak found from a crosstalk peak as a crosstalk event happens almost instantaneously after a detection. Figure 21 shows the measured crosstalk across the range of bias voltages. At a bias voltage of 33.4V (7V overvoltage) the SiPM was estimated to exhibit a crosstalk probability of 43%, the same amount denoted in the datasheet.
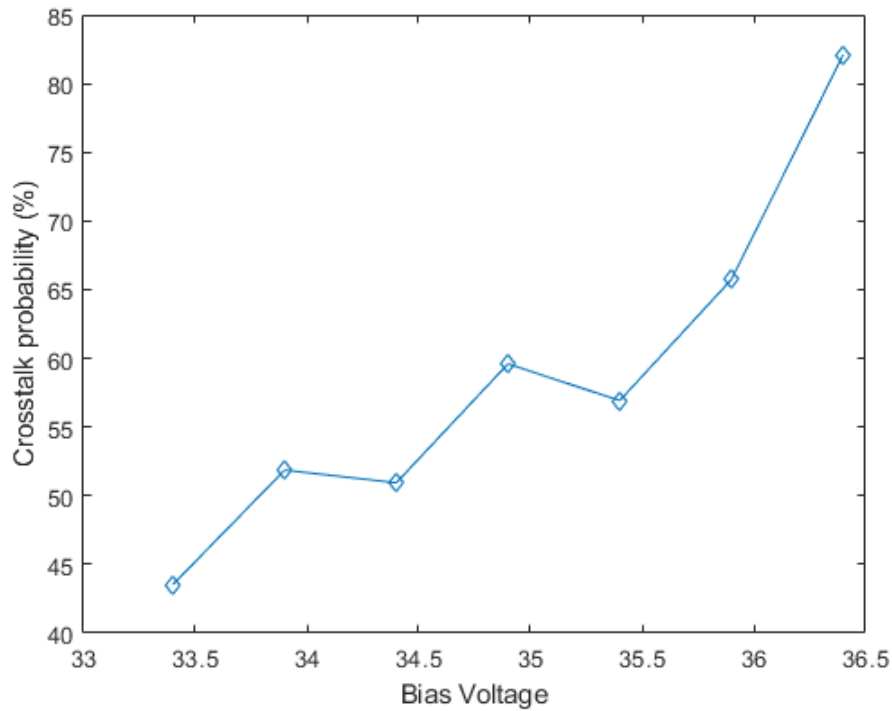
Figure 21: Crosstalk probability measured for various bias voltages

3.3.4 Silicon photomultiplier typical output pulses
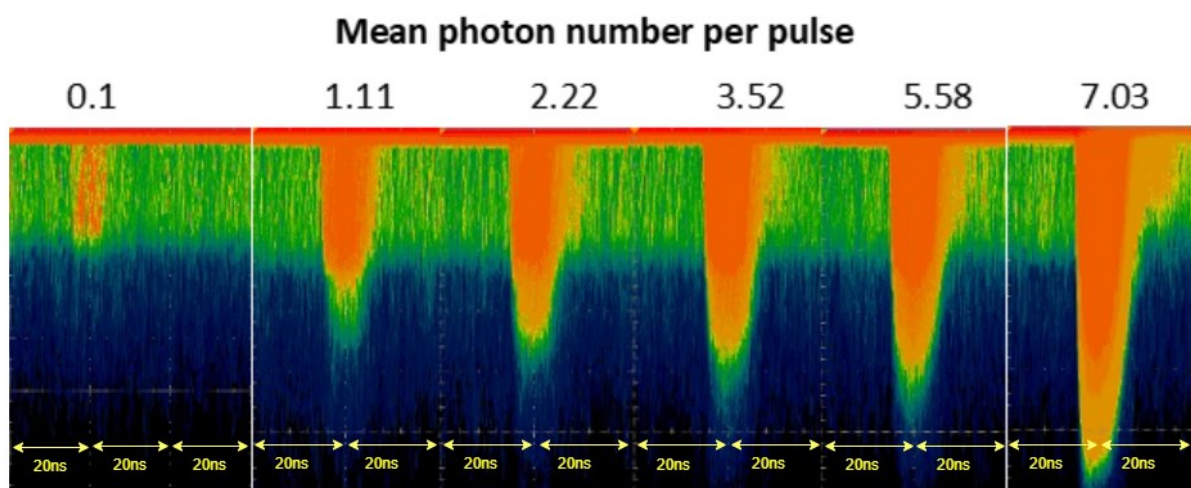
Figure 22: Heat map of SiPM output pulses measured using oscilloscope performed with a timescale of 20ns per division at varying light levels showing the effect of optical crosstalk on the right of the main pulses

When looking at the SiPM pulses on an oscilloscope at varying light levels we can observe the effect of the photon number resolving capability of the detector in Figure 22, as the negative going pulse height clearly scales with the mean number of incident photons. Furthermore, it is believed that the optical crosstalk can be observed in Figure 22 at higher mean photon levels, the crosstalk can be seen more clearly on the right of the main pulses. In addition, Figure 23 shows the SiPM input pulse amplitudes when they are histogrammed using the built-in oscilloscope functions, as shown in orange on the left of the diagram. Amplitudes are only histogrammed to generate amplitude for the centre of the peak (shown as a red line on the diagram) and the pedestal values (zero photon voltages) are omitted for maximum clarity. This gives an idea on the typical multi photon amplitudes and the maximum number of photon events the detector can discriminate.

In accordance to what was inferred in [110], the acquisition bandwidth of the oscilloscope was reduced from 1GHz to 250MHz for the SiPM channel to maximise fidelity of the amplitude spectrums and improve the peak to trough ratio. To demonstrate this, the same experiment was performed with the 250MHz bandwidth limit on the oscilloscope, with the resultant signal and amplitude spectrum being shown in Figure 24. Using the 250MHz acquisition bandwidth has a low pass filtering effect on the SiPM signal and ends up smoothing/averaging the pulse amplitudes over time, which in turn results in the various mean photon events to be more easily distinguished.
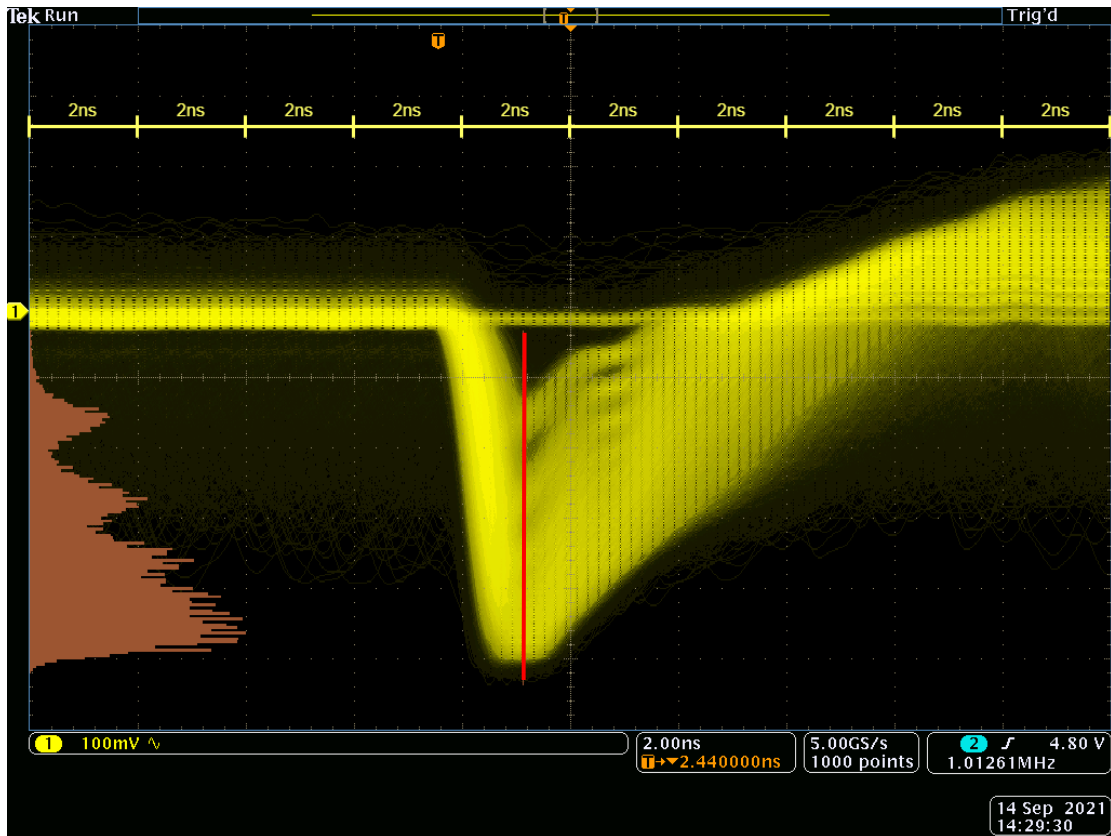
Figure 23: SiPM output pulses measured using built in oscilloscope histogram feature using a full 1GHz bandwidth. The amplitude spectrum histogram is shown in orange on the left. The red line shows the amplitude range which forms the histogram. The timescale used on the oscilloscope was 2ns per division
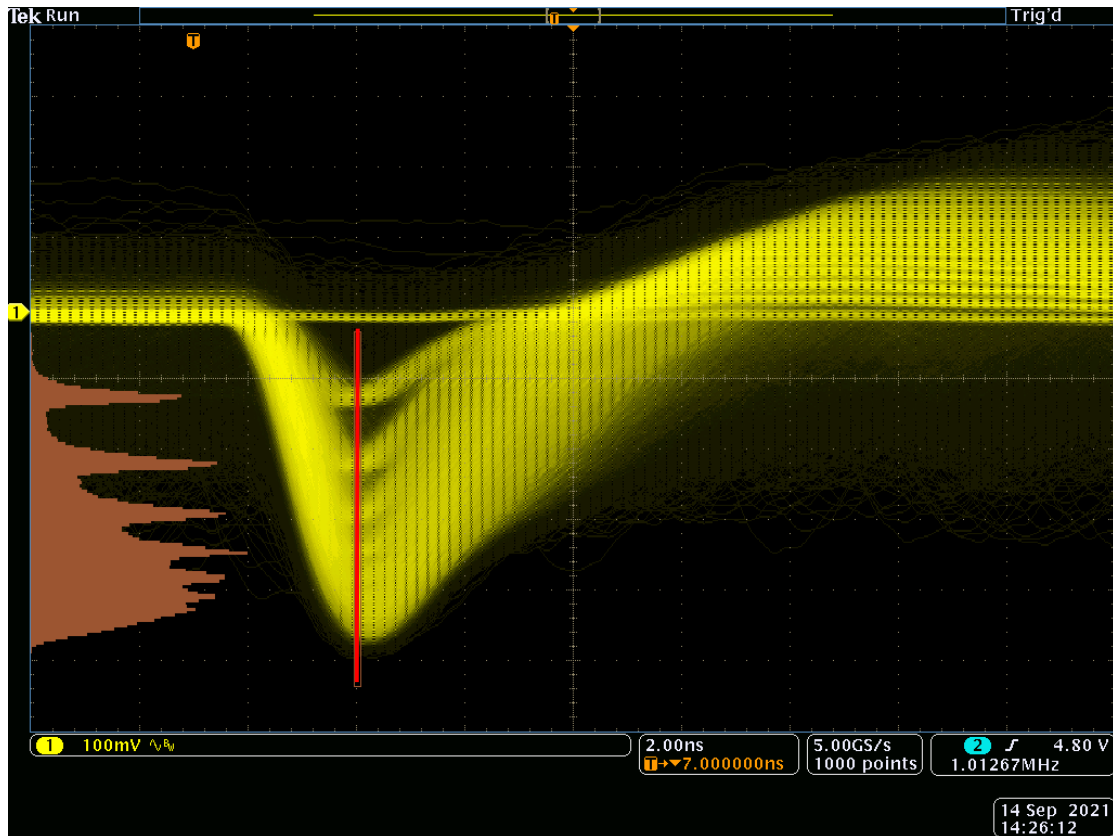
Figure 24: SiPM output pulses measured using built in oscilloscope histogram feature with a bandwidth limit of 250 MHz. The amplitude spectrum (orange) is considerably more distinct. The red line shows the amplitude range which forms the histogram.

The SiPM data was further analysed to determine the effect of applying low pass filters to the signal at varying frequencies and the peak to trough ratios for the first two photon peaks were observed. Figure 25 shows the recorded peak to trough ratios at the varying frequencies where an increased ratio was observed as the value of the filtering frequency decreased. Taking this into account along with the data in Figure 26, which shows the ratios between the first 2 photon peaks of the SiPM signal with the varying low pass filter frequencies applied, it is observed that while the ratio between the first photon peak to the second stays roughly constant (around 2.1:1) except at the lowest frequencies under 100 MHz. The peaks become more pronounced making it easier to distinguish between the various photon levels in the signal. For further measurements with the SiPM performed later in this chapter, a low pass filter was chosen with a 250 MHz cut off as it offered an improvement in the signal while still maintaining acceptable timing precision.

M. Sadik, PhD, Thesis, Aston University, 2023
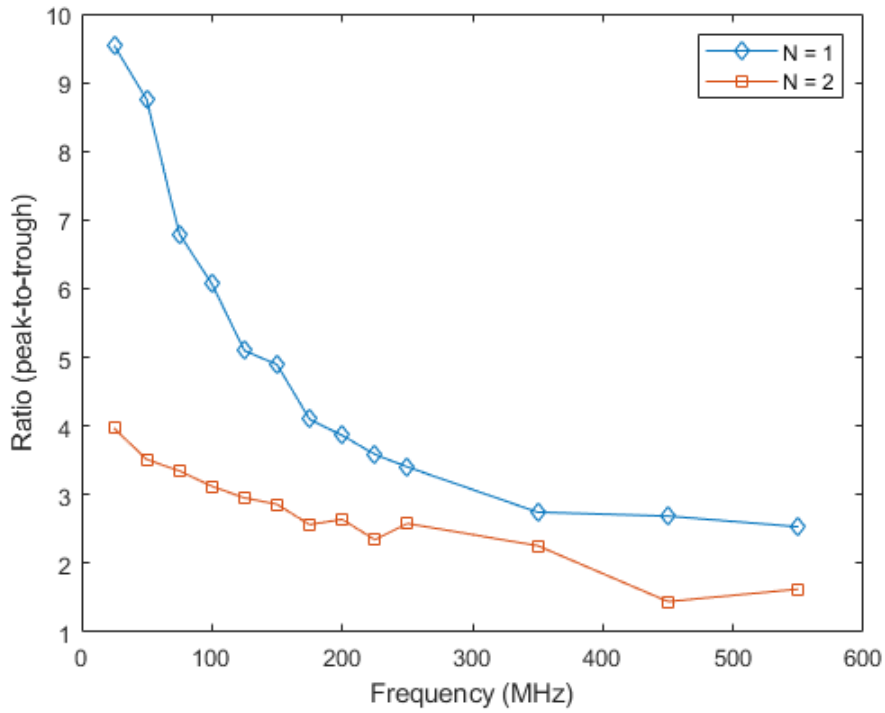
Figure 25: Peak to trough measurement of first and second peak in the SiPM signal for varying low pass filter cut-off frequencies
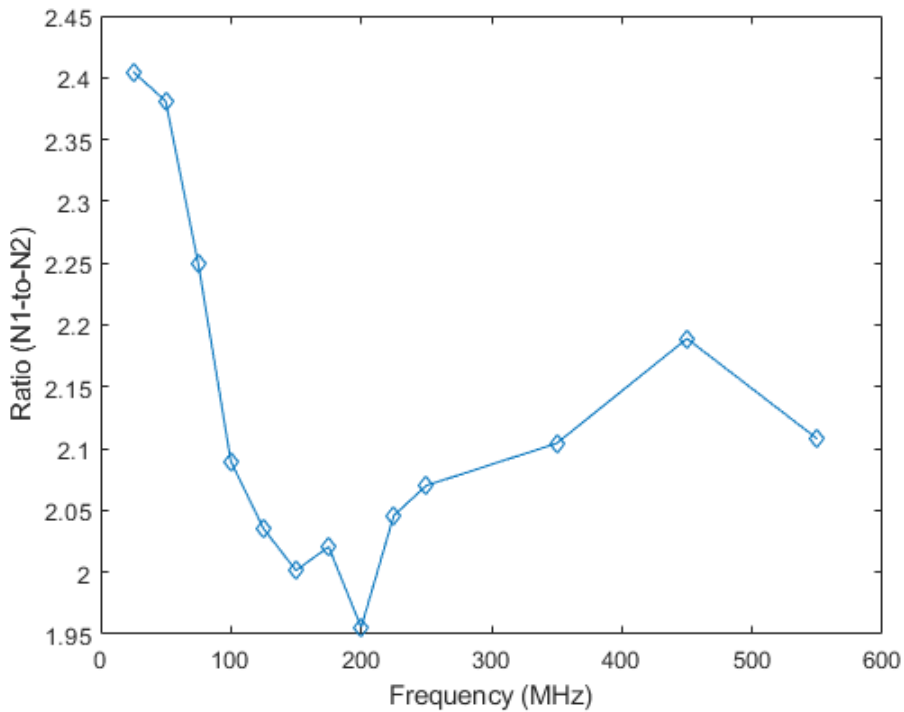
Figure 26: Ratio of the first peak to the second peak in the SiPM signal corresponding to N = 1 photons and N = 2 photons respectively for various cut-off frequencies

3.3.5 Silicon photomultiplier count rate vs mean photon number

To investigate whether the SiPM can provide a benefit over SPADs in TCSPC, several measurements were performed with the SiPM where the mean photon number per laser excitation pulse was adjusted. A Thorlabs multimode fiber pig-tailed laser diode [111] at a wavelength of 635nm was pulsed using an iC-Haus iC-HS05 laser diode driver [112] and was coupled to a multimode fibre.

The multimode fibre output from the laser diode was coupled into a Thorlabs Fiber Bench [113] such that $1/2$" neutral density (ND) filters [114] could be placed in line with the optical path to the detector to limit the amount of light passed through. Using an FCPC coupled Thorlabs PM100D optical power meter, the unattenuated optical power at the output of the Fiber Bench was initially measured. A diagram of the experimental setup is shown in Figure 27. To then limit the amount of light, the required amount of ND filtering had to be calculated.
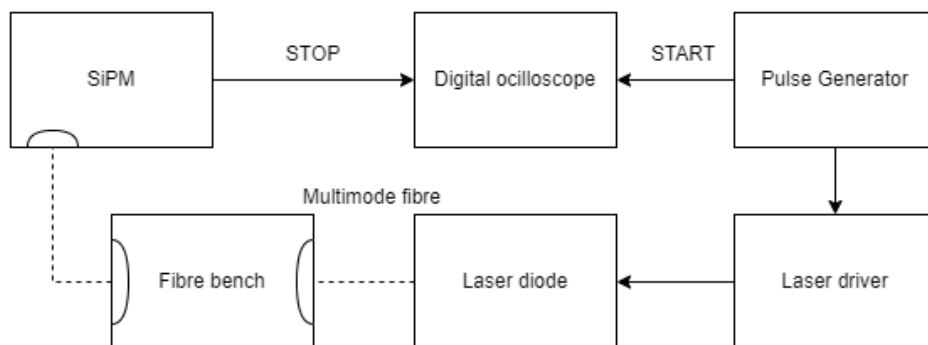
Figure 27: Diagram of experimental setup for SiPM measurements using a pulse light source. Dashed lines represent optical paths and solid lines represent electrical paths

For this, first the unattenuated number of photons per second $N_{photons/sec}$ were calculated. This was done by finding the energy per photon according to:

$$E = hf$$

M. Sadik, PhD, Thesis, Aston University, 2023

where h is planck's constant and f is the frequency of red light at 635nm. From this, the total number of photons per second were calculated by:

$$N_{photons/sec} = \frac{Unattenuated\ optical\ power\ (W)}{E\ (J)}$$ (3.3)

With this information known, the unattenuated number of photons per pulse N_{pp} was calculated using:

$$N_{pp} = \frac{N_{photons/sec}}{repetition\ rate\ of\ laser\ (Hz)}$$ (3.4)

Once this had been calculated, the next step to determining the required ND amount involved calculating the ratio between the desired N_{pp} value to be tested and the unattenuated N_{pp}. Finally using this ratio, the value of ND filtering required was calculated to the first decimal point using:

$$ND = -\log\left(\frac{T}{100\%}\right)$$ (3.5)

With T representing the percentage of the input to be transmitted.

The first set of TCSPC measurements done with the SiPM, at a bias voltage of 33.4V (7V overvoltage) was done at an optimal light level for SPADs with ND filters being used to keep the $N_{pp} = 0.1$ at the fiber to avoid pile-up. The laser driver was pulsed at a rate of 10 MHz using a square wave from a pulse generator.

All measurements shown in this section were taken from the oscilloscope and consisted of 20 million points sampled at 5 GS/s for an integration time of 4ms, taken for both the detector and the START reference. This was repeated multiple times at each of the data points to collect a larger amount of data for post processing. The result of the initial measurement for the SiPM is shown in Figure 28 where the correlation in the observed SiPM signal is indistinguishable from

M. Sadik, PhD, Thesis, Aston University, 2023

the noise in the detector at this low level of light, due to the considerably higher dark count of the SiPM. Note that for all correlations presented in this chapter, the amplitude information is not used in the formation of the histograms.
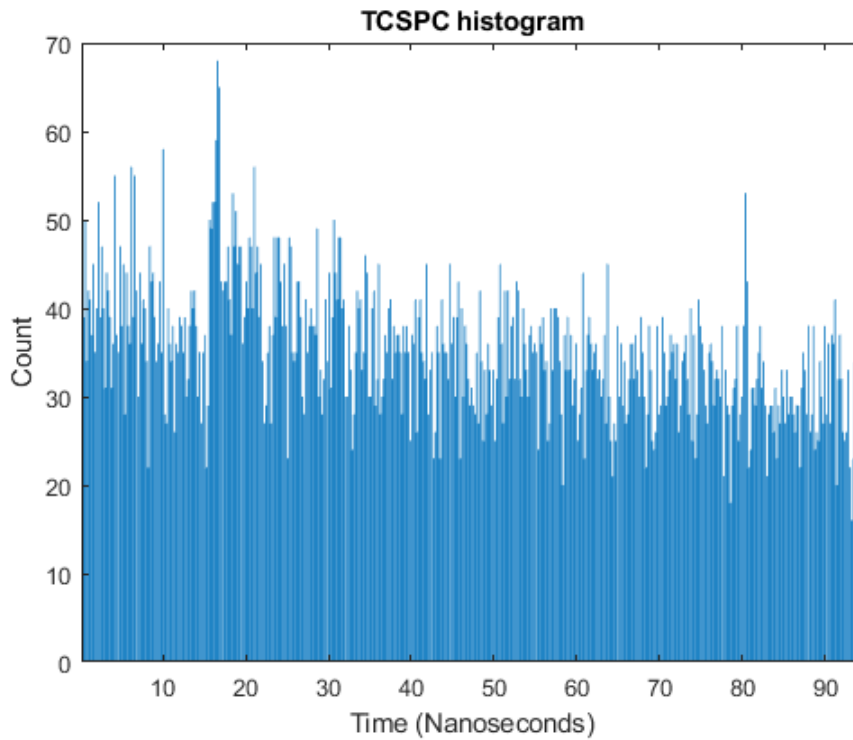
Figure 28: TCSPC measurement with SiPM at bias 33.4V at Npp = 0.1 for a duration of 4ms

Further tests were performed on the SiPM to evaluate its performance at various higher light levels by changing the ND filtering in the Fiber Bench to provide varying N_{pp} values at the fibre port. At first the count rate of the SiPM was observed for varying values of N_{pp} as shown in Figure 29 for a 4ms period. From this data it was observed that the count rate of the SiPM increases linearly until it nears $N_{pp} = 10$ at which point the detector starts saturating and starts to go non-linear. Because of this, light levels up to $N_{pp} = 10$ are deemed to be in the acceptable working range of the SiPM at this bias voltage. Note that the measurements of N_{pp} are done at the fibre and does not take into consideration the loss in the fibre port nor the imperfect coupling of the SiPM.

M. Sadik, PhD, Thesis, Aston University, 2023
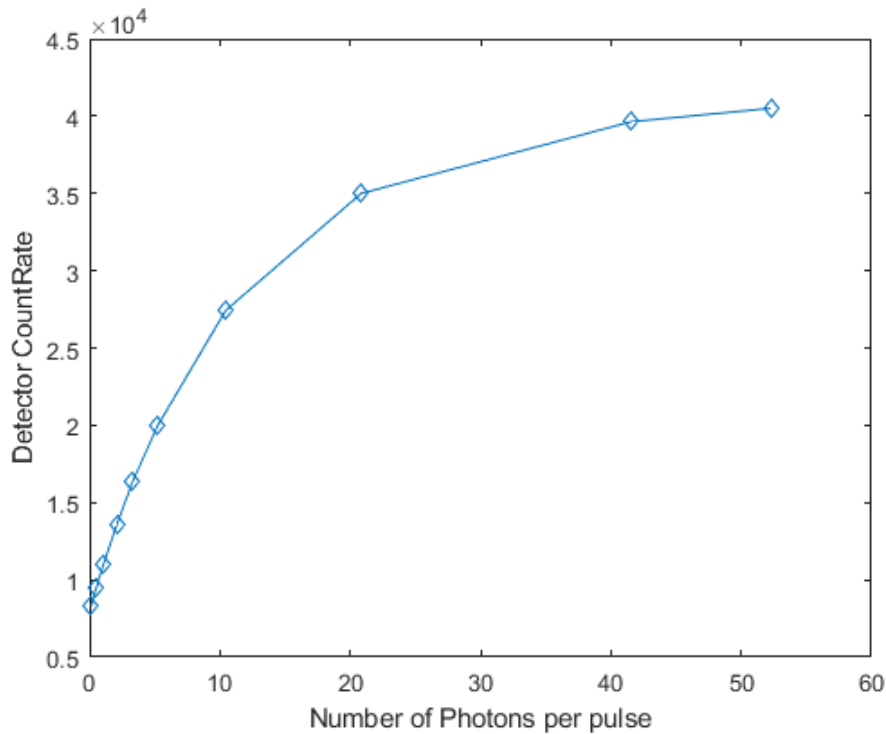
Figure 29: Measurement of SiPM Count rates (per 4ms period) for varying Npp values, Biased at 33.4V

Observing the SiPM at light levels slightly higher than the optimal level for SPADs at $N_{pp} = 0.5$ in Figure 31, the measured waveform can be seen unlike at $N_{pp} = 0.1$ although the noise floor is still dominantly visible within the correlation (low signal to noise ratio). As the light levels were slowly increased until it reached $N_{pp} = 10$, the number of correlated photons being detected also increased and the correlation became more distinguished from the sources of noise with this process being observable in Figure 31 to Figure 34.

The measured SiPM output can be seen to have multiple secondary peaks in the measured waveforms. These secondary peaks were measured to repeat approximately every ~2.4 ns and was present throughout all measurements taken with the SiPM. Figure 30 shows the secondary peaks in question with a measurement performed at 33.4V. The SiPM was measured using a separate electrical signal path with a new amplifier to rule out whether the secondary peaks were from a reflection in the electrical path while the SiPM was kept in its enclosure due to the ambient light. No change was observed in the SiPM output when changing the experiment setup. While the exact cause of these reflections has not been confirmed, they are believed to be reflections in the optical path of the SiPM, possibly caused by the reflective interior of the SiPM enclosure.

M. Sadik, PhD, Thesis, Aston University, 2023

These so called reflections were more apparent on the measurements done at a bias of 33.4V compared to those performed at a bias of 34.9V.
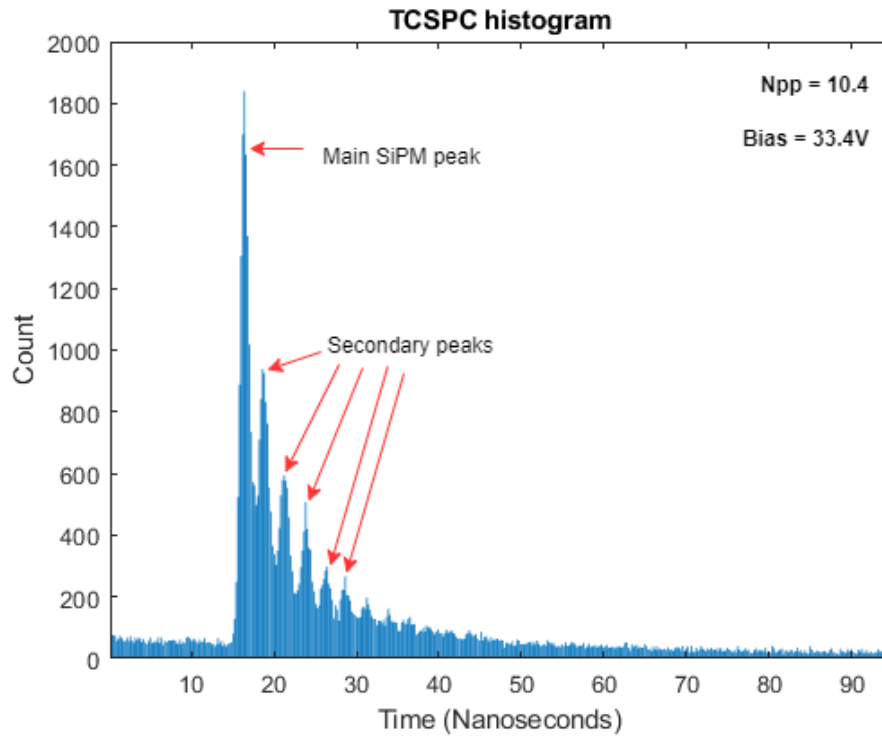
Figure 30: TCSPC measurement performed using SiPM experimental setup with secondary peaks found in measurement highlighted. Performed at a bias of 33.4V for a mean photon number of 10.4

M. Sadik, PhD, Thesis, Aston University, 2023
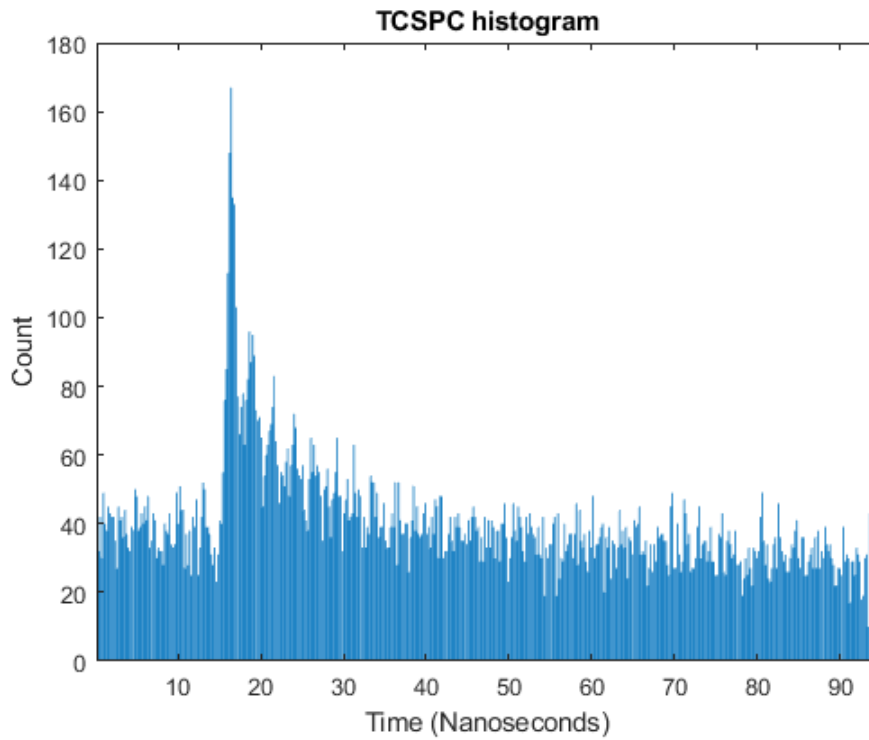
Figure 31: TCSPC measurement with SiPM at bias 33.4V at Npp = 0.5
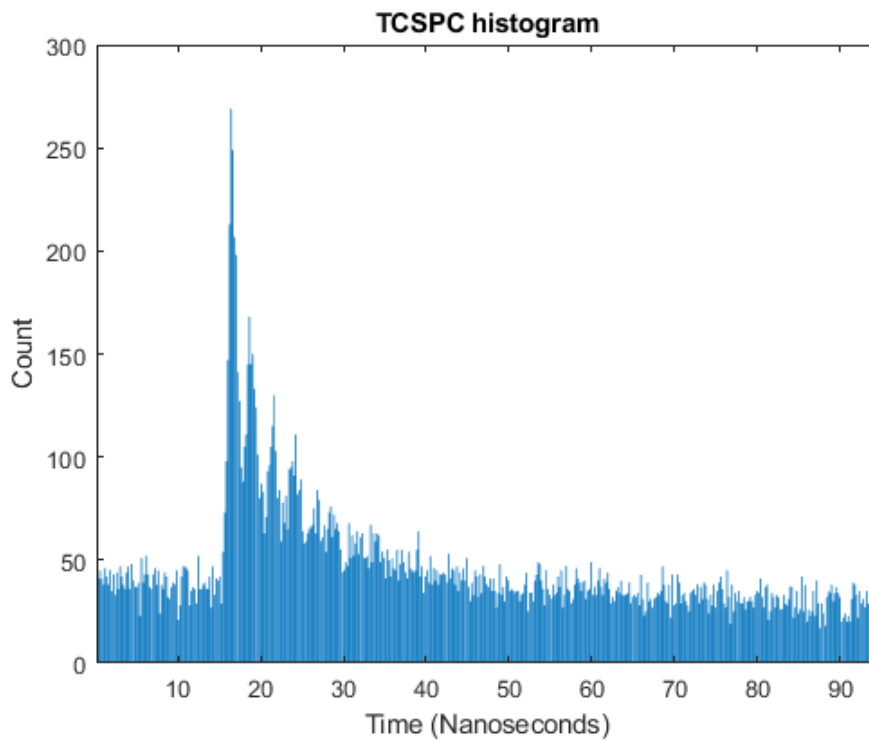
Figure 32: TCSPC measurement with SiPM at bias 33.4V at Npp=1.0
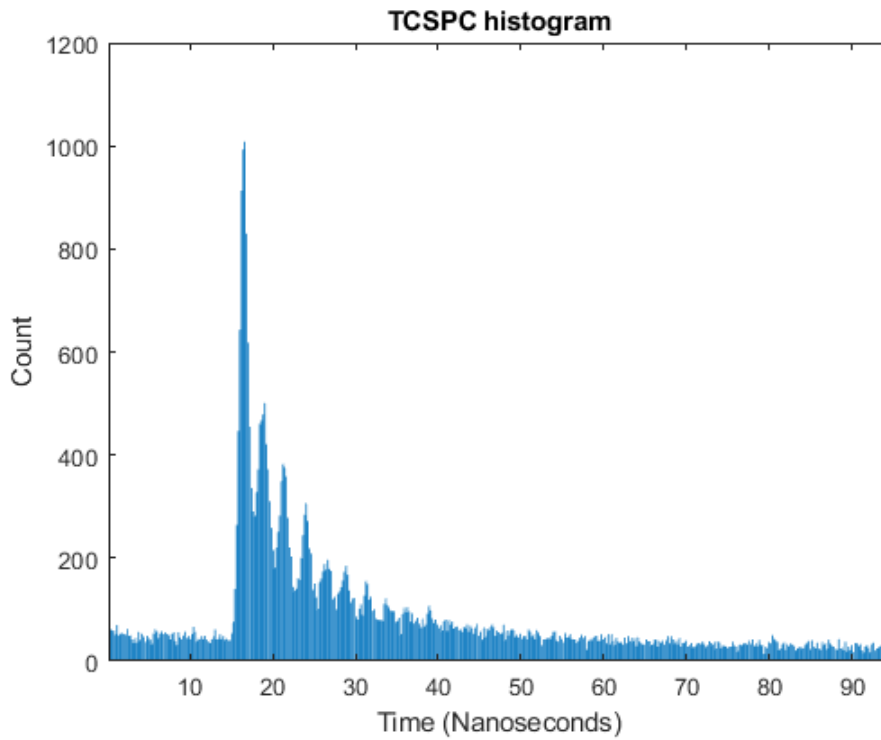
Figure 33: TCSPC measurement with SiPM at bias 33.4V at Npp = 5.2
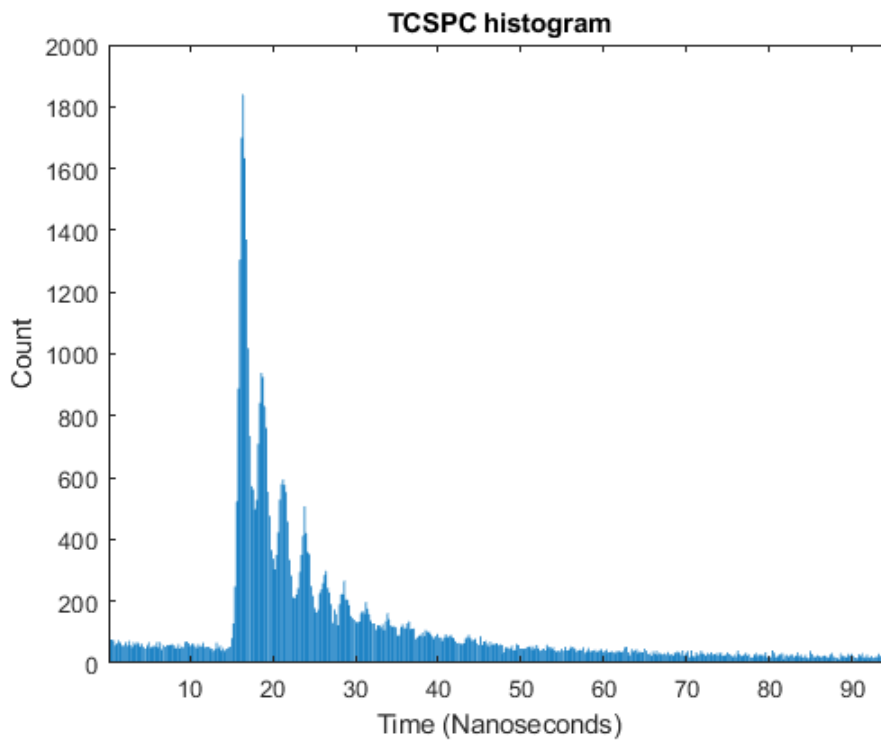
Figure 34: TCSPC measurement with SiPM at bias 33.4V at Npp = 10.4

The measurements for the SiPM were also done at a different bias voltage of 34.9V (8.5V overvoltage) where the dark count rate of the detector was measured to be 2.64 MHz and the crosstalk probability was estimated to be around 60% (section 3.3.3). The measurements performed were done using the same experimental setup as before with only the bias voltage being changed. Looking at the count rates at this bias voltage, shown in Figure 35, we can observe the same trend as we did with the lower bias voltage where the SiPM count rates increase in a linear fashion until it nears $N_{pp} = 10$, at which point it starts to go non-linear confirming our previous acceptable working range.
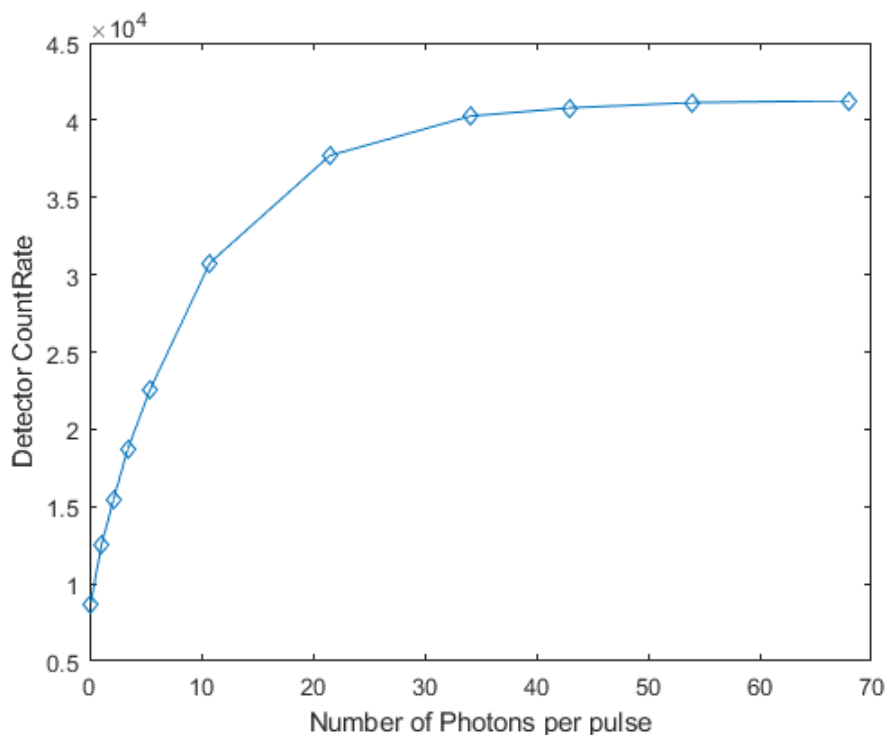
Figure 35: Measurement of SiPM Count rates (per 4ms period) for varying Npp values, biased at 34.9V

When looking at the results of the TCSPC measurements for this bias voltage, we can observe that the detector can resolve the waveform at a photon rate of 0.1 with the peak being clearly visible, unlike when the bias was set to 33.4V, as shown in Figure 36. Although the peak can be detected, the full shape of the waveform is still hidden behind the high noise floor. Once the light levels were slowly increased up to the maximum acceptable working range of light levels that was characterised for the SiPM, the waveform became more distinguished as the correlated counts started to overshadow the noise in the histogram (as signal to noise ratio increases). This can be seen in Figure 36 to Figure 39, where the photon rate is increased up to $N_{pp} = 10$ and the noise

M. Sadik, PhD, Thesis, Aston University, 2023

in the correlation can be seen to no longer affect the measurement with the full waveform becoming more and more visible. The number of counts in the peaks of the histograms were measured to be up to 97% higher for a bias of 34.9V than they were at 33.4V. However, this is to be expected as the PDE and responsivity of the SiPM increases at higher values of overvoltage while the noise also increases [68].
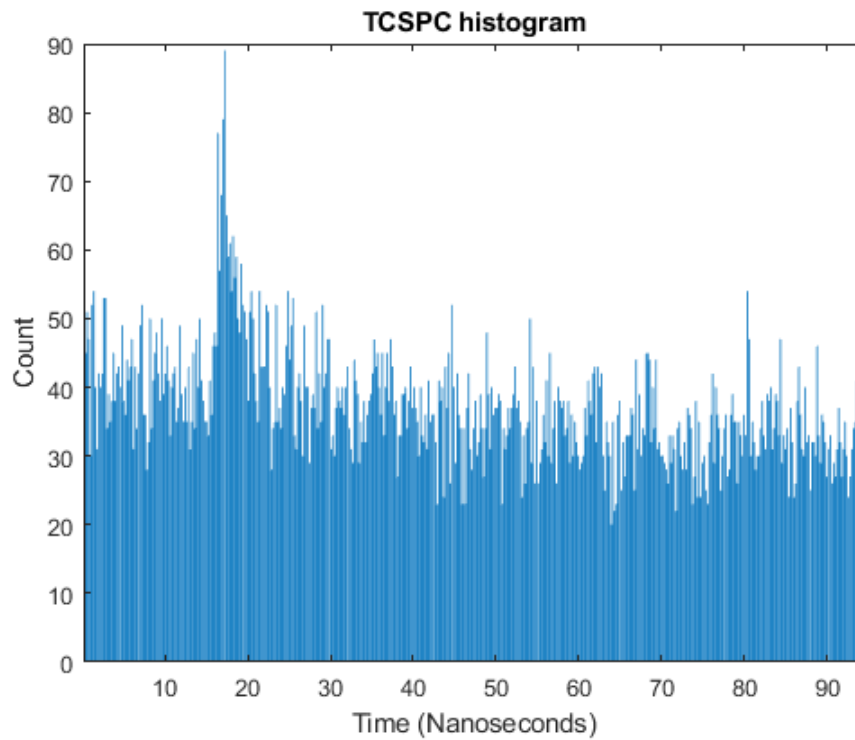
Figure 36: TCSPC measurement with SiPM at bias 34.9V at Npp = 0.1
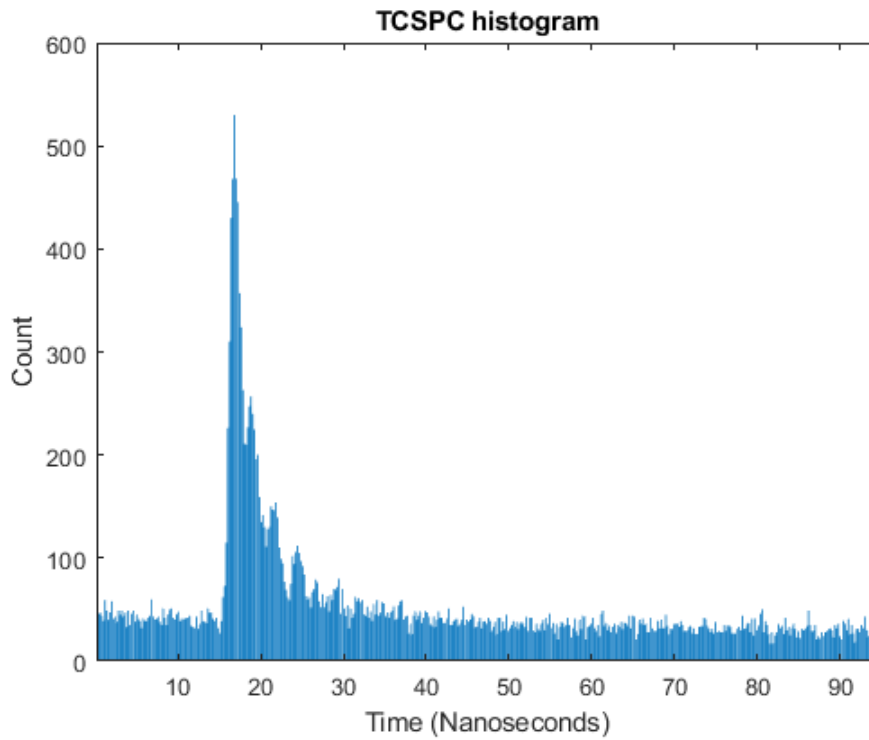
Figure 37: TCSPC measurement with SiPM at bias 34.9V at Npp = 1.0
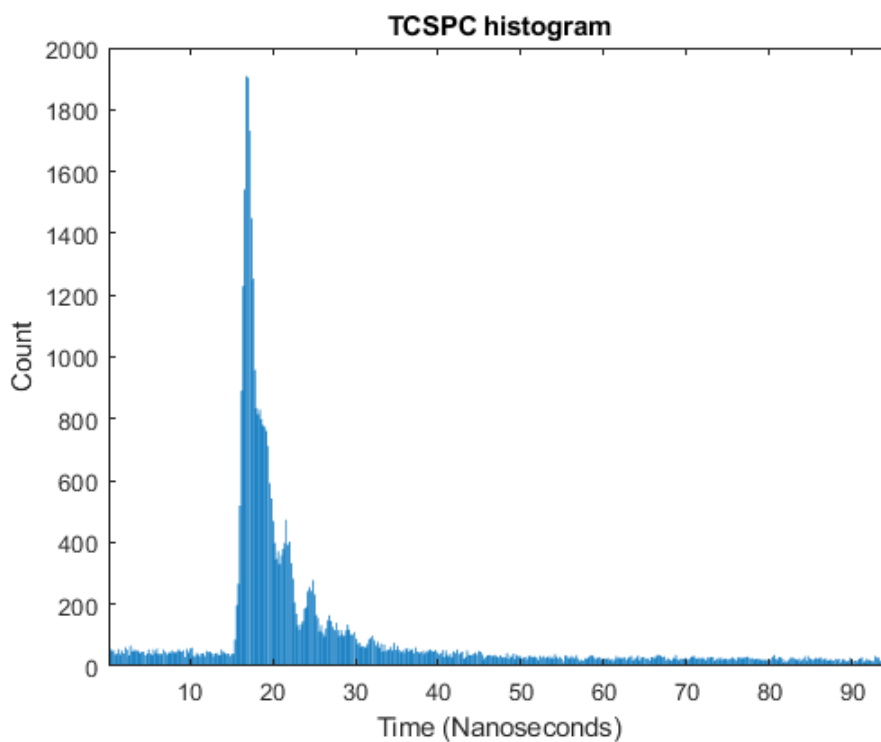
Figure 38: TCSPC measurement with SiPM at bias 34.9V at Npp = 5.4
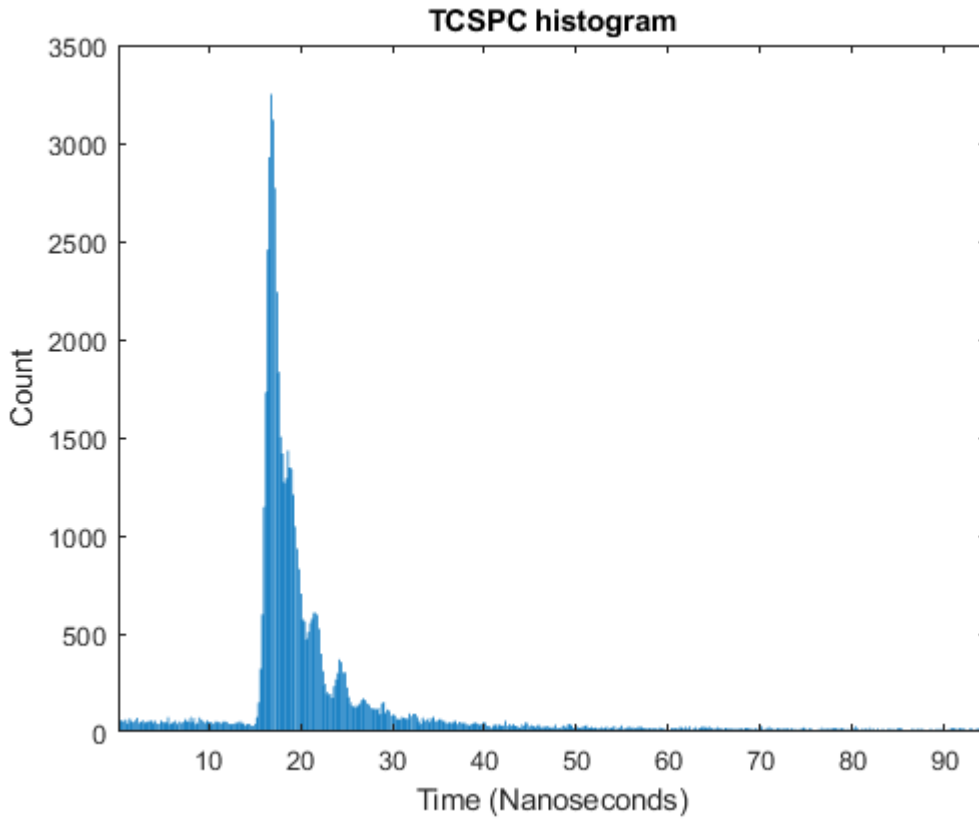
Figure 39: TCSPC measurement with SiPM at bias 34.9V at Npp = 10.7

The PDE of the detector was measured at the various light levels and was found to range from 8% to 11%. Note that the value of the PDE measured here is a product of the PDE of the SiPM and the coupling efficiency of the SiPM to the fibre port on the enclosure. The PDE was measured as of:

$$PDE = \frac{number\ of\ photons\ detected}{number\ of\ photons\ at\ the\ fibre} \tag{3.6}$$

The number of photons at the fibre was calculated from the multiplication of the number of photons per second (equation 3.2) and the transmission ratio, T, of the ND filtering used:

$$number\ of\ photons\ at\ the\ fibre = T \cdot N_{\frac{photons}{sec}} \tag{3.7}$$

3.3.6 Silicon photomultiplier amplitude spectrum

In [86] the author characterises their SiPM, showing that the detector was able to resolve different pulse amplitudes corresponding to the different number of simultaneous detections. This was also done by the author in [87] where they characterised their SiPM for the different photon event

M. Sadik, PhD, Thesis, Aston University, 2023

amplitudes and found up to nine distinct photon events that was later used for faster acquisition of histogram data for Raman spectroscopy. The author calls this technique time correlated photon counting (TCPC) as unlike TCSPC more than a single photon can be detected within a single excitation pulse due to the detectors ability to resolve photons.

In this section the SiPM amplitudes are investigated for use in applications of TCPC. The SiPM amplitudes were examined while using brief pulses of light at $N_{pp} = 2.3$. By histogramming the occurrences of the various amplitudes in the recorded signals using MATLAB scripts, the amplitudes corresponding up to four photon events were able to be characterised. The amplitudes were determined to be within a range of values after analysing the amplitude spectrums for each of the various bias voltages of the SiPM as shown in Table 1.

Bias voltage	$N_{photon} = 1$	$N_{photon} = 2$	$N_{photon} = 3$	$N_{photon} = 4$
33.4	100 – 135 mV	135 – 175 mV	175 – 210 mV	210+ mV
33.9	105 – 150 mV	150 – 185 mV	185 – 230 mV	230+ mV
34.4	110 – 155 mV	155 – 195 mV	195 – 245 mV	245+ mV
34.9	115 – 165 mV	165 – 205 mV	205 – 255 mV	255+ mV
35.4	120 – 170 mV	170 – 210 mV	210 – 265 mV	265+ mV
35.9	125 – 175 mV	175 – 215 mV	215 – 275 mV	275+ mV
36.4	130 – 185 mV	185 – 225 mV	225 – 290 mV	290+ mV

Table 1: Photon event amplitude values determined for the SiPM for bias voltages of 33.4V to 36.4V (overvoltage of 7-10V)

As the value of overvoltage is raised for the SiPM, the value of the gain also increases [45, 68]. The gain is a measurement of the number of charge carriers released when a photon is successfully detected which influences the pulse amplitude of the SiPM signal. Hence, as the bias voltage of the SiPM is increased, the signal amplitude will be higher. For this reason, when using the SiPM with TCPC, the amplitude values for the four photon events must be determined at the bias voltage being used. The histograms showing the amplitude spectrum of the SiPM pulses at the various bias voltages measured are shown in Figure 40 to Figure 46 where the shifting of the amplitude values can be observed.
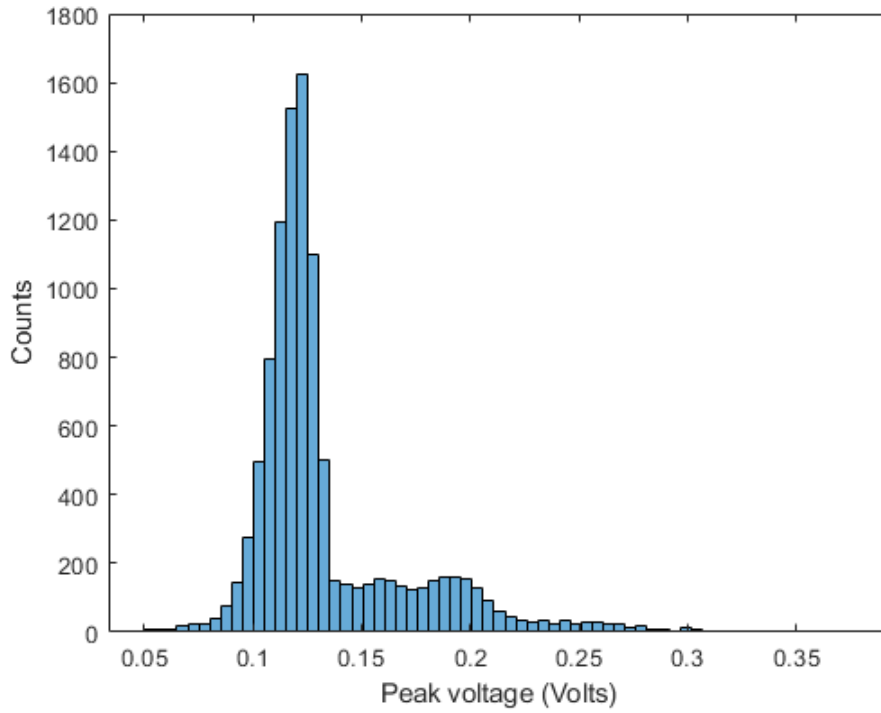
Figure 40: Amplitude spectrum of SiPM pulses at a bias voltage of 33.4V
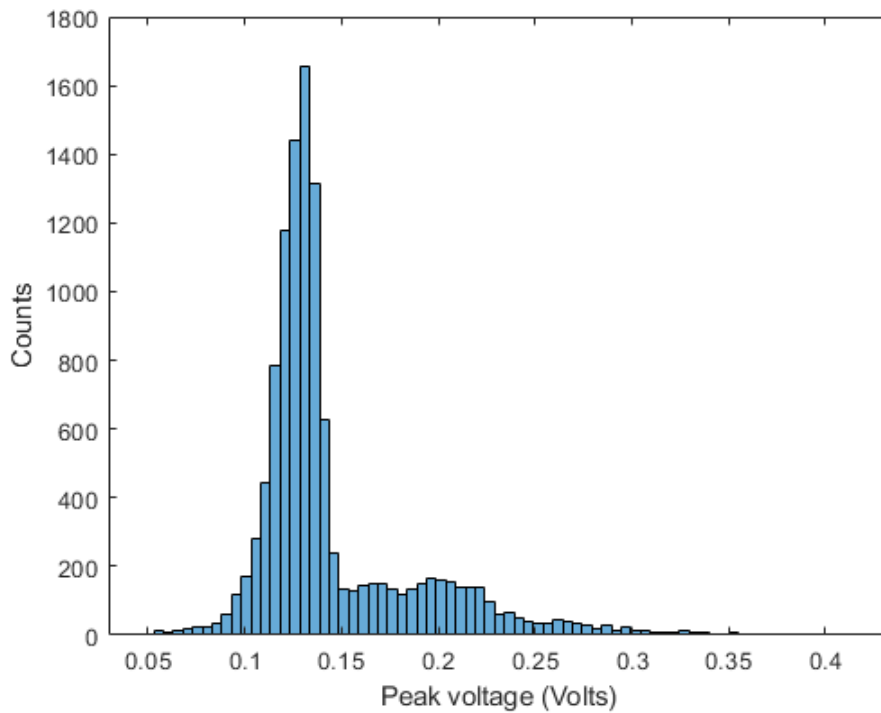
Figure 41: Amplitude spectrum of SiPM pulses at a bias voltage of 33.9V
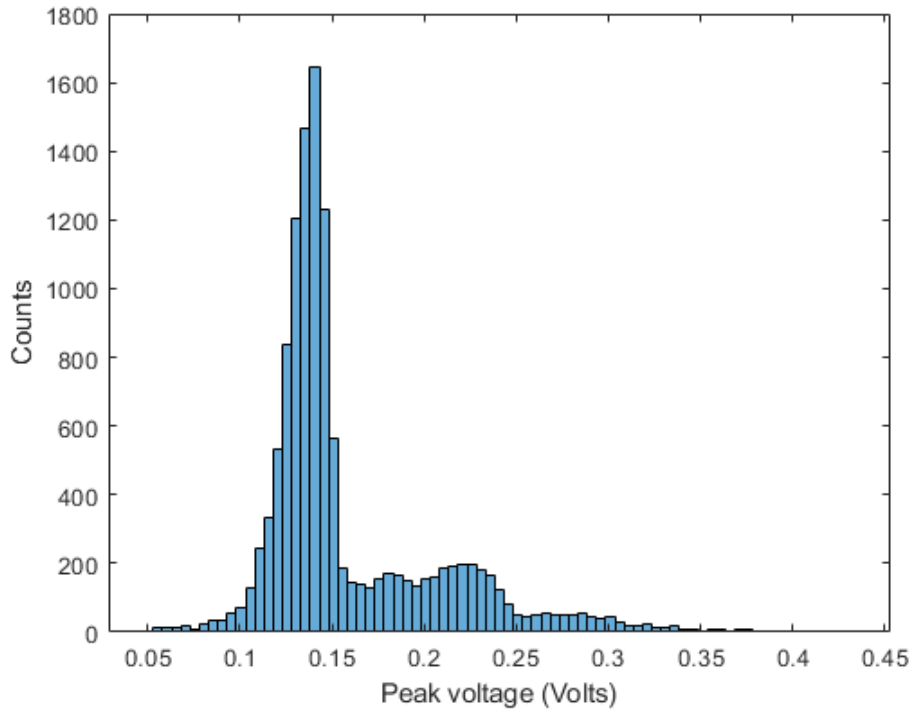
Figure 42: Amplitude spectrum of SiPM pulses at a bias voltage of 34.4V
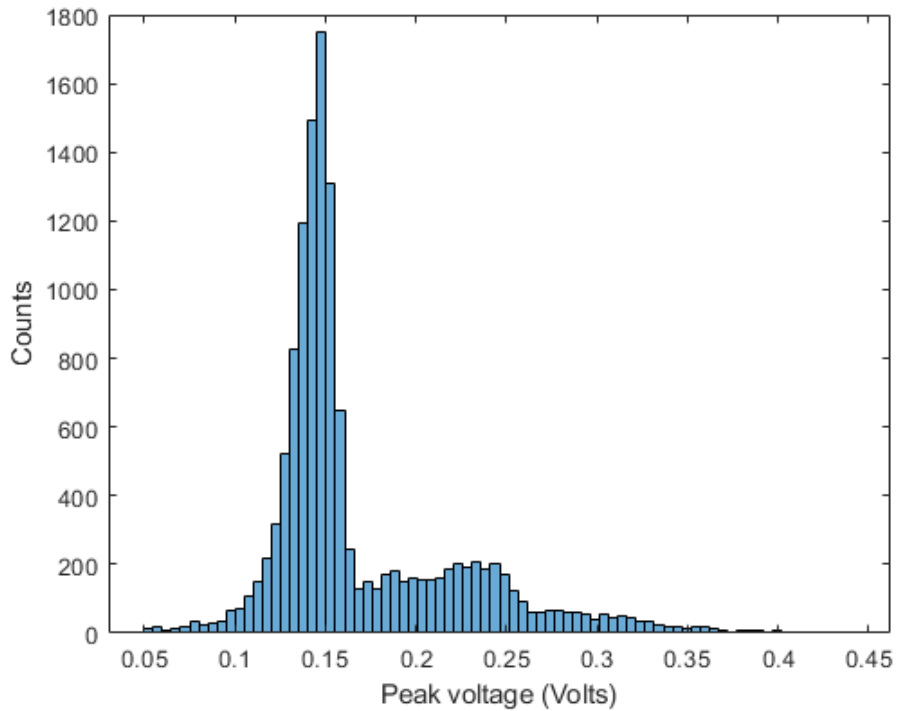
Figure 43: Amplitude spectrum of SiPM pulses at a bias voltage of 34.9V
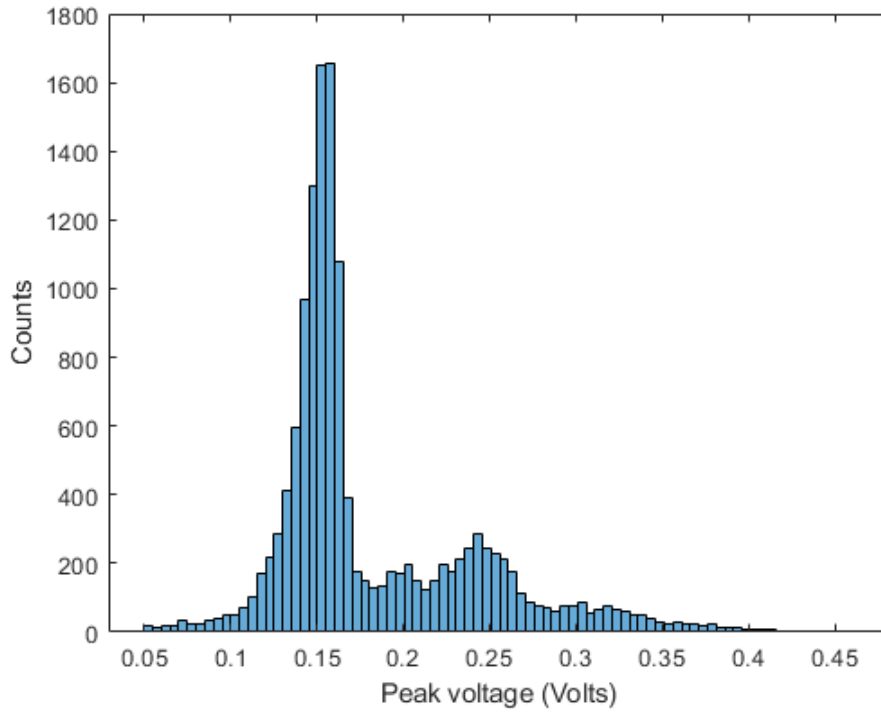
Figure 44: Amplitude spectrum of SiPM pulses at a bias voltage of 35.4V
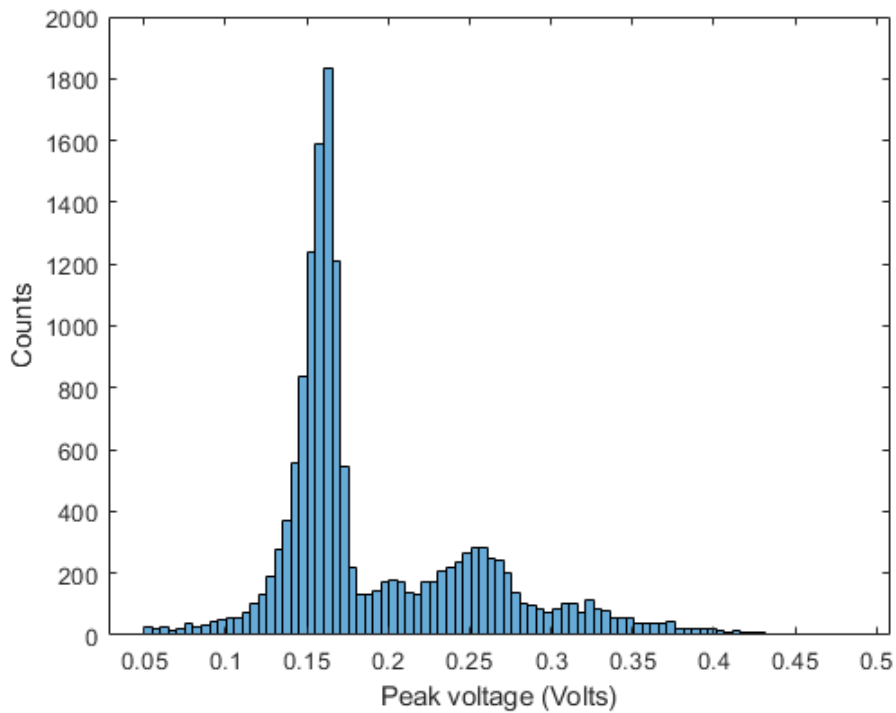
Figure 45: Amplitude spectrum of SiPM pulses at a bias voltage of 35.9V

M. Sadik, PhD, Thesis, Aston University, 2023
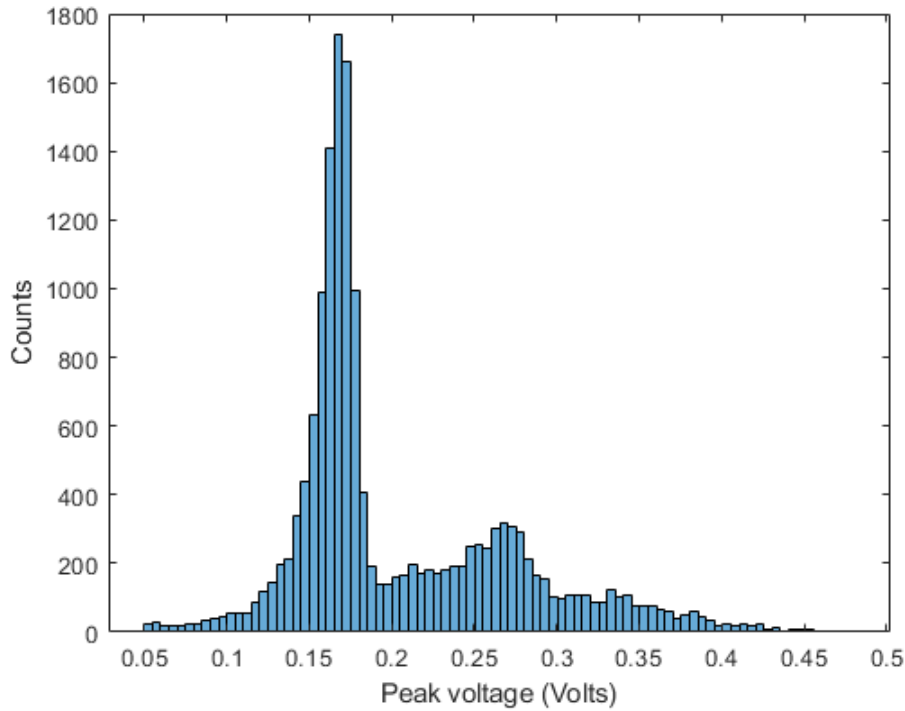
Figure 46: Amplitude spectrum of SiPM pulses at a bias voltage of 36.4V

3.3.7 Summary

This section focused on the work done to characterise an onsemi MicroRB-10035 SiPM for applications of photon counting utilising photon number resolving detectors. At first, an enclosure was built for the SiPM along with the necessary components needed to operate it. This included an adjustable power supply such that the bias voltage of the SiPM could be manipulated with ease, amplifiers for the SiPM signal, and a bias tee used to offset the negative going pulses of the detector. Once this had been done, the noise in the SiPM was characterised in the form of dark count and crosstalk. The SiPM was then illuminated via a pulsed laser while adjusting the light levels going to the detector through ND filtering to control the photon probability for applications of photon counting. Data for the SiPM was gathered via an oscilloscope and was used in conjunction with MATLAB scripts to perform TCSPC measurements with the SiPM at the various light levels. Finally, the amplitude spectrum of the SiPM pulses were studied to determine the threshold values for the various photon events.

M. Sadik, PhD, Thesis, Aston University, 2023

3.4 Conclusion

The work done in this chapter was towards the characterisation of an onsemi MicroRB-10035 SiPM for applications of photon counting. The first task towards this goal was the construction of an enclosure to house the SiPM along with the electronics needed to operate it. The dark count rate and the crosstalk of the SiPM have been measured and presented for a range of overvoltage values from 7V to 10V. The count rates of the detector were measured at various light levels to determine the point when the detector saturates from over exposure. From this, an acceptable working range of light levels was compiled and TCSPC measurements were performed using the SiPM within this range at two different bias voltages. The results showed the SiPM being incapable of resolving the shape of the waveform at a photon probability rate of 0.1, which is the optimal rate for SPADs, due to the amount of noise in the correlation. At higher light levels, the SiPM was observed to be able to resolve the correlated from the background noise.

It has been shown that the SiPM is capable of photon number resolving, where unlike traditional single photon detectors more than a single photon can be resolved within a pulse due to their array like structure. The pulse amplitudes of the detector were then studied at the different bias voltages, deriving from them the pulse amplitudes corresponding to multi photon events.

4.0 Time to digital converters, time correlated single photon counting and photon number resolving instrumentation

4.1 Introduction

The concept of time correlated photon counting (TCPC) is an extension of that of TCSPC adding the capability for multiphoton detection with photon number resolving detectors. First mentioned in [87] where the author uses it for time correlated Raman spectroscopy, TCPC makes use of the photon number resolving capabilities of a SiPM to infer the number of photons within any incoming SiPM pulse (also referred to as a 'click') which enables faster acquisition of histogram data, as for each excitation pulse the exact number of photons can be added to the appropriate histogram bin. Given the structure of the SiPM, which can be thought of as a passively summed array of passively quenched SPADs (referred to as microcells), the limiting effects of a detector dead-time in TCSPC are reduced. This is because each subsequent photon landing on the SiPM (or similar array based detector) will randomly land on microcells in the array, with the probability of landing on a microcell experiencing dead-time being small. The array structure allows for higher light levels to be utilised per excitation pulse in which more multi-photon events can also be inferred, which results in a far greater detector dynamic range. Due to these factors, utilising TCPC with a SiPM can forgo the standard 5-10% detector count rate limit (of excitation frequency) imposed in TCSPC due to the pile-up effect [115] allowing for higher photon probability rates per laser pulse to be used with the detector explored in chapter 3.

This chapter goes over the instrument that has been developed as part of this work that performs TCPC measurements in real time. The amplitude information within a SiPM pulse is quantised by hardware to determine the number of photons present within a pulse with 4 distinct quantisation levels, allowing for more histogram data to be acquired within a single excitation pulse. While the original author of the TCPC paper [87] had performed TCPC measurements using a SiPM, this was done through post processing of oscilloscope data. This chapter goes over the instrument design and performance along with an experimental comparison performed on the hardware between TCSPC and TCPC using the onsemi RB-Series 10035 SiPM characterised in the previous chapter.

M. Sadik, PhD, Thesis, Aston University, 2023

4.2 Hardware developed

The instrument developed during this work is an FPGA based time correlated photon counting (TCPC) system to be used for performing time correlations/range measurements using a SiPM, taking advantage of its photon number resolving capabilities. The instrument could also be operated as a time tagger, which in addition to measuring the time of an input pulse, it also measures the input amplitude with a custom fast 2-bit ADC.

The instrument was developed on a ZTEX USB-FPGA module 2.16 containing an Artix7 200T FPGA on which time measurements are taken via two on board TDCs, one each for the START and STOP channels. The STOP channel is put through additional amplitude quantisation circuitry (discussed further in section 4.4) as this is the channel designed to pass through the SiPM signal's amplitude as well as time of arrival. A block diagram showing the various hardware modules of the instrument can be found in Figure 47 and a photograph of the instrument is presented in Figure 48.
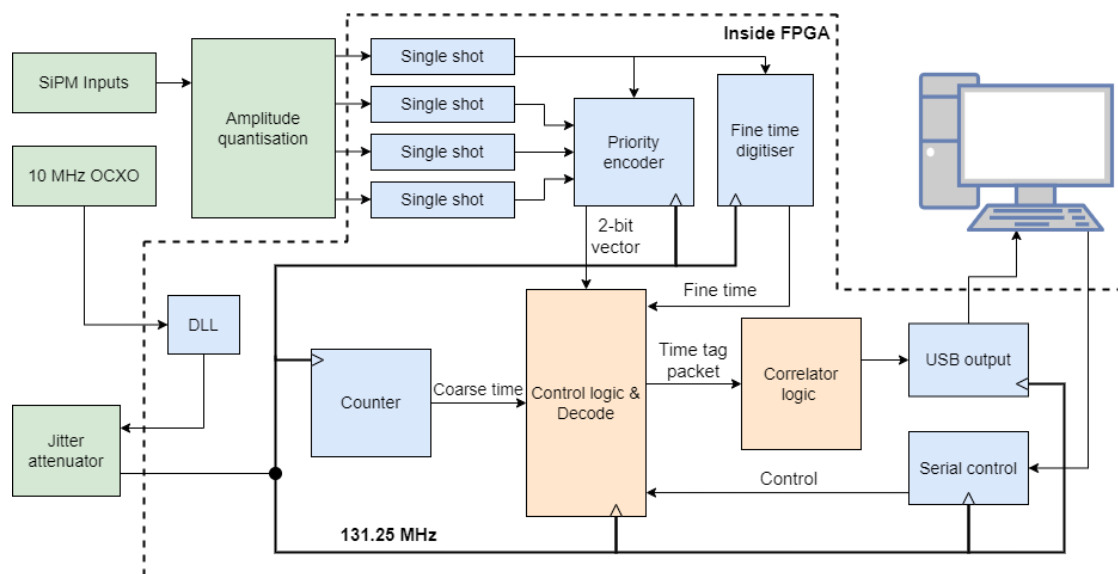
Figure 47: Block diagram of TCPC instrument

The clock for the FPGA is provided by a stable 10 MHz oven controlled crystal oscillator (OCXO) which is then internally increased to 130 MHz inside the FPGA using a delay locked loop (DLL) [116]. Finally, a jitter attenuator [117] is utilised to reduce the jitter from the clock signal generated by the DLL as jitter on the clock could negatively affect the TDCs precision. Due to the nature of

M. Sadik, PhD, Thesis, Aston University, 2023

the jitter attenuator used, the frequency of the final clock signal was slightly increased to 131.25 MHz. This clock source is used for most of the system components including the TDC and correlator. Some parts of the design, such as the USB bulk-transfer interface, are clocked at 48 MHz using the clock from the Cypress FX2 microcontroller present on the ZTEX FPGA module. First in first out (FIFO) buffers are used to cross the clock domains.
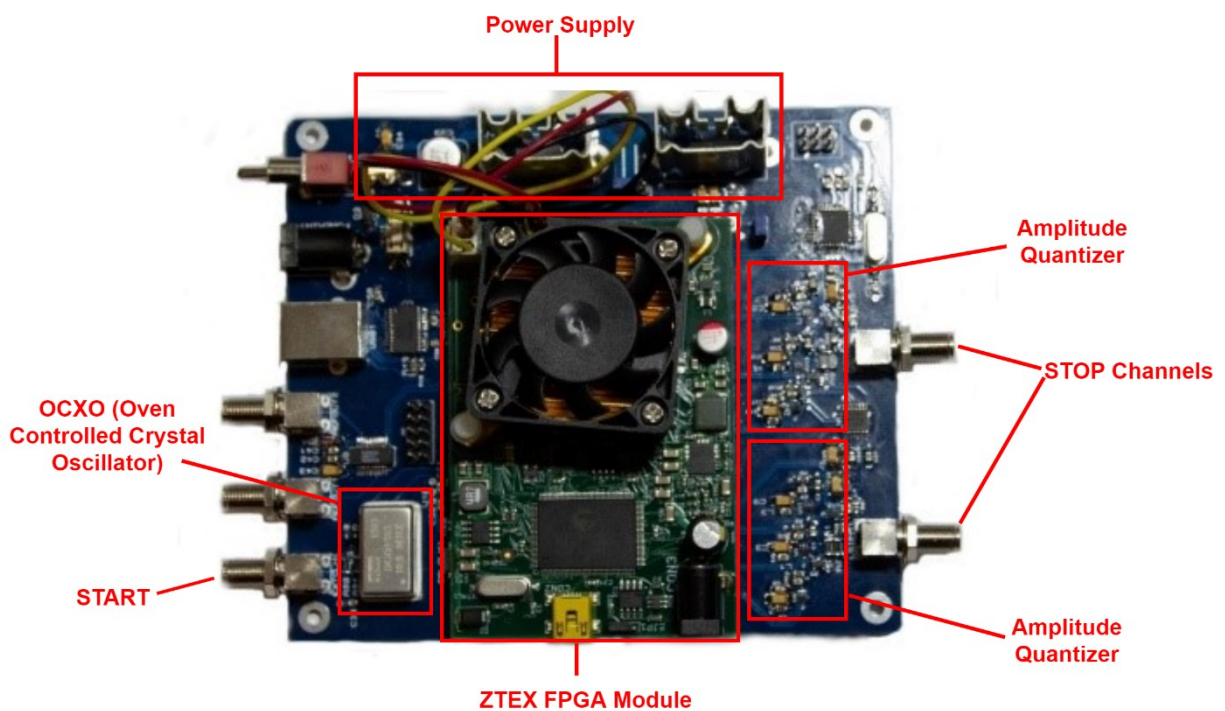
Figure 48: The hardware platform developed during this work showing the main system components

Inside the FPGA, single shot circuitry is used to hold the result from the quantizer signal while the TDC measures the time information, and the priority encoder resolves the 2-bit amplitude vector. The input quantizer can be thought of as a 2-bit ADC, constructed from high-speed Low-Voltage Differential Signalling (LVDS) output comparators [118]. A microcontroller and a 12-bit DAC allow for the transfer function of the ADC to be controlled via software to a resolution of 1.22mV, through a RS232/serial communication link. This is vital, as each step in ADC's transfer function needs to be adjusted to account for the detector's amplitude spectrum for varying photon number events.

If a comparator in the quantizer detects an input is above a threshold, the comparator will output a high-level output signal. As the signal pulses from the SiPM are relatively short in comparison to the FPGA's approximate 7.6ns clock period, single shot circuits will store the value until being reset. A block diagram of the single shots is shown in Figure 49. The input is routed the clock pin

M. Sadik, PhD, Thesis, Aston University, 2023

of a D-type flip flop while the D-input is held at VCC. This makes the flip flop trigger asynchronously from the TDC's clock which preserves the timing information. As the D input is held at VCC, it is impossible to violate the setup and hold time requirements of the initial flip flop. Two subsequent flip flops are used to reset the first flip flop. The output of the first single shot, at the single photon threshold, is passed to the TDC to measure the time of the click, as any click will always experience the single photon detecting comparator firing. At the same time, the outputs of all the flip flops are sent to the priority encoder, which encodes the 4-bit thermometer code into a 2-bit amplitude vector.
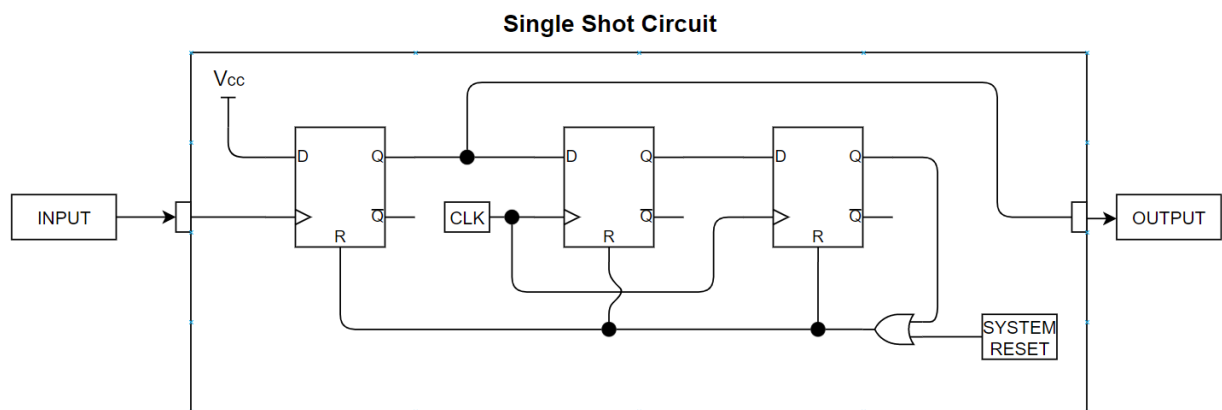
Figure 49: Single Shot Circuit block diagram showing the asynchronously triggered flip flop and the reset signal path

The rationale behind the use of the single shots is twofold. First, the detector pulses expected are much shorter than the ~7.6ns it takes for the TDC complete a measurement. Because of this the system is likely to miss events as the TDC looks for the rising edge transition across two clock cycles on the input to perform a measurement. The second reason behind their use is to ensure that the input signal is held long enough for it to be synchronised to the system clock such that the amplitude information can be reliably extracted with no issues regarding metastability.

The TDCs and correlator utilised in the FPGA design are a modified version of the TCSPC instrument developed in [63]. The VHDL project was ported over to the Artix7 platform and was modified into a TCPC instrument to accommodate the photon number resolving of a SiPM. This also required new hardware to measure the detector's pulse height. While there are two channels with amplitude quantisation circuitry included on the hardware platform, only one of these

M. Sadik, PhD, Thesis, Aston University, 2023

channels is used throughout this work with the VHDL code only supporting the one channel. The extra channel was placed there with future scalability in mind.

The instrument was controlled from a PC using a USB serial port powered by a FTDI FT232R that was routed to the FPGA. This provided a way to control and configure the instrument, allowing for the correlator state machine to be controlled without having to reprogram the FPGA. A Cypress FX2 microcontroller present on the ZTEX FPGA module is used for high throughput communication and configuration of the FPGA itself (bit file programming). Histogram data is sent to the PC via the Cypress FX2 microcontroller. A program written in C was used to provide a real time preview of the histogram data collected by the instrument for a single integration cycle while also saving the histogram data into a CSV file, which were then used along with MATLAB scripts to plot the data.

To power the instrument a 9V DC adapter was used in conjunction with a barrel connector on the printed circuit board (PCB). Protection circuitry was employed on the power supply to protect from overcurrent and reverse current. The DC input was used directly to power the FPGA module as it has onboard regulators that accept an input voltage of 4.5V-16V. The voltage was then reduced using linear regulators to 5V and 2.5V. Linear regulators were used to reduce noise on the critical 5V rail, which is used for all the components in the amplitude quantisation circuitry. The 2.5V was used to provide power to the IO bank voltage on the FPGA on which differential signalling was used to comply with the LVDS_25 standard on Xilinx FPGAs.

4.3 Time to digital converter developed

The TDC is an essential part of the hardware correlator platform as its performance can influence the precision of the measurements. A Nutt interpolation scheme is used for the TDC featuring a coarse timer clocked at the 131.25 MHz system clock and the fine time interpolators utilise the carry chain inside the FPGA. The SSP, linearity and transfer function of the developed fine time TDC have been measured and presented below.

The SSP of the TDC was measured by histogramming a 1 MHz signal from an HP8082A pulse generator applied between the START and STOP inputs using a 50Ω splitter from Mini Circuits [119] which effectively presented a small, fixed delay between the two signals due to the delay in the cables as in Figure 50. The result of this would be a measurement of the jitter of the system

and is shown in Figure 51 with the SSP measured with a FWHM of 107ps or 45ps RMS across two channels, which is a single channel precision of 31.8ps. In this case we assume that the jitter created by the 50Ω splitter is much less than the jitter of the instrument.
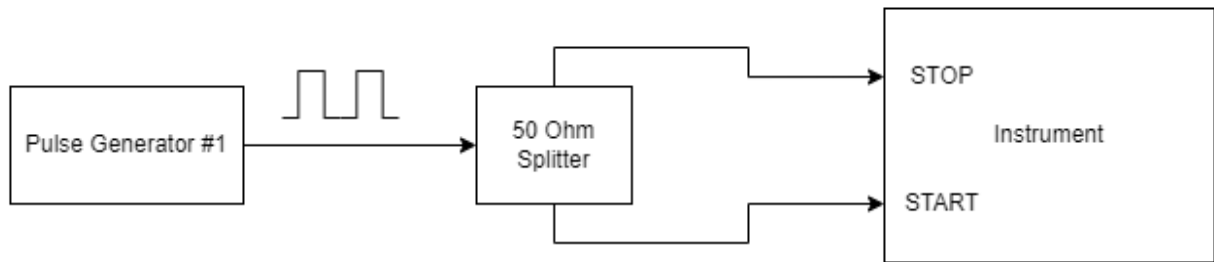
Figure 50: Diagram of experimental setup used for precision measurement
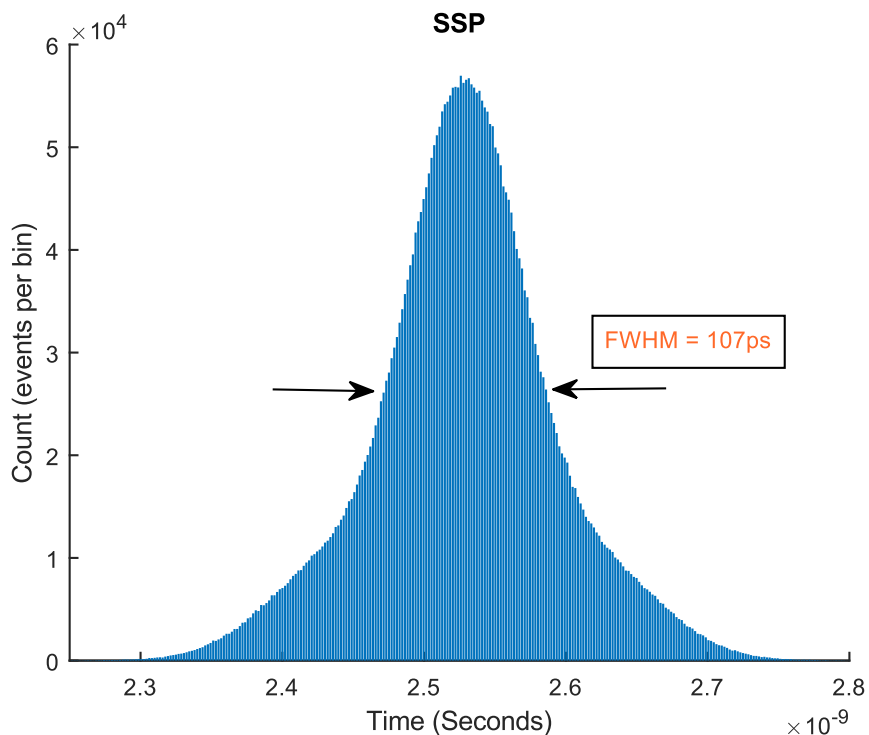
Figure 51: Time to digital converter single shot precision with FWHM = 107ps (45ps RMS)

The DNL and INL were measured by histogramming the raw TDC output codes (before SCDT calibration has taken place), which are an integer in the range of 0 to 511 generated by an asynchronous input signal from an external pulse generator with no phase relationship to the main OCXO used for the TDC, effectively performing a SCDT. This was repeated for 2^{24} (approximately 17 million) hits from the asynchronous signal. The DNL was measured at (-1, 9.18) as shown in Figure 52, while the INL was measured at (-2.33, 23.1) as shown in Figure 53.

M. Sadik, PhD, Thesis, Aston University, 2023

Furthermore, the transfer function of the SCDT is shown in Figure 54 where the bin positions relative to time are plotted. The TDC exhibits the ultra-wide bin phenomenon at approximately bins 80 and 280. This could be potentially improved by reducing the delay line length and through custom placement and routing on the FPGA.
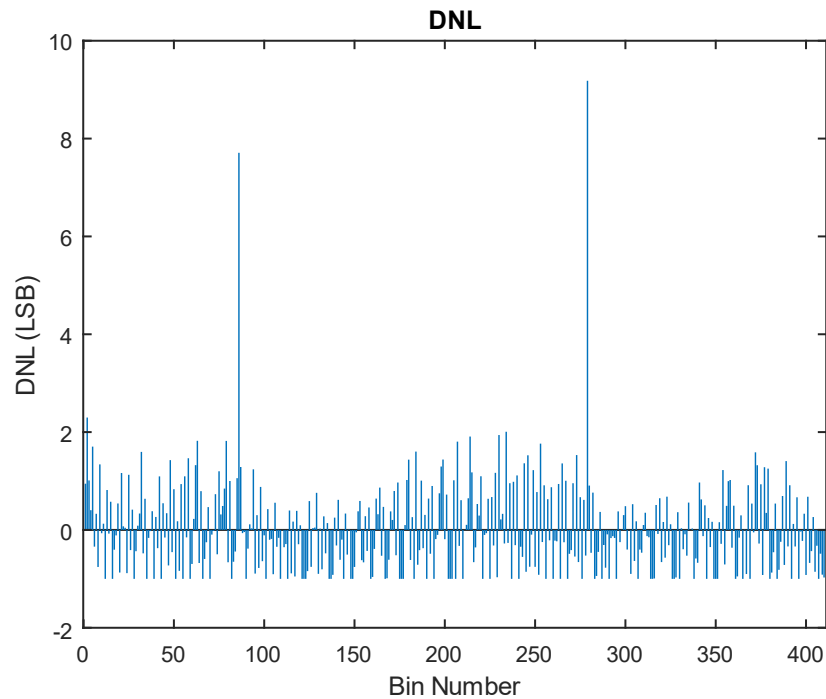
Figure 52: Time to digital converter differential nonlinearity measurement, DNL = (-1, 9.18)
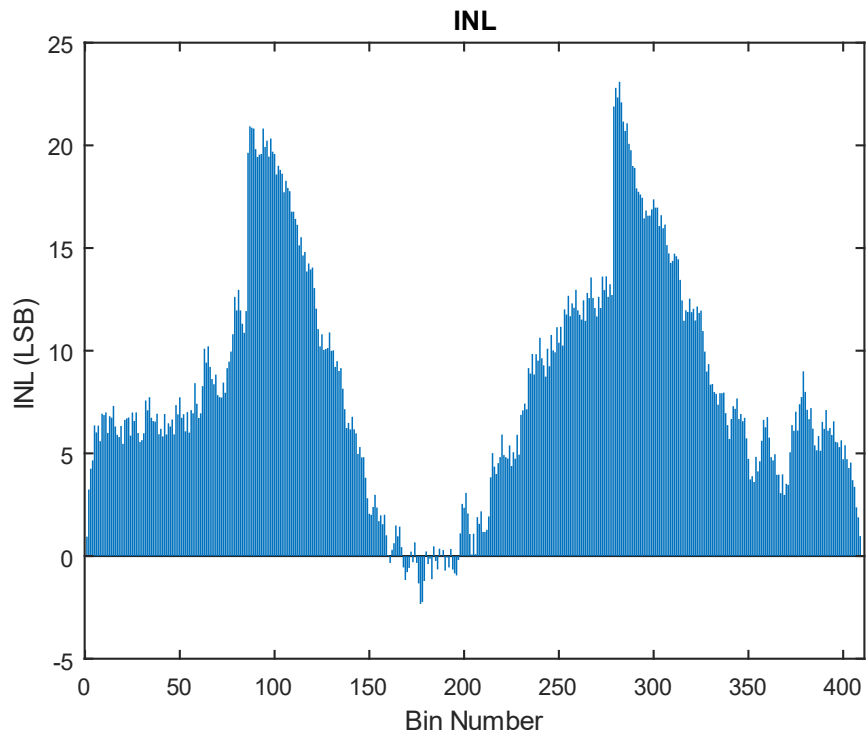
Figure 53: Time to digital converter integral nonlinearity measurement, INL = (-2.33, 23.1)
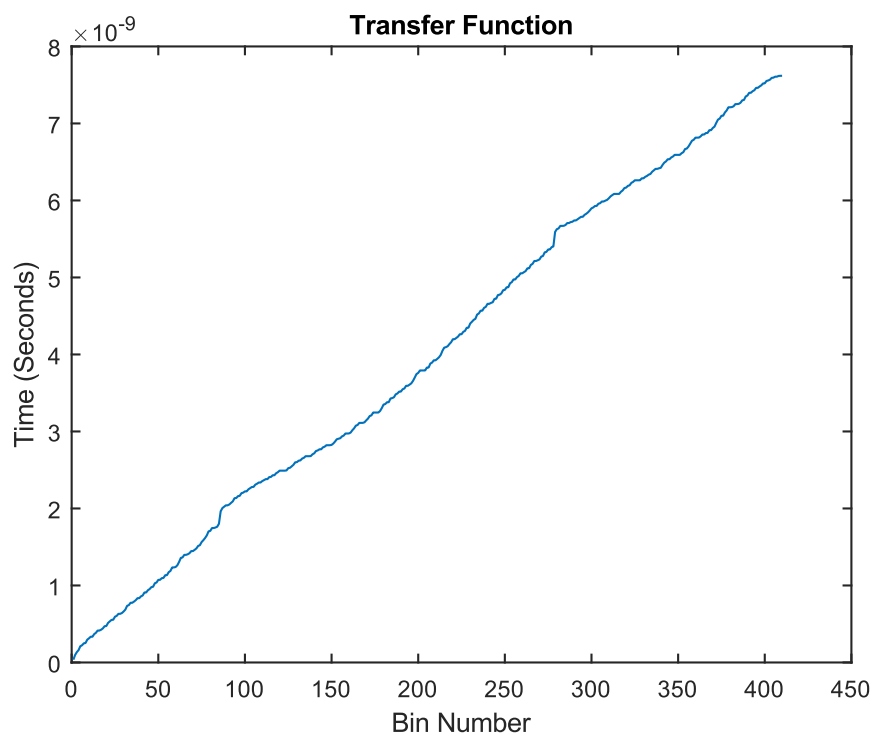
Figure 54: Time to digital converter transfer function showing bin number to time

4.4 Amplitude quantisation

The amplitude quantisation circuitry initially resistively splits the input signal from the SiPM and routes it into four ADCMP604 variable threshold comparators. The thresholds of these comparators are controlled by a 12-bit digital to analog converter (DAC) and are set during run time using an onboard ATMEGA328P microcontroller which is controlled on the PC side by a command line program that sends commands via the same FT232 USB serial port as the one used for configuring the correlator that was mentioned in section 4.2. The routing of the serial control from the microcontroller to the FT232 is done through the FPGA as the FT232 only has a single serial input. The extra microcontroller was used due to familiarity with the platform for an easier design and not an efficient one. This could be excluded in future revisions with the DACs being directly controlled by the FPGA.

By analysing the SiPM data from the oscilloscope, the amplitudes of the various SiPM pulses were determined in section 3.3.5. The peaks found in the histogram are assumed to correlate to the average amplitude values for the various N_{photon} levels and these values are then used to set the relevant threshold values of the comparators. Note that since only 4 comparators are used, any $N_{photon} \geq 4$ events will be treated as $N_{photon} = 4$ events.

The outputs of the comparators are then utilised as the inputs to the single shot circuits in the FPGA where a priority encoder then converts the thermometer code generated from the single shots into a 2-bit vector. This whole system can be considered a 2-bit flash ADC with user configurable step sizes for each bit. The 2-bit vector representing the amplitude information is appended to the TDC output where it then gets passed to the correlator along with the time information. The modified correlator then uses this 2-bit vector to determine the number of counts to add to the bin located at the given time difference.

M. Sadik, PhD, Thesis, Aston University, 2023
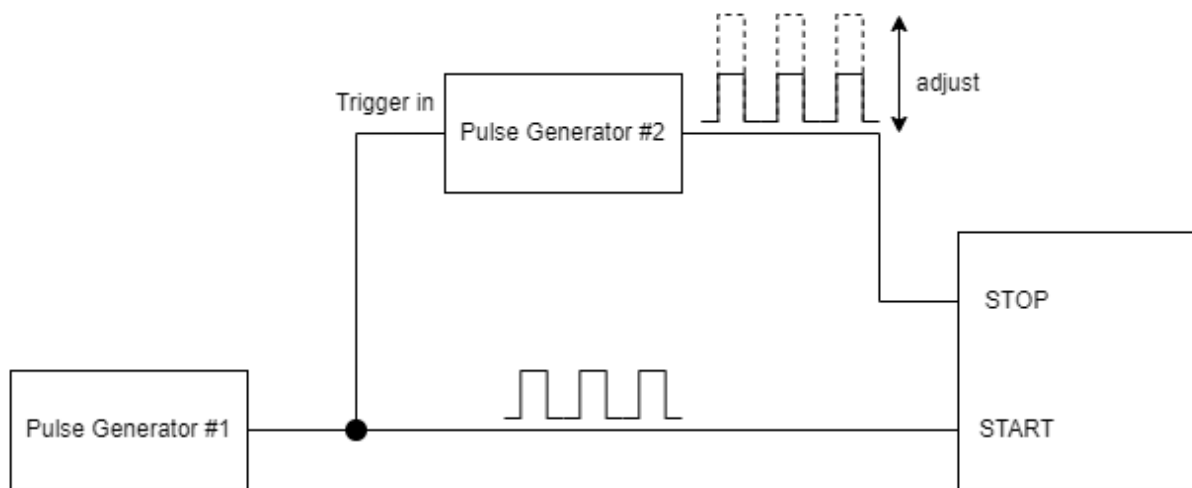
Figure 55: Experimental setup used when simulating multi photon events for correlator

To verify the correlator functioned as intended with the 2-bit vector, the counts in the histogram were monitored while simulating the various photon event levels. A signal from a pulse generator was presented to both the START input of the TCPC instrument and the trigger input of a second pulse generator. The second pulse generator output a delayed signal that was triggered using the first pulse generator and was presented to the STOP input of the instrument such that the amplitude could be adjusted to simulate the various multi photon events. A diagram showcasing the experimental setup is shown in Figure 55. The thresholds of the comparators were set to be 0.5V apart starting from 1V such that the STOP channel amplitude could be increased to simulate multi photon events. Hence, to simulate only single photon events the STOP channel amplitude was adjusted to a level between 1V and 1.5V. The STOP channel amplitude was then increased above 1.5V to simulate two photon events, above 2V to simulate three photon events and above 2.5V to simulate four photon events. The results of the correlations are shown in Figure 56 to Figure 59 where the counts in the histogram are seen to increase proportionally to the number of photons being simulated.
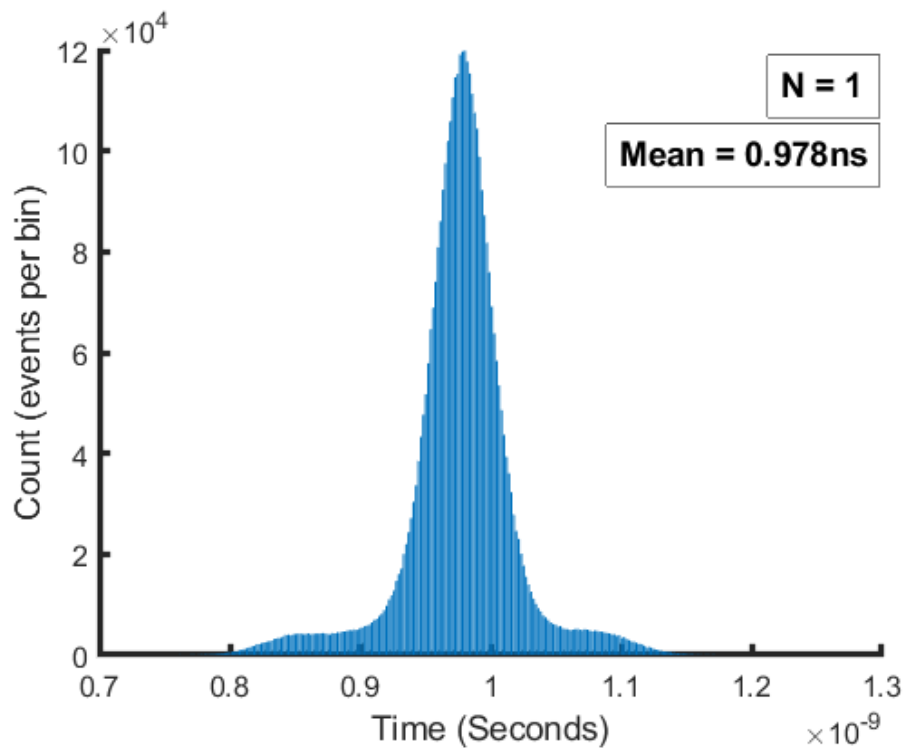
Figure 56: Measurement of simulated N=1 photon events using instrument
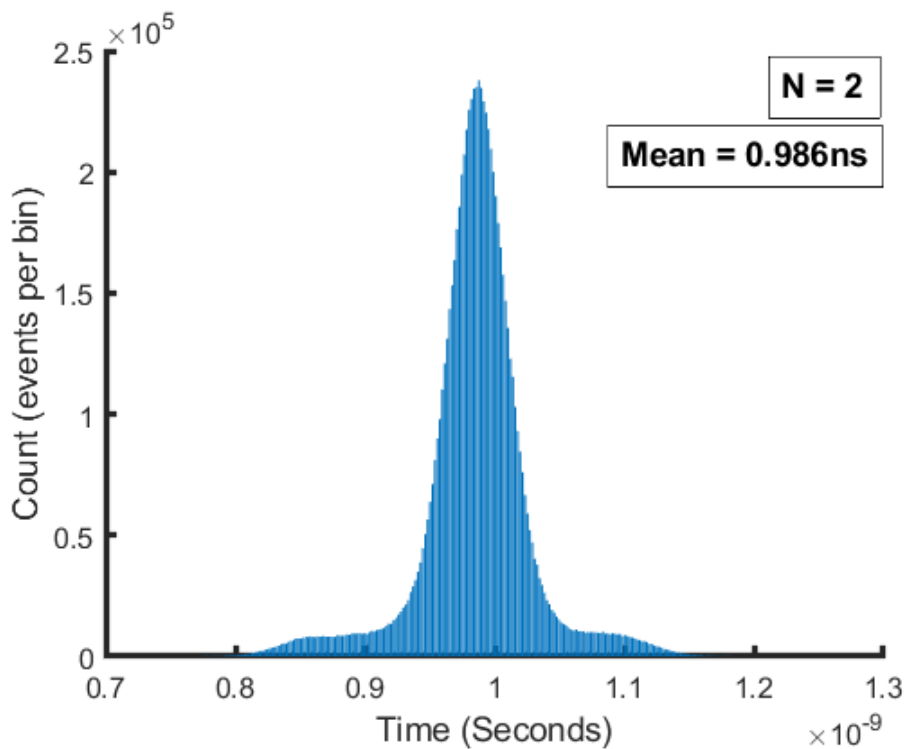
Figure 57: Measurement of simulated N=2 photon events using instrument

M. Sadik, PhD, Thesis, Aston University, 2023
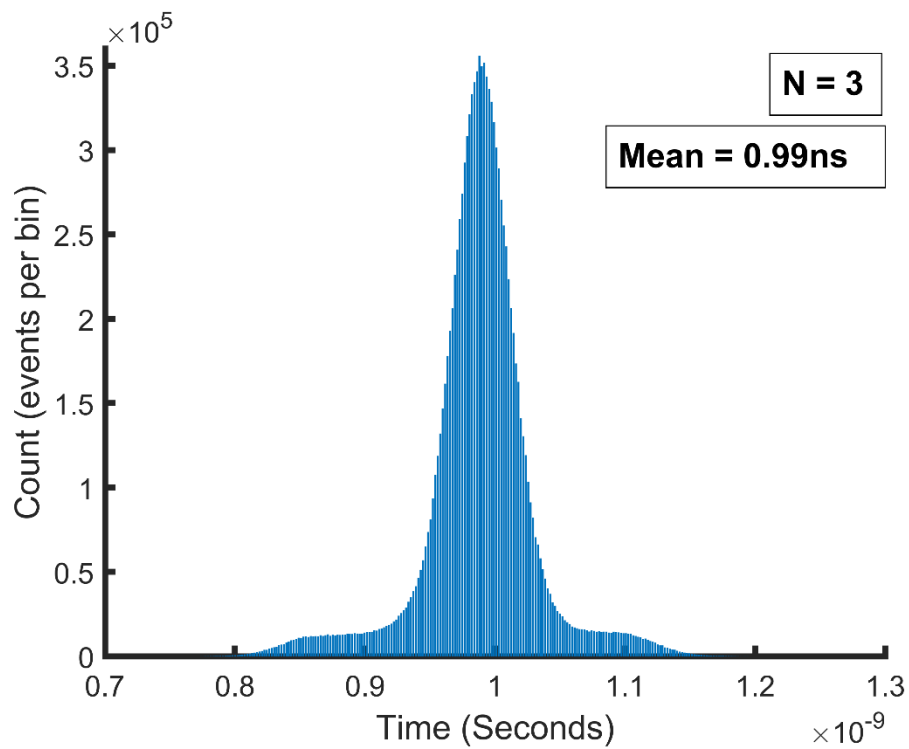
Figure 58: Measurement of simulated N=3 photon events using instrument
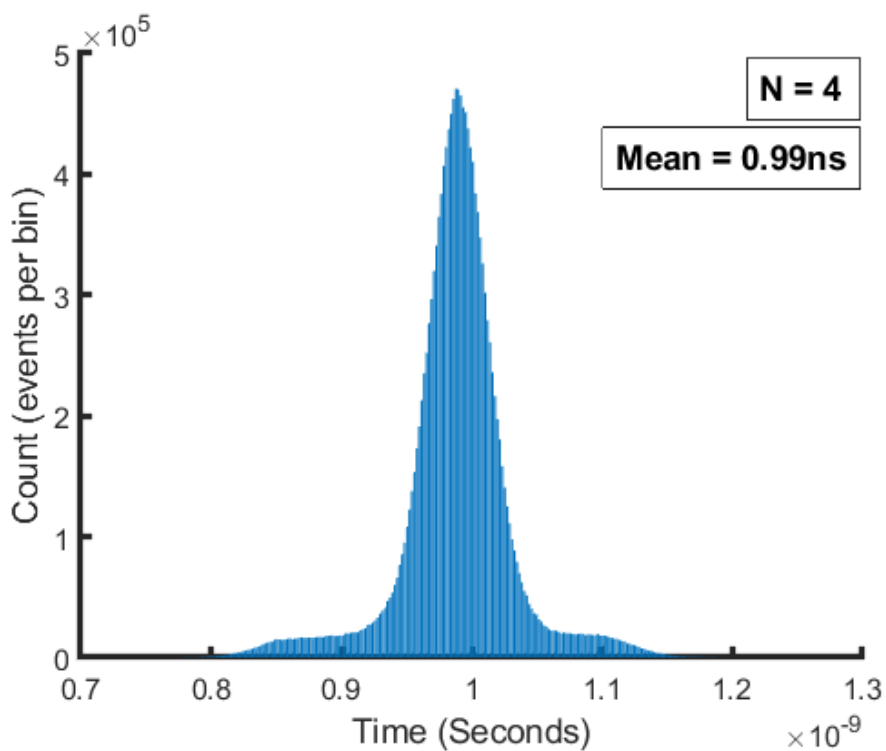
Figure 59: Measurement of simulated N=4 photon events using instrument

A mean shift can be noticed across the correlations of the various photon events. This is due to the constant level thresholding of the comparators which will always result in a time offset for varying input thresholds [120]. A method for mitigating this time offset within the FPGA correlator design was explored within this work, however, was not implemented into the instrument. The proposed method for the offset correction was to measure the mean shift from the single photon events to the two, three and four photon events when using the real values for the SiPM pulse amplitudes at the bias voltage being used for the comparator thresholds. These values could then be recorded in a look up table such that they could be used to subtract the mean shift from the time difference based on the value of the 2-bit amplitude vector as of:

$$\Delta T = STOP - START - (amplitude\ dependent\ mean\ shift) \tag{4.1}$$

4.5 Time correlated photon counting

The input to the modified correlator of the instrument was a circular buffer created out of dual port RAM. This allowed for tags from the TDC to be stored while the correlator was processing tags and forming the histogram. The histogram itself was created in the FPGAs block RAM, with the time differences from the TDCs being used as the addresses for the block RAM while the data at the address contains the number of counts at the relative bin. Figure 60 shows a block diagram depicting the path of the input to the correlator along with a visual representation of the process of building histograms in the modified correlator. When a new time tag is sent to the correlator to be processed it arrives along with the amplitude information. Once the time information is processed the correlator decides based on the amplitude information the number of counts to add to the relevant address in memory.
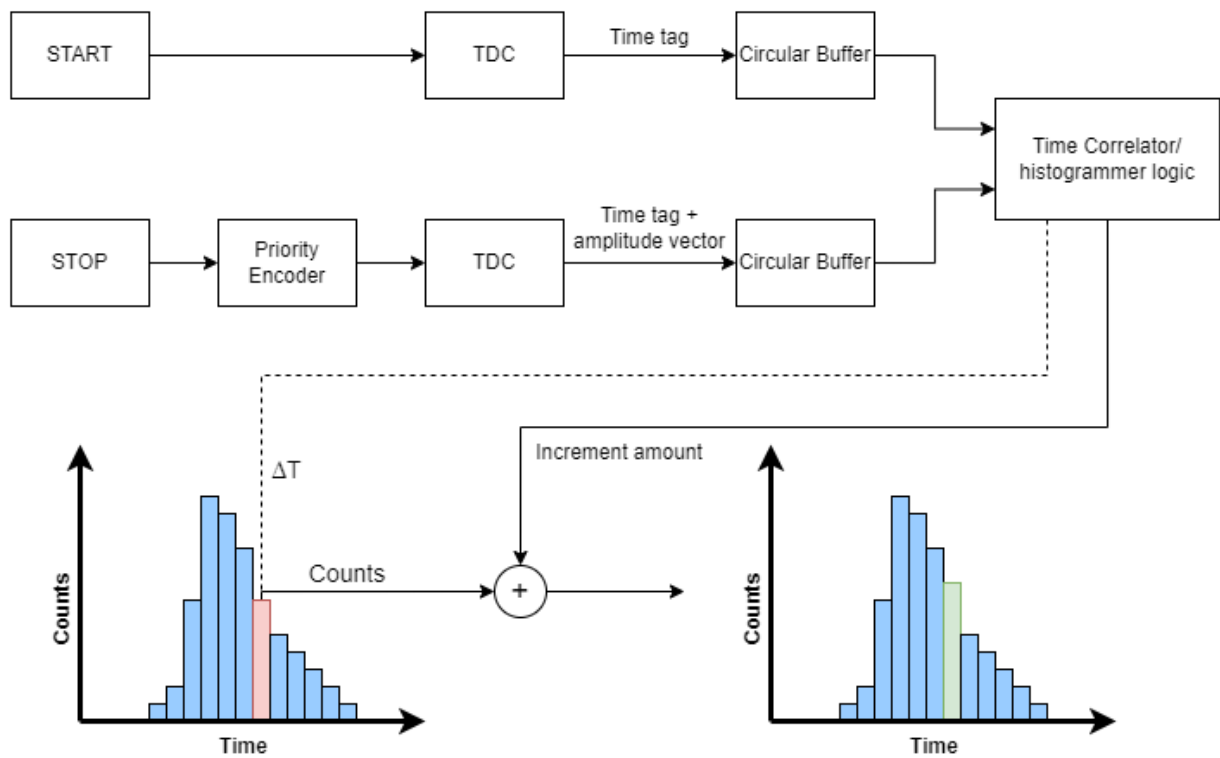
Figure 60: Correlator design of FPGA instrument showing process of building histograms in block ram

The instrument was used to perform TCSPC with the SiPM while it was being pulsed by a laser, coupled into a multimode fiber, with a pulse width of approximately 1ns. The laser driver was connected to a HP8082A pulse generator running at 1 MHz, which also provided the START reference. This measurement was performed at a light level of $N_{pp} = 1.0$, where N_{pp} is the mean photon number per pulse. The result of this is shown in Figure 61, where only a single comparator at the single photon threshold is used for the measurement. The measurement was then repeated with all four comparators configured for multi photon detection using the values found in section 3.3.6 to perform a TCPC measurement, the result of which is shown in Figure 62. The 2-bit ADC was used in Figure 62 which led to the increase in the number of counts. This confirmed that the hardware correlator and the 2-bit ADC were working with a real SiPM by adding to the histogram depending on the number of photons detected while preserving the timing information. The multiple peaks in Figure 61 and Figure 62 are not related to the ringing effect noted in Chapter 3. They are caused due to impedance mismatching when using the HP8082A pulse generator as the driving electronics for the light source.
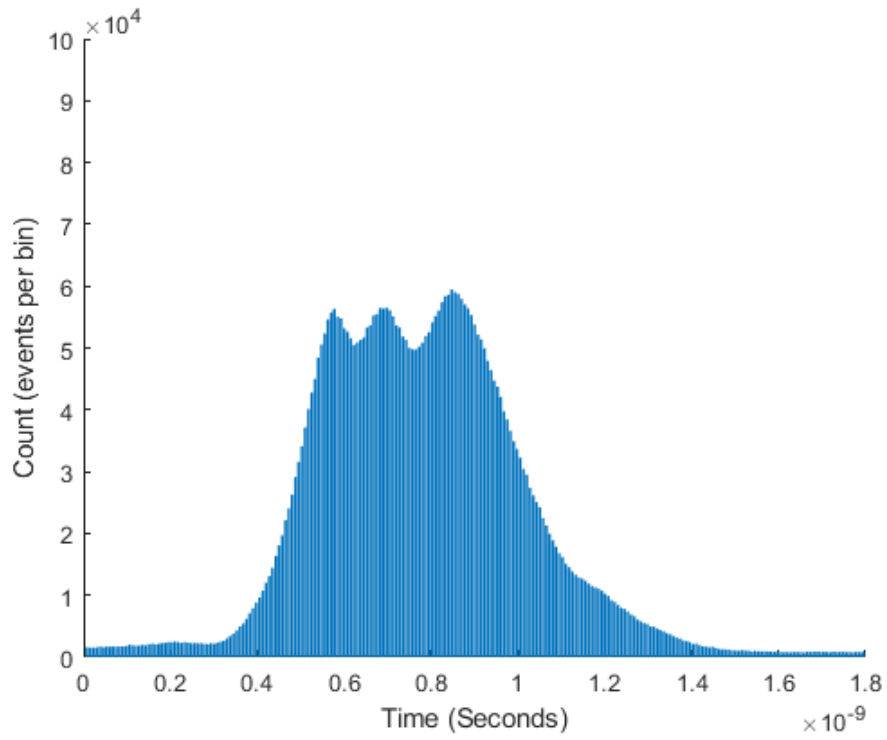
Figure 61: TCSPC measurement performed on instrument using SiPM pulsed at Npp = 1.0
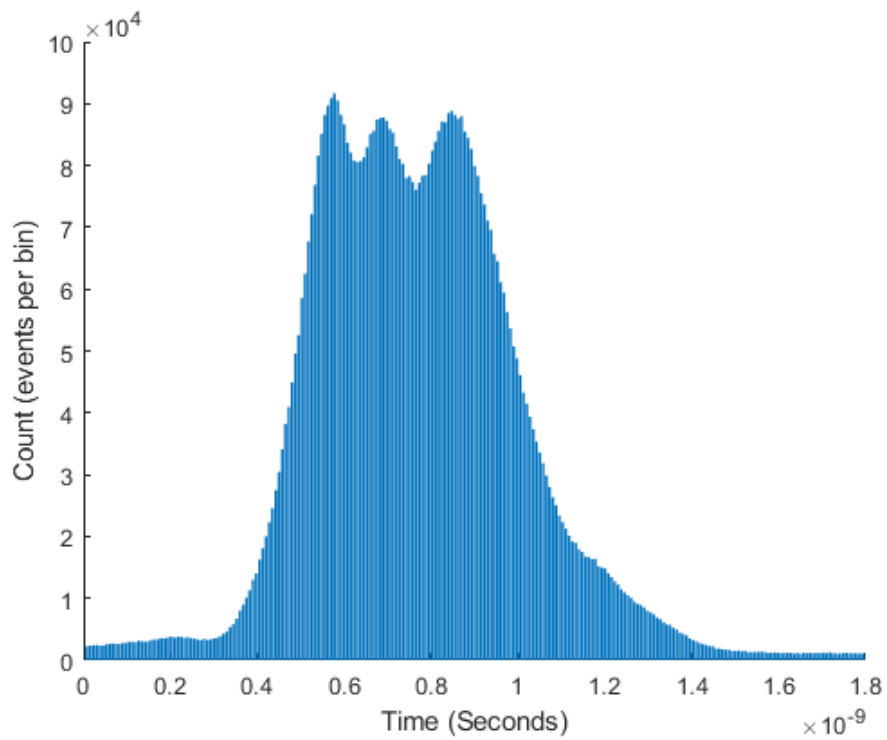
Figure 62: TCPC measurement performed on instrument using SiPM pulsed at Npp = 1.0

72

Further data obtained from the SiPM is shown in Figure 63 and Figure 64 performed at a much slower repetition rate of 105 kHz with an iC-Haus iC-HS05 laser diode driver with a bin width of 30ps. Figure 63 is performed as TCSPC while Figure 64 shows the measurement when performed with TCPC with the 2-bit digitizer working. The multiple peaks are no longer visible in these set of results as they are in Figure 61 and Figure 62. This is due to the impedance matching of the laser diode driver with the laser diode as well as the low repetition rate which is used. The measurements were performed at a bias volage of 34.2V and a light level of $N_{pp} = 2.3$. The ringing effect seen in the oscilloscope data from chapter 3 is also not present in these results that were performed on the hardware correlator developed.
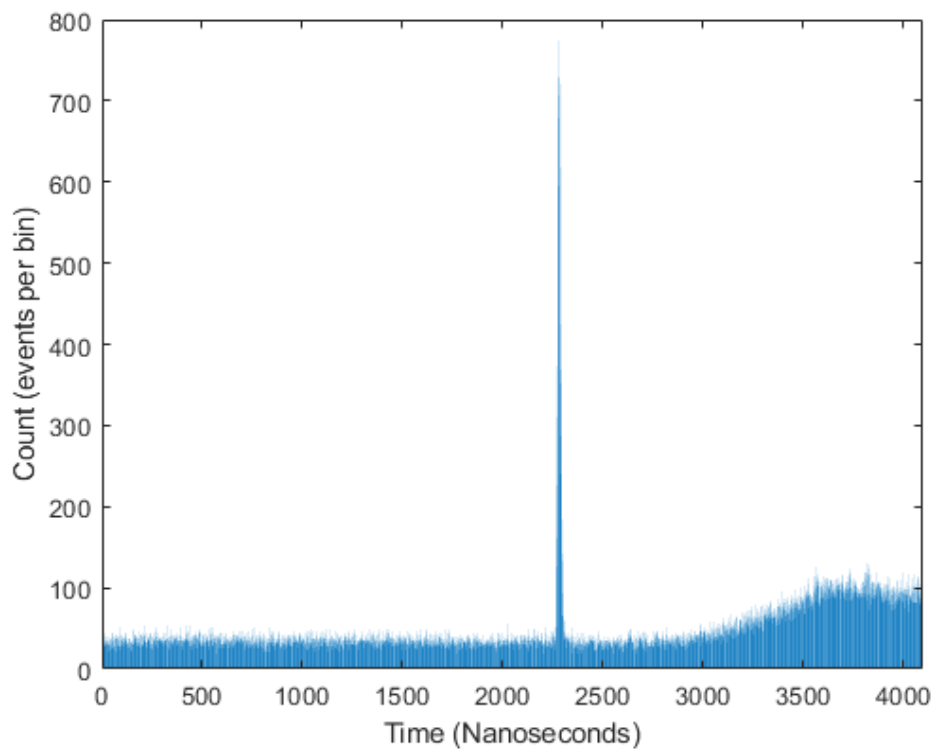
Figure 63: TCSPC measurement performed on instrument using SiPM pulsed at Npp = 2.3

M. Sadik, PhD, Thesis, Aston University, 2023
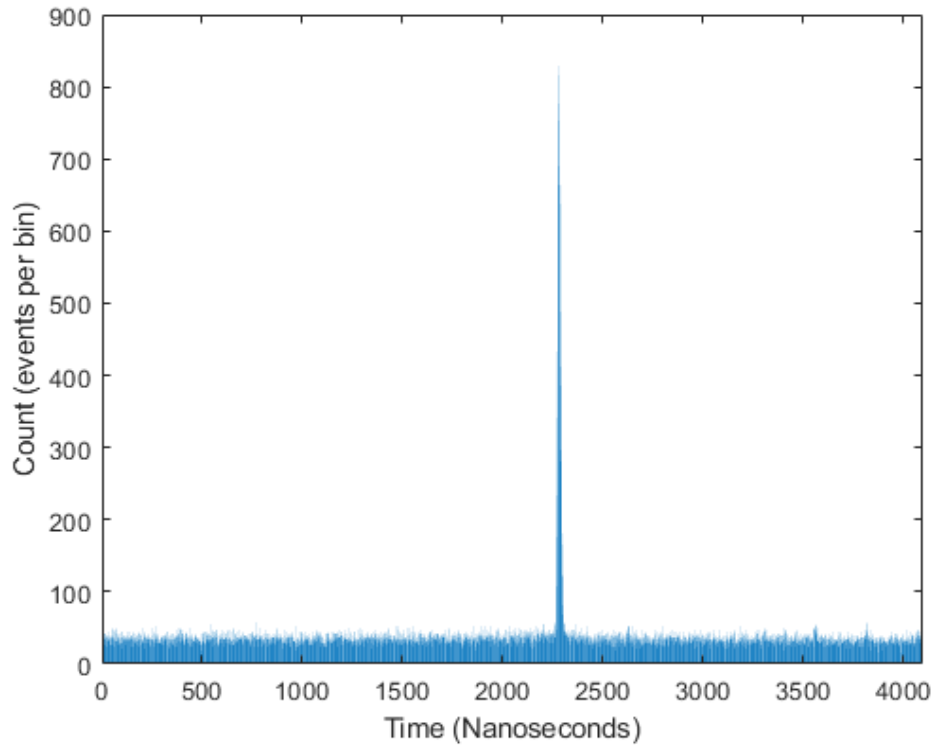
Figure 64: TCPC measurement performed on instrument using SiPM pulsed at Npp = 2.3

4.6 Conclusion

In conclusion, this chapter introduced an instrument that was developed to perform TCPC measurements in real time. The components for the system were implemented on a FPGA which included the TDCs, the correlator logic and the histogrammer module. The TDC achieved a precision of 31.8ps RMS along with a DNL of (-1, 9.18) and INL of (-2.33, 23.1). Extra circuitry was used for the amplitude quantisation of SiPM pulses to resolve the number of photons within a single excitation period with up to 4 distinct levels being quantised. The functionality of the correlator logic was confirmed by simulating a changing pulse amplitude using two pulse generators. Finally, an experimental comparison between TCSPC and TCPC was performed using a SiPM showing a clear benefit in the number of counts in the histogram.

While the 2-bit ADC hardware behaved as intended, the hardware correlator had some performance limitations which is why it was not used in the following Chapter 5 for further measurements of TCSPC and TCPC. The hardware correlator performed as expected at lower laser repetition rates, however, at higher rates the correlator state machine would have issues keeping up with the number of detections made. The rate at which the hardware would start to fall behind was experimentally tested to be approximately 2.5 MHz and higher.

M. Sadik, PhD, Thesis, Aston University, 2023

5.0 Light detection and ranging with silicon photomultipliers

5.1 Introduction

In this chapter, the benefit of using a SiPM with TCPC is evaluated along with an experimental comparison to an iD100 SPAD using TCSPC. The detectors are measured in a range of tests including the measurement of count rates to determine their ranges of usable excitation frequencies, and correlations are performed at various light levels to determine the detectors response with varying incident light. These experiments essentially measure the usable count rates and the improvement in the process of TCPC over TCSPC. A comparison is presented at the end of this section highlighting the key differences discovered from the data gathered between the TCPC and TCSPC techniques when using the different detectors.

5.2 Detector linearity and usable count rate measurements for varying mean photon number
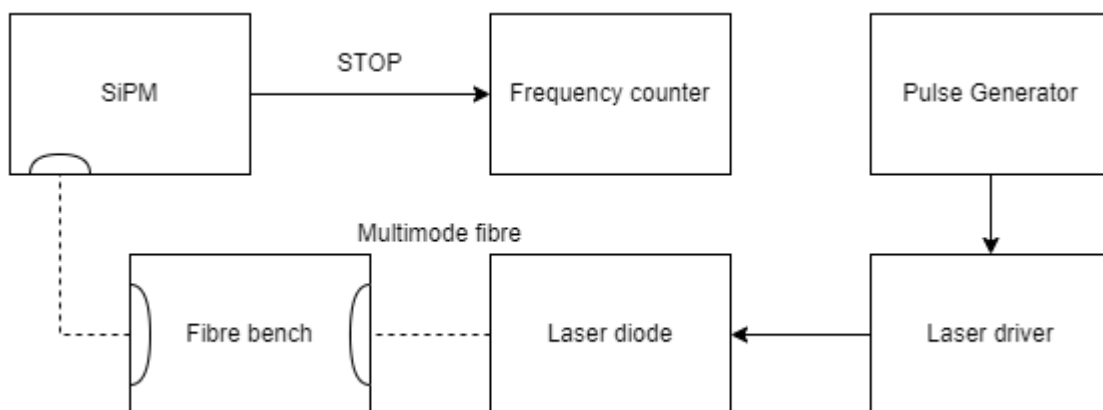
Figure 65: Block diagram of experimental setup for measuring detector linearity and usable count rates

The detectors were tested to measure the range of laser excitation rates that could be used before the detector's output started to go nonlinear. For this set of measurements, the PDEs of the detectors as well as their coupling efficiencies were ignored. Instead, the count rate of the detector was monitored while the mean number of photons in the laser pulses was tuned using ND filtering until the detector rate reflected the photon probability expected. The experimental setup for this process is depicted in Figure 65. For example, at a mean photon rate of $N_{pp} = 0.1$

the probability of a photon being detected within any excitation period should be 10% such that using a laser excitation rate of 10 MHz with the SPAD, a count rate of 1 MHz is expected from the detector. For the SiPM, the (count rate – dark count rate) was used as the dark count rate is high enough to affect these measurements. The dark count rate was not excluded from the SPAD measurement as it was low enough not to affect the result. Once the optical attenuation was tuned to achieve the desired mean photon number, the pulse rate was adjusted while measuring the count rates to determine the range of usable pulse rates for each of the detectors, or the detector's count rate dynamic range. Note the iD100 is rated to be stable up to a count rate of 20 MHz by the manufacturer [60].
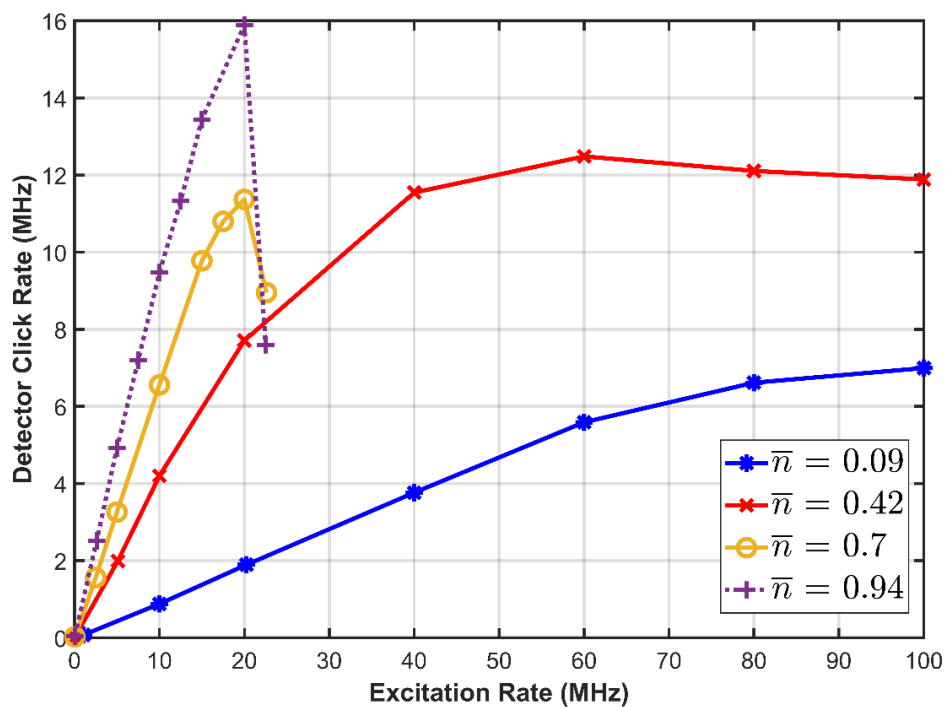
Figure 66: Measurement of count rates for iD100 SPAD performed at various light levels

The results of the count rate measurements at varying pulse rates were performed on each detector at different photon probability rates and are shown in Figure 66 for the iD100 and Figure 67 for the SiPM. The count rates were measured using an FPGA based frequency counter with 20 seconds worth of data being taken for each point. The iD100 manages to stay linear until a pulse rate of up to 20 MHz, except at the lowest photon probability of 10% where it provides a linear increase in click rates for excitation rates up to 60 MHz. The 20 MHz figure is to be expected from the datasheet [60] and is evident at the higher light levels as the dead time of the single pixel detector is rated to be between 45-50 ns (a rate of 20 - 22.2 MHz).

M. Sadik, PhD, Thesis, Aston University, 2023

As the SiPM is an array-based detector composed of multiple pixels (620 in the MicroRB-10035), the dead time for the individual microcells cannot provide us with an estimate for usable count rates like in the case of the single pixel SPAD, as each subsequent photon is likely to land on a different microcell. This and the added crosstalk probability the SiPM has due to it's the microcell array structure makes estimating the usable count rates more difficult. The SiPM's count rate was measured at the single photon threshold for various mean photon numbers and it was observed that at a photon rate of 0.1 the detector rate increased in a linear fashion until the laser excitation rate was increased to over 50 MHz. At the highest measured photon rate of 4.14 the SiPM only managed a laser pulse rate up to 7.5 MHz before the click rates started to go non-linear. This reduction in the maximum count rate is expected, as there are more microcells firing in each excitation period. The SiPM can be used at count rates up to 40 MHz at $N_{pp} = 1.0$ with a detector click rate of 35 MHz. The observed SiPM click rates are higher than the SPADs at the various photon rates for the same excitation rates. As such it is concluded that the SiPM with a single threshold can provide an advantage over the SPAD in applications only concerned with the returned count values from the detector.
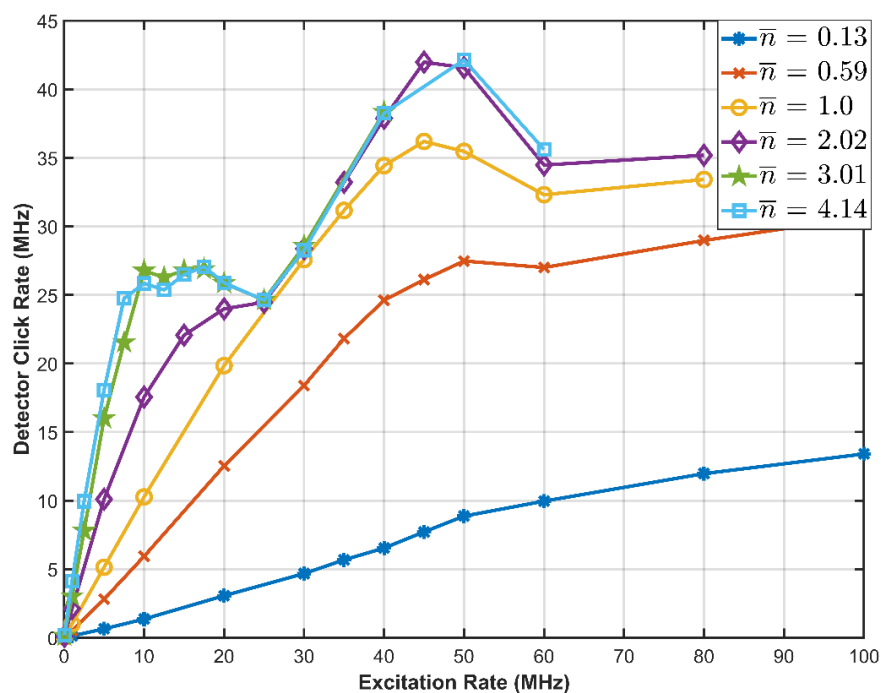
Figure 67: Measurement of count rates for SiPM at a bias voltage of 33.4V performed at various light levels using only single photon threshold

Using the threshold values for the various photon events of the SiPM mentioned in section 3.3.5, the count rates of the multi photon events were also recorded then decoded. When the TCPC

M. Sadik, PhD, Thesis, Aston University, 2023

measurements were performed with the SiPM, the signal amplitude was compared against the threshold values to infer the multi photon events. However, when using a frequency counter to measure the count rates using the various threshold values the count rate of the single photon events will also contain the two photon, three photon, and four photon events as shown in equation 5.1. The same is true for the count rate of two photon events which contains the count rate of three photon and four photon events, and the count rate of three photon events which also contains the four photon events.

$$unfiltered\ rate(N_1) = rate(N_1) + rate(N_2) + rate(N_3) + rate(N_4) \tag{5.1}$$

$$unfiltered\ rate(N_2) = rate(N_2) + rate(N_3) + rate(N_4) \tag{5.2}$$

$$unfiltered\ rate(N_3) = rate(N_3) + rate(N_4) \tag{5.3}$$

Therefore, to use this data, the count rate of 4 photon events was subtracted from the three photon event rate to get the decoded rate of three photon events. Afterwards, this decoding process was repeated for the two photon events and single photon events. Once all the event rates had been extracted, the total decoded count rate was obtained as of:

$$Decoded\ count\ rate = rate(N_1) + \left(2 \cdot rate(N_2)\right) + \left(3 \cdot rate(N_3)\right) + \left(4 \cdot rate(N_4)\right) \tag{5.4}$$
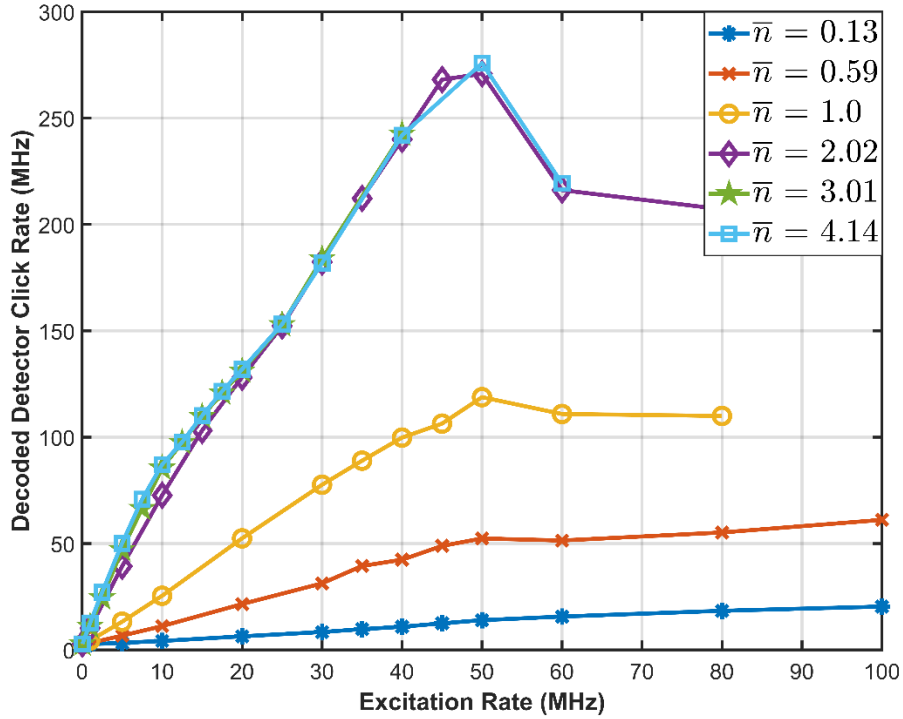
Figure 68: Measurement of count rates for SiPM at a bias voltage of 33.4V performed at various light levels using decoded multi photon events

The decoded count rates for the SiPM are shown in Figure 68 where the linearity of the multi photon events can be seen to resemble that of the singles measurement at the lower light levels up to $N_{pp} = 1.0$. While not immediately visible from the graph, the count rates at the higher levels also follow the linearity of their singles counterparts, with all of them going non-linear at the same excitation rates as their single threshold counterparts, around 7.5 to 10 MHz.

5.3 An experimental comparison of time correlated photon counting and time correlated single photon counting light detection and ranging

5.3.1 Single photon avalanche diode correlations for varying mean photon number

TCSPC measurements were performed on the iD100 detector for a range of varying mean photon numbers from $N_{pp} = 0.1$ to $N_{pp} = 19.7$ (measured at the fibre) as shown in Figure 70 to Figure 82. Figure 72 and Figure 73 show the TCSPC measurement in logarithmic scale for $N_{pp} = 0.1$ and $N_{pp} = 0.2$ respectively, and they demonstrate that the dark counts in the histogram are evenly distributed across the bins in the histogram. The experimental setup used when measuring

M. Sadik, PhD, Thesis, Aston University, 2023

the TCSPC data from the SPAD was identical to the one used for the SiPM in chapter 3 shown in Figure 27 with more values under $N_{pp} = 1.0$ (measured at the fibre) being tested for the single pixel SPAD. The START and STOP data for the correlations are taken for a total time of 4ms from a digital oscilloscope and processed using MATLAB scripts. The number of total counts measured from the correlations with the SPAD are shown in Figure 69 highlighting a mainly linear increase in count rates for the SPAD with the slope of the graph only starting to go nonlinear towards the highest light levels which suggests that the SPAD is still not yet fully saturated since if it were, a figure similar to that seen in the simulation in Figure 17 of chapter 3 would be expected.
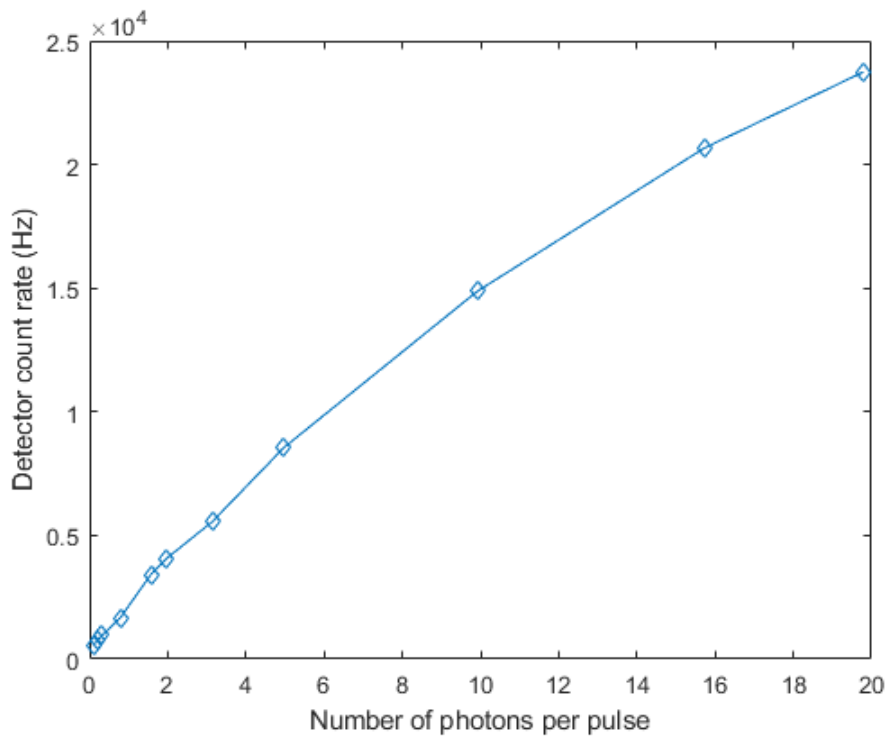
Figure 69: Measurement of iD100 SPAD count rates (per 4ms period) for varying Npp values

M. Sadik, PhD, Thesis, Aston University, 2023
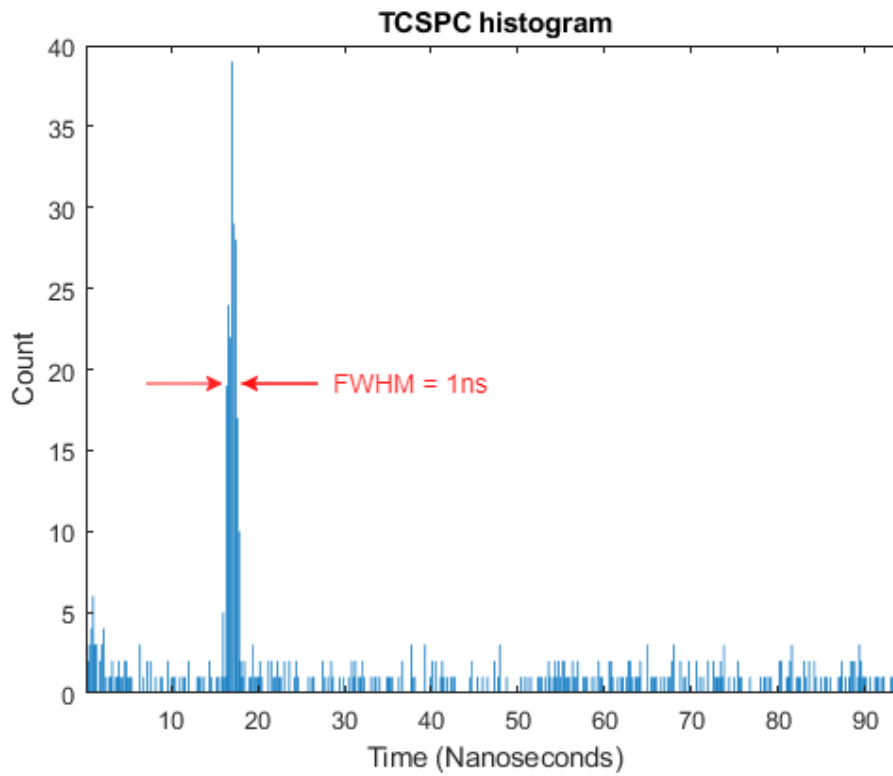
Figure 70: TCSPC Measurement performed with iD100 SPAD at Npp = 0.1 where the FWHM is approximately 1ns
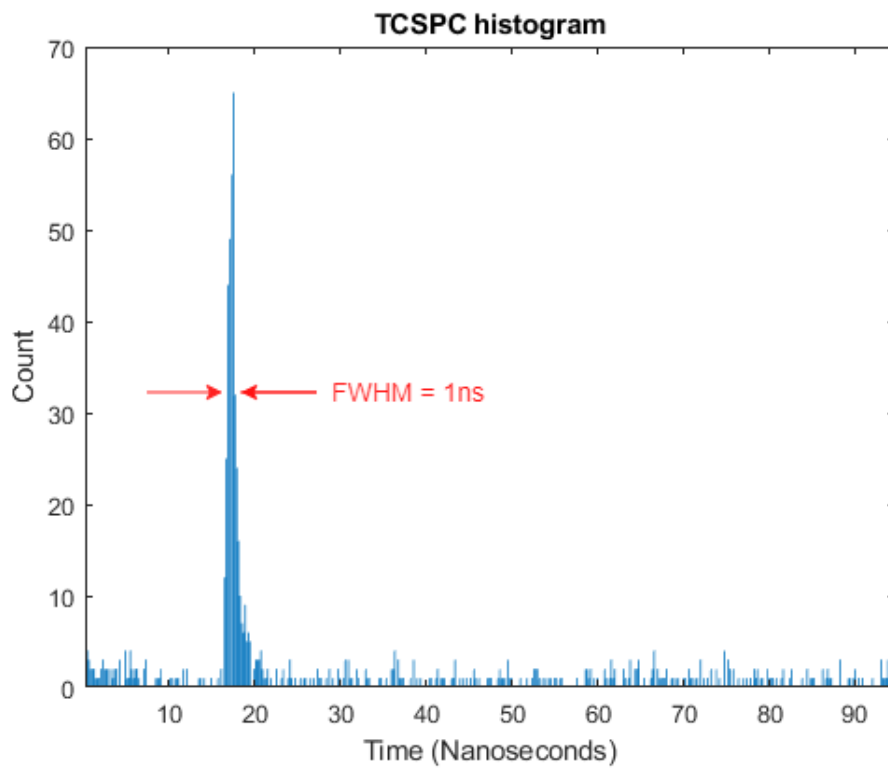
Figure 71: TCSPC Measurement performed with iD100 SPAD at Npp = 0.2 where the FWHM is approximately 1ns
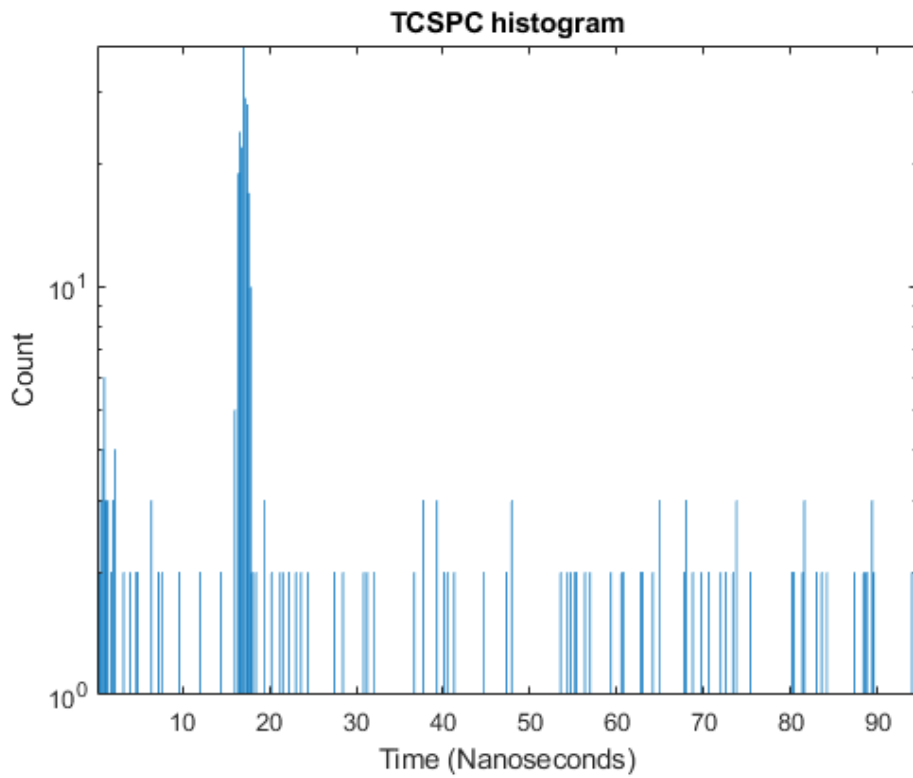
Figure 72: TCSPC Measurement performed with iD100 SPAD at Npp = 0.1 shown with logarithmic Y axis
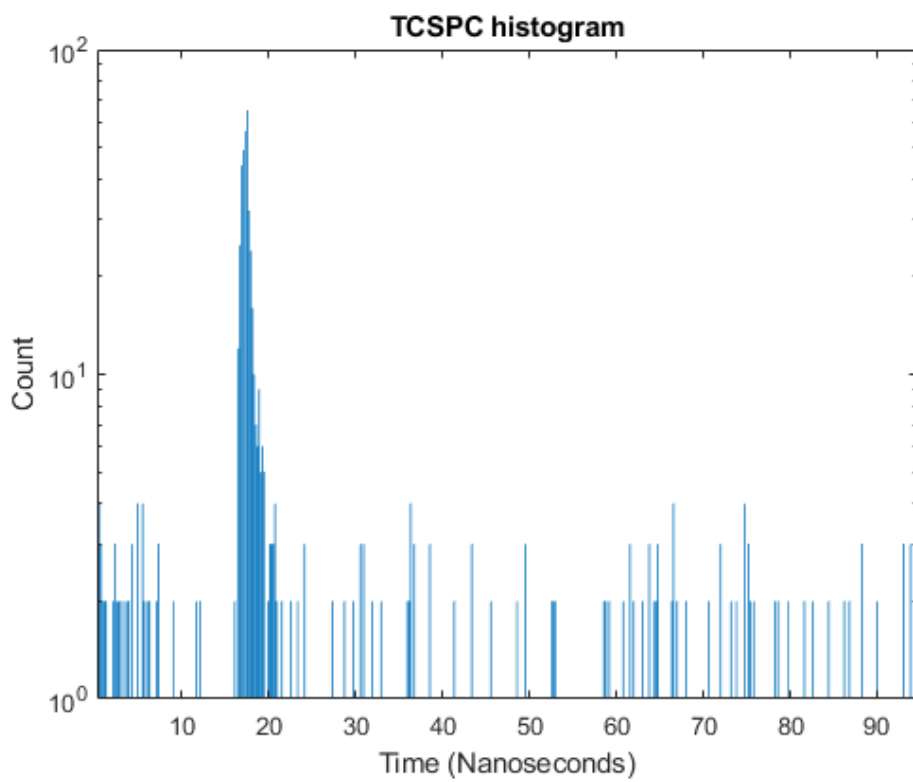
Figure 73: TCSPC Measurement performed with iD100 SPAD at Npp = 0.2 shown with logarithmic Y axis
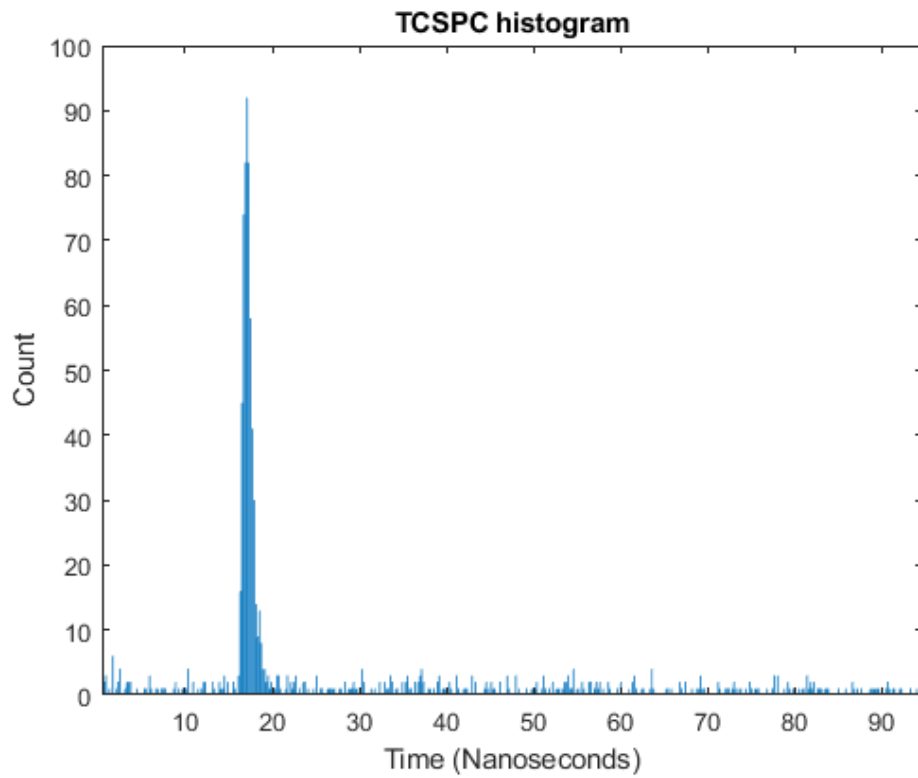
Figure 74: TCSPC Measurement performed with iD100 SPAD at Npp = 0.31
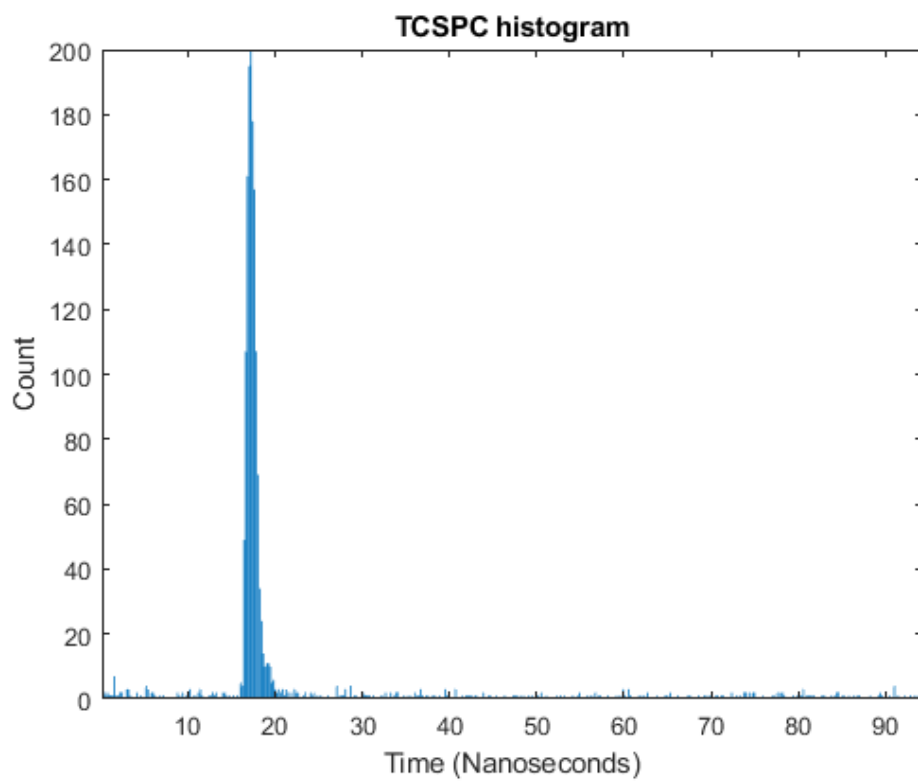
Figure 75: TCSPC Measurement performed with iD100 SPAD at Npp = 0.78

M. Sadik, PhD, Thesis, Aston University, 2023
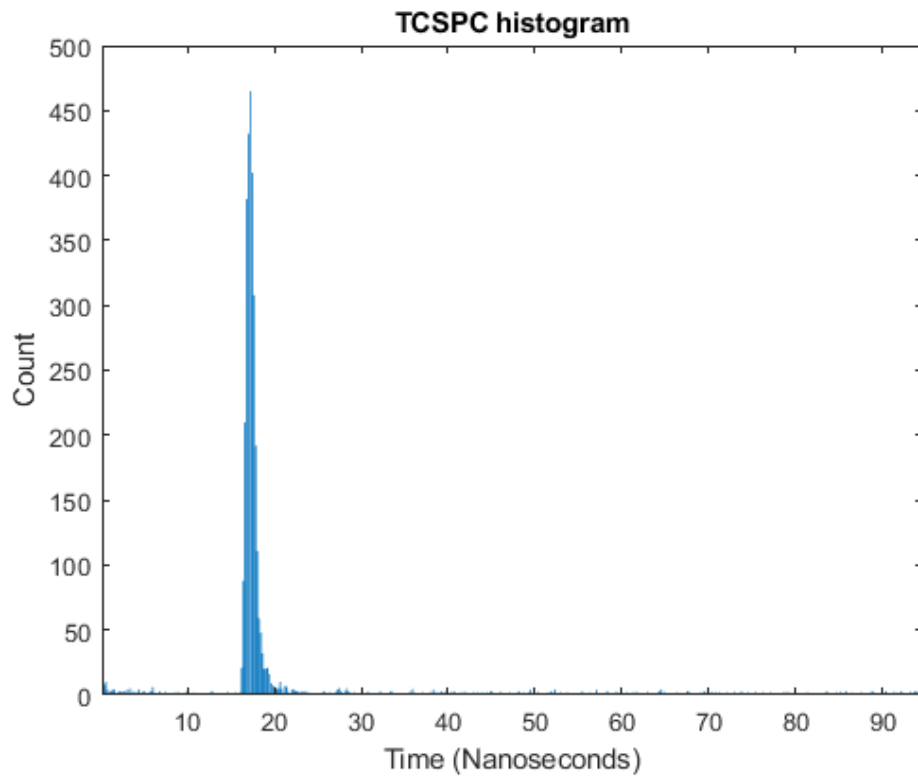
Figure 76: TCSPC Measurement performed with iD100 SPAD at Npp = 1.57
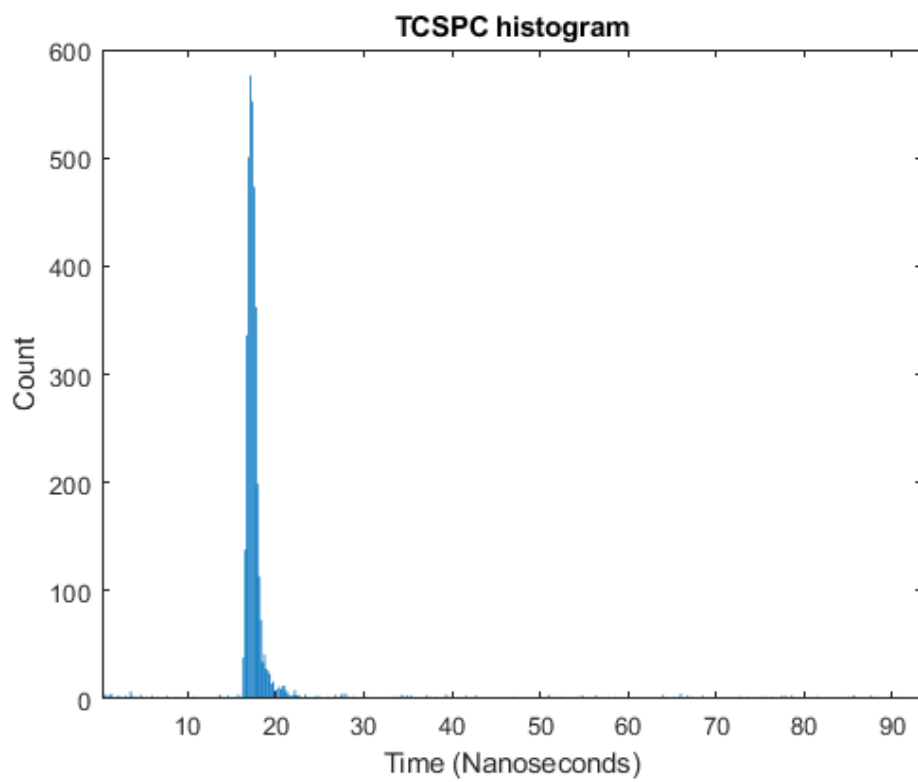
Figure 77: TCSPC Measurement performed with iD100 SPAD at Npp = 1.97
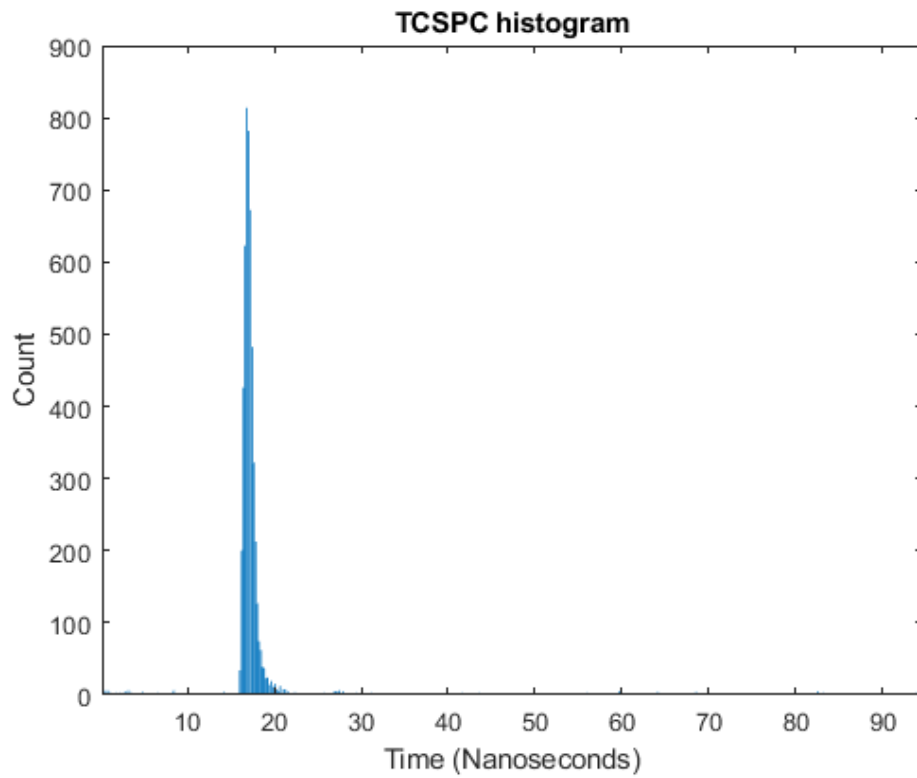
Figure 78: TCSPC Measurement performed with iD100 SPAD at Npp = 3.13
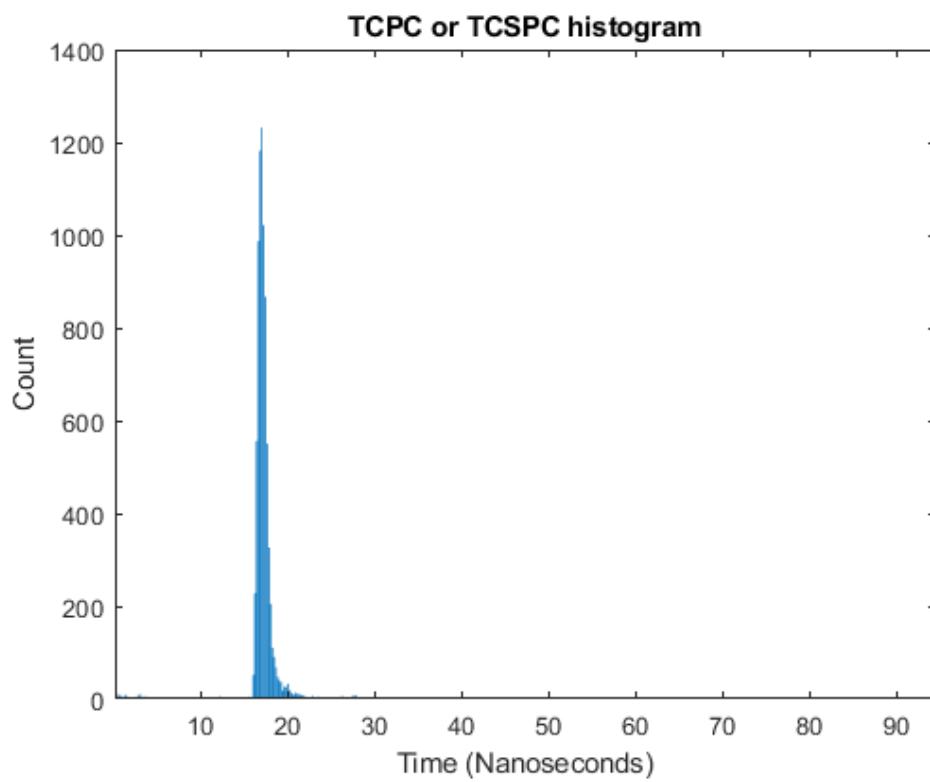
Figure 79: TCSPC Measurement performed with iD100 SPAD at Npp = 4.97

M. Sadik, PhD, Thesis, Aston University, 2023
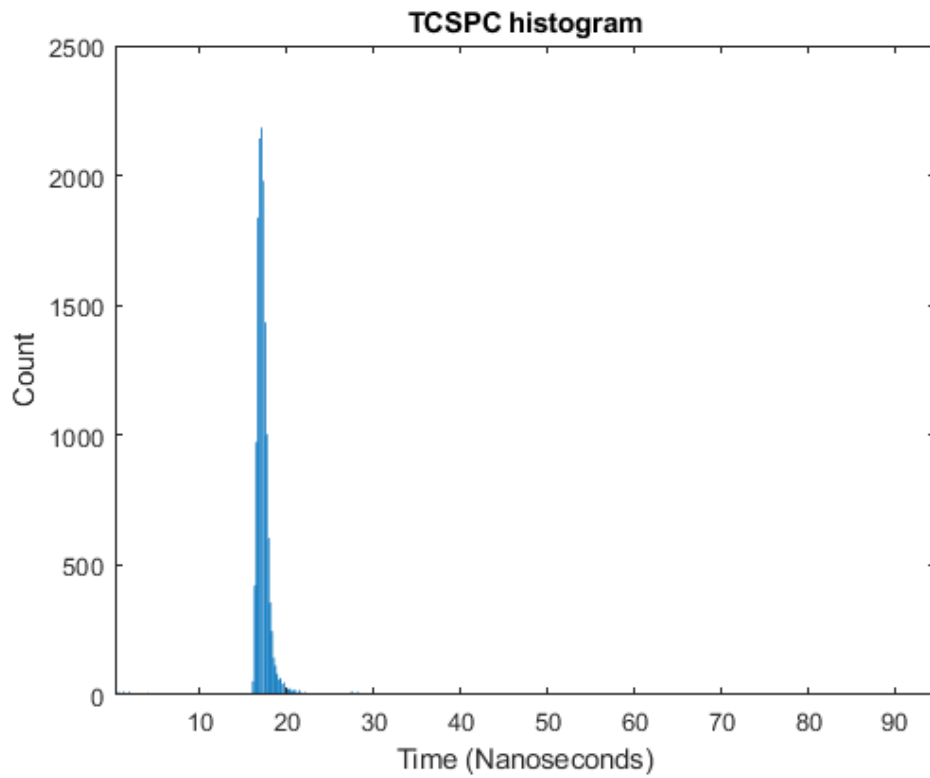
Figure 80: TCSPC Measurement performed with iD100 SPAD at Npp = 9.9
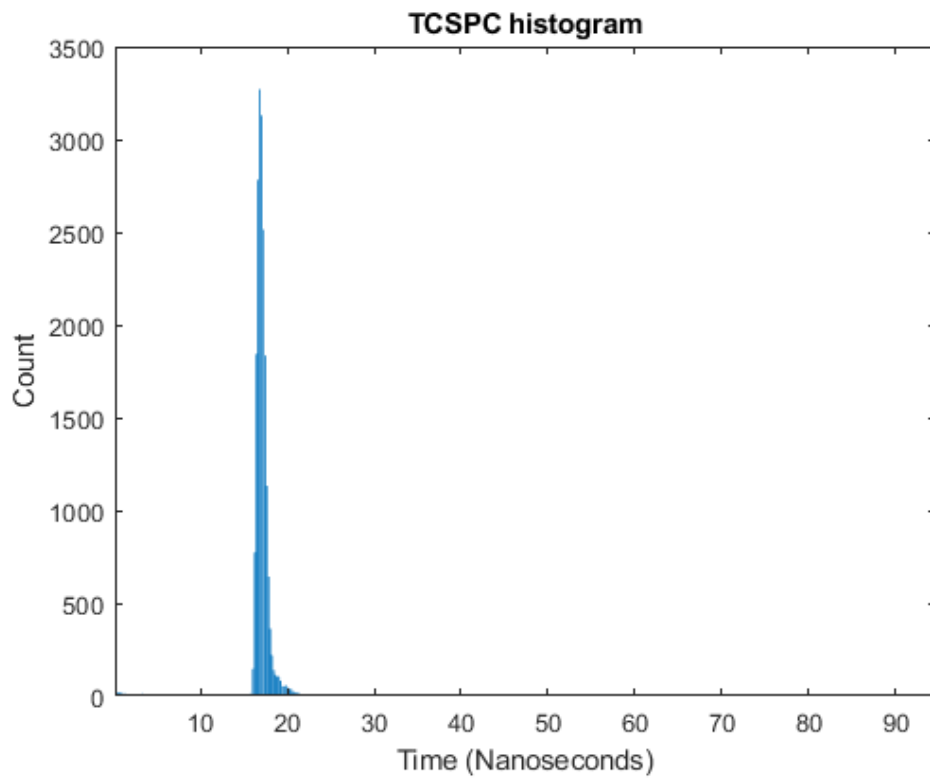
Figure 81: TCSPC Measurement performed with iD100 SPAD at Npp = 15.7

M. Sadik, PhD, Thesis, Aston University, 2023
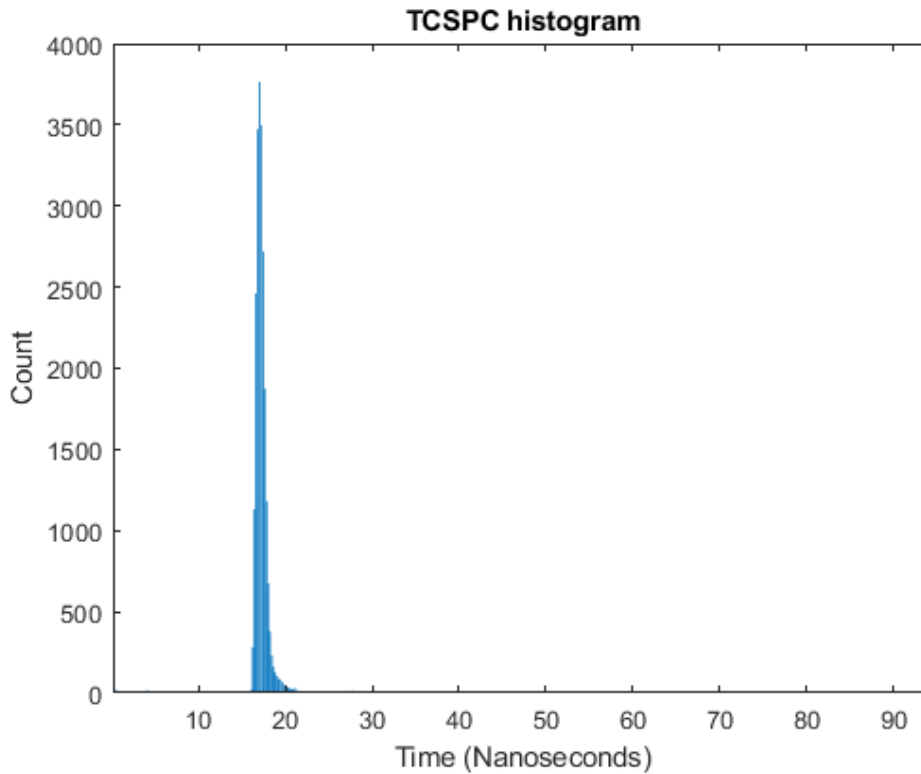
Figure 82: TCSPC Measurement performed with iD100 SPAD at Npp = 19.7

5.3.2 Silicon photomultiplier range correlations for varying mean photon number

The previously measured amplitude values for the various photon event levels were used with the MATLAB script for photon counting to perform TCPC. For every successful correlation, the peak amplitude of the correlated SiPM signal was compared against the measured photon number amplitudes and the number of photons corresponding to the signal amplitude was added to the bin at the measured time. These measurements were repeated with the data for both bias voltages (33.4V and 34.9V) previously acquired in section 3.3.5. Figure 83 and Figure 84 show the number of counts in the TCPC histograms for each of the bias voltages compared with those of TCSPC. The count rates were observed to have an increase of up to 236% over the count rates in the TCSPC results with the SiPM previously acquired for a bias of 33.4V and an increase of 202% in the count rates at a bias of 34.9V. The measured TCPC waveforms for both bias voltages are shown in Figure 85 to Figure 92. The shapes of the measured TCPC correlations match those of their TCSPC counterparts with both the correlated photons and some of the noise photons.
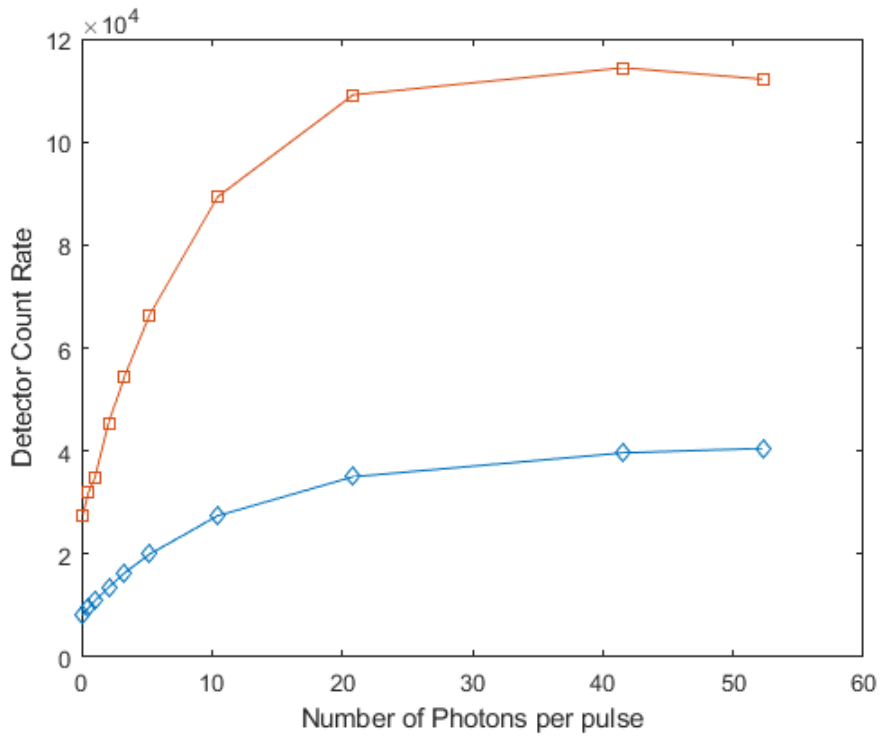
Figure 83: Comparison of SiPM Count rates using single photon events vs decoded multi photon events for varying Npp values for 4ms period, Biased at 33.4V
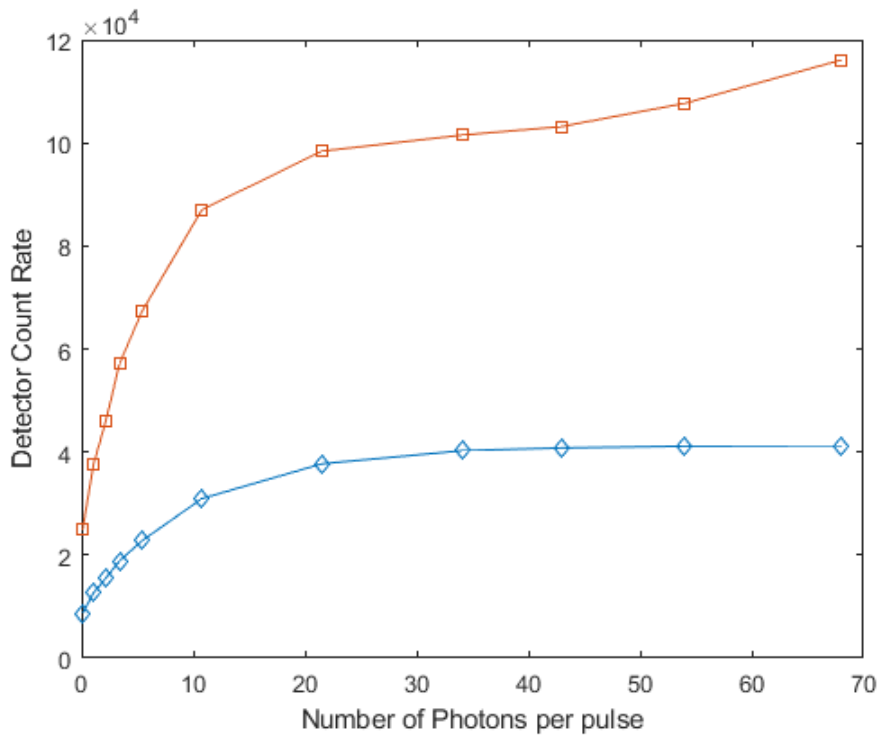
Figure 84: Comparison of SiPM Count rates using single photon events vs decoded multi photon events for varying Npp values for 4ms period, Biased at 34.9V
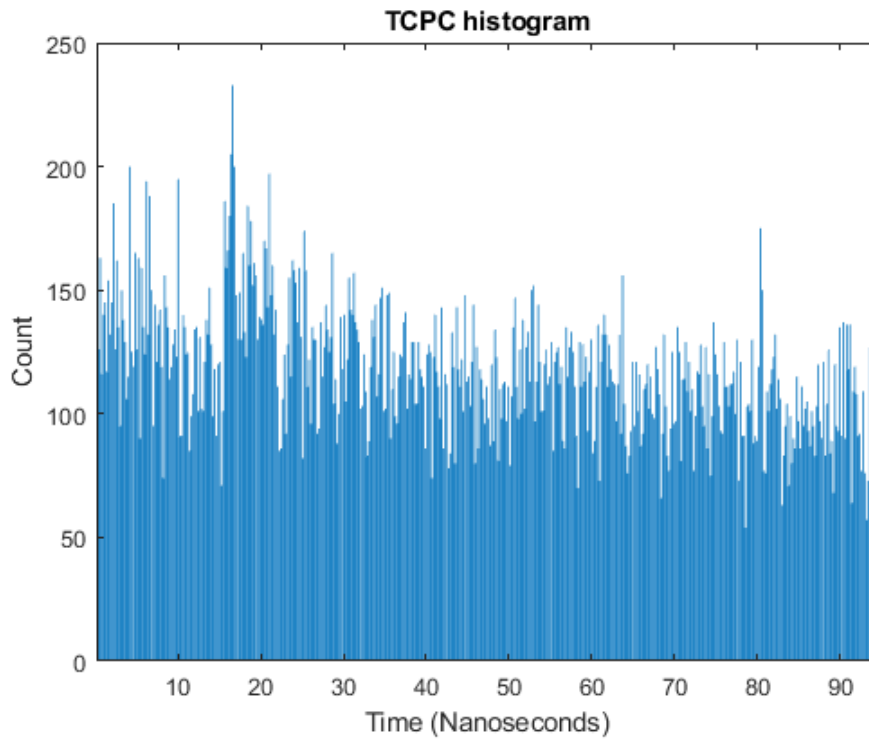
Figure 85: TCPC measurement with SiPM at Npp = 0.1, Biased at 33.4V
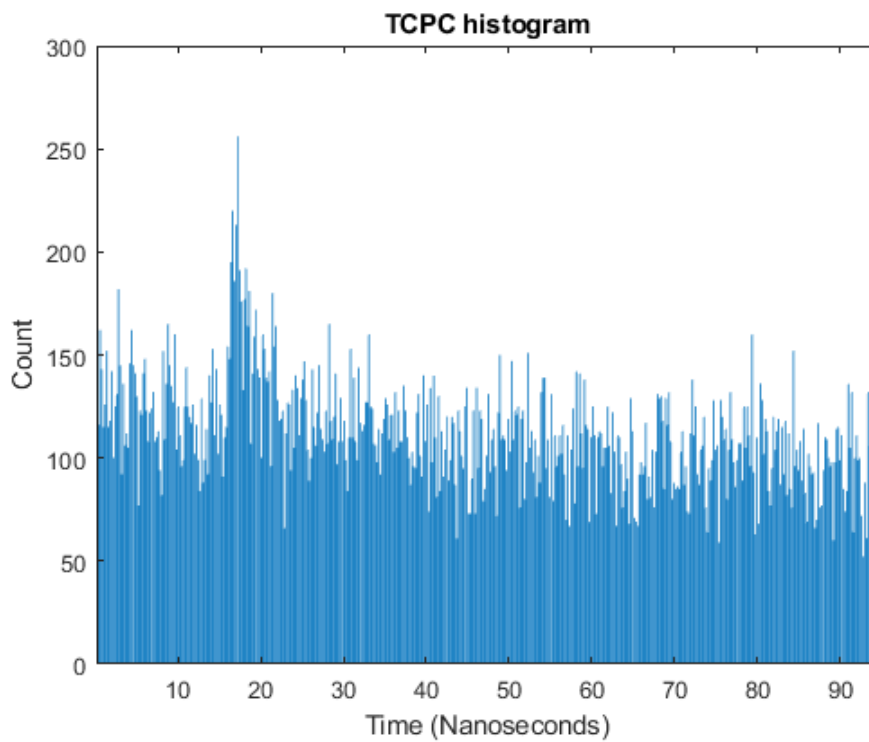
Figure 86: TCPC measurement with SiPM at Npp = 0.1, Biased at 34.9V

M. Sadik, PhD, Thesis, Aston University, 2023
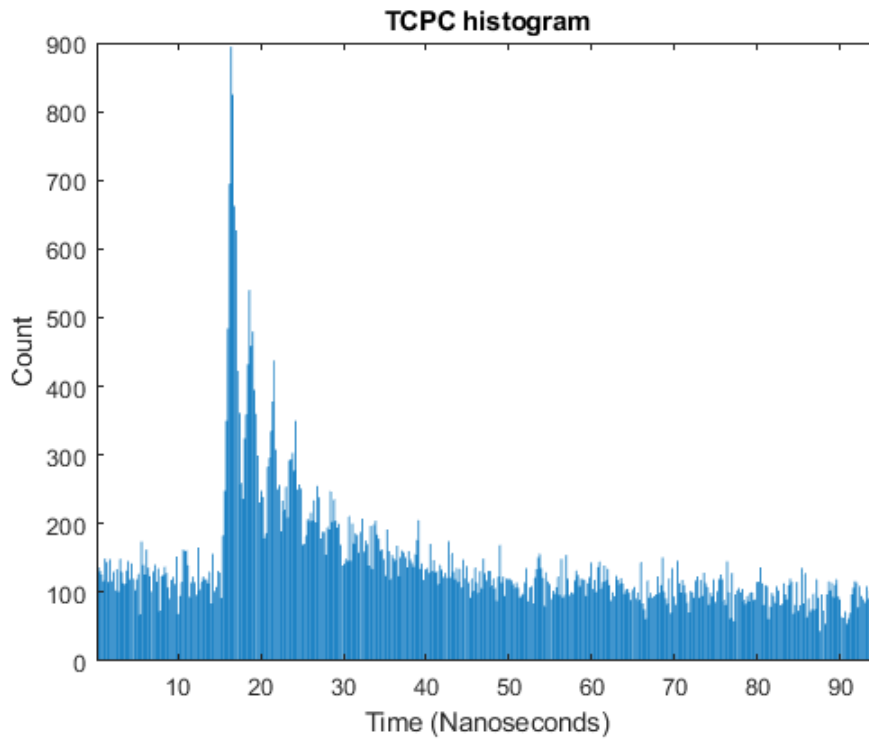
Figure 87: TCPC measurement with SiPM at Npp = 1.0, Biased at 33.4V
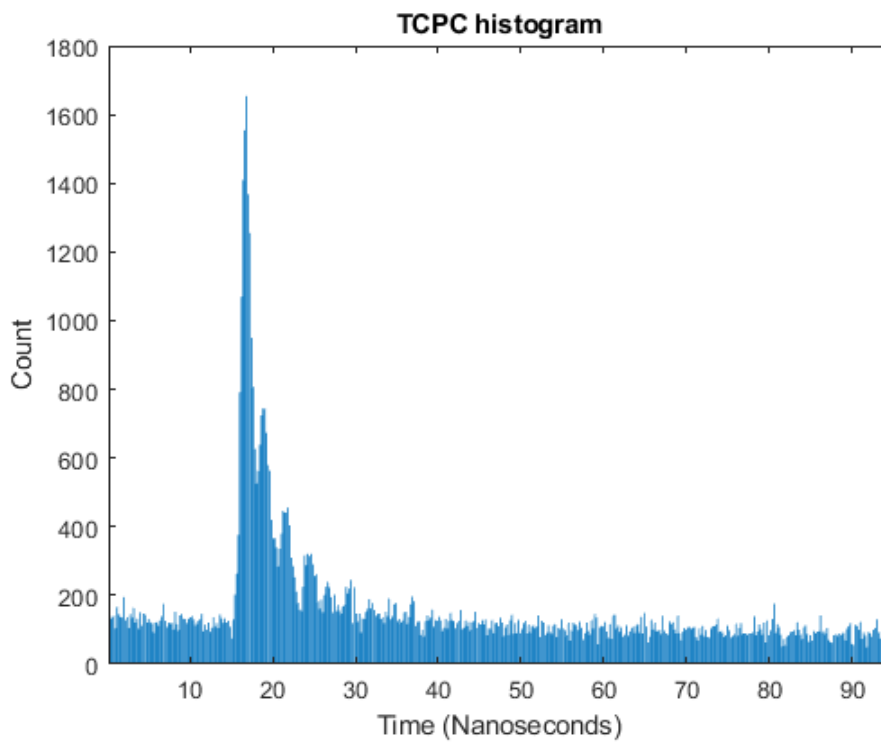
Figure 88: TCPC measurement with SiPM at Npp = 1.0, Biased at 34.9V
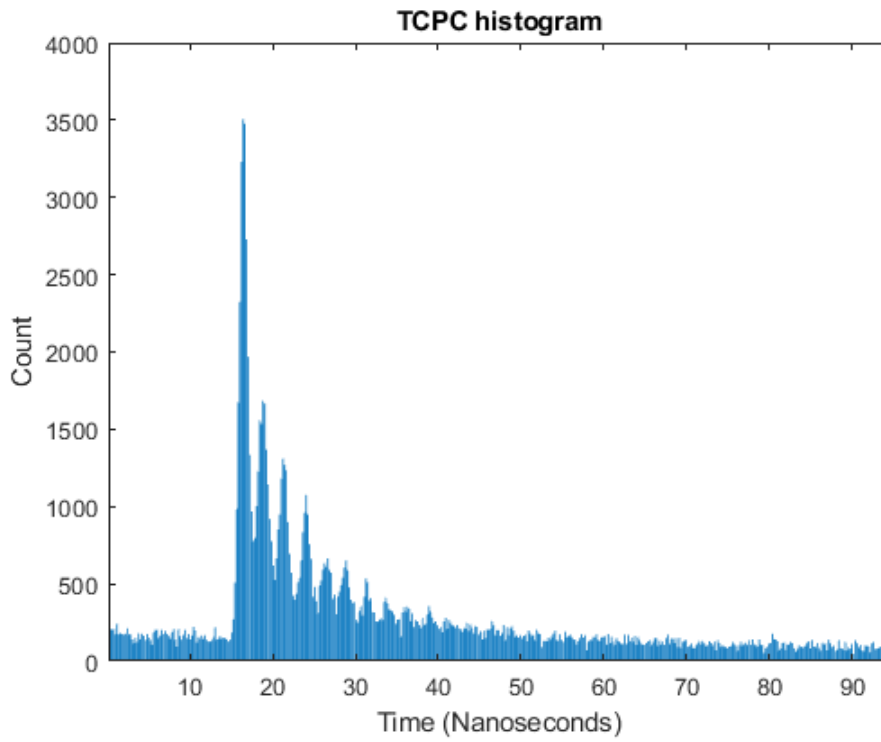
Figure 89: TCPC measurement with SiPM at Npp = 5.0, Biased at 33.4V
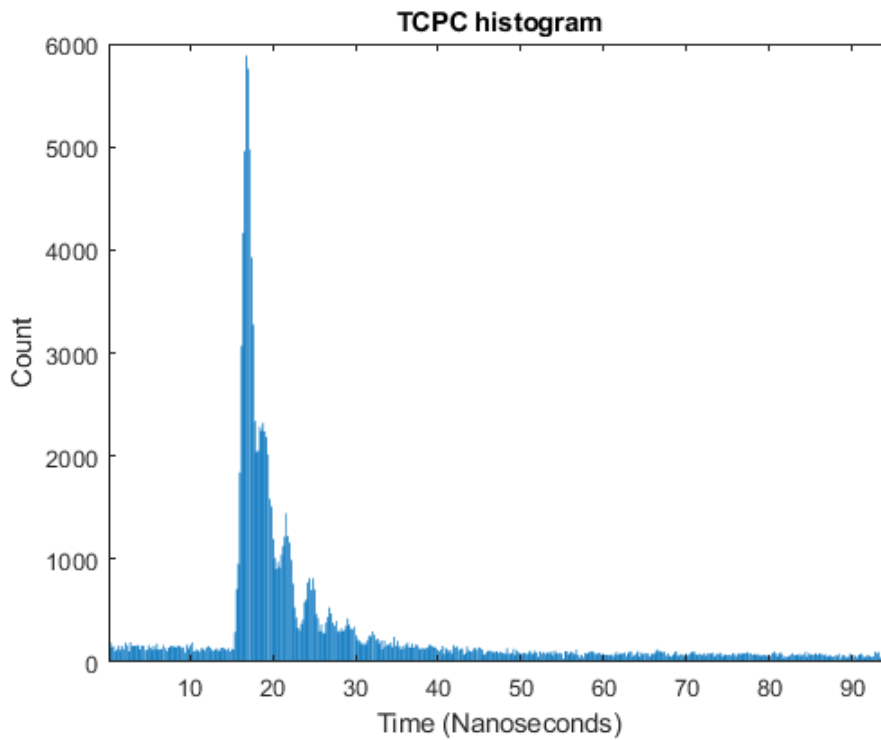
Figure 90: TCPC measurement with SiPM at Npp = 5.0, Biased at 34.9V

M. Sadik, PhD, Thesis, Aston University, 2023
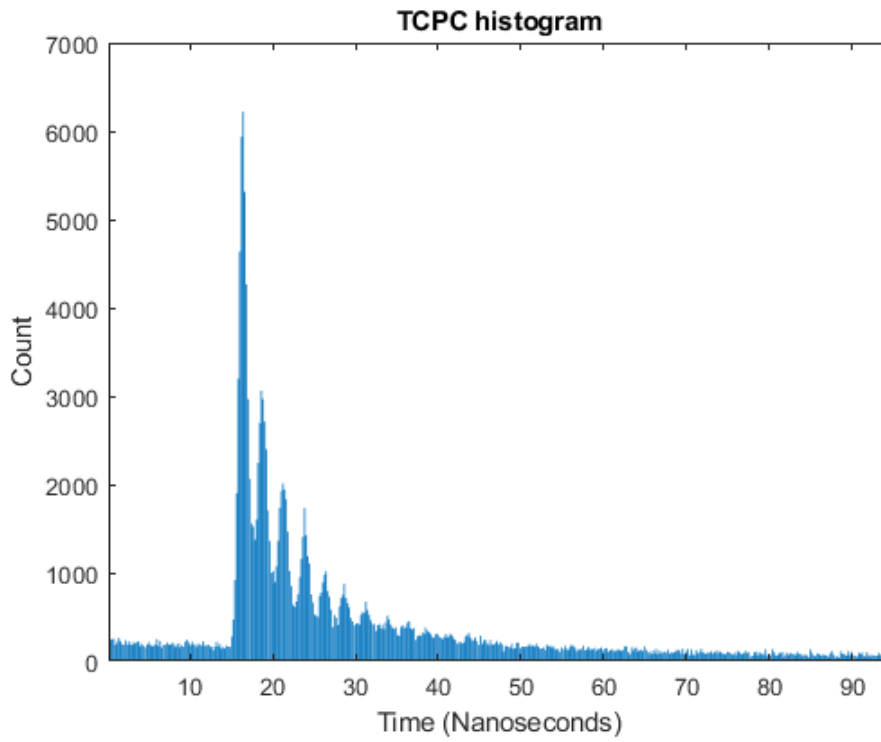
Figure 91: TCPC measurement with SiPM at Npp = 10.0, Biased at 33.4V
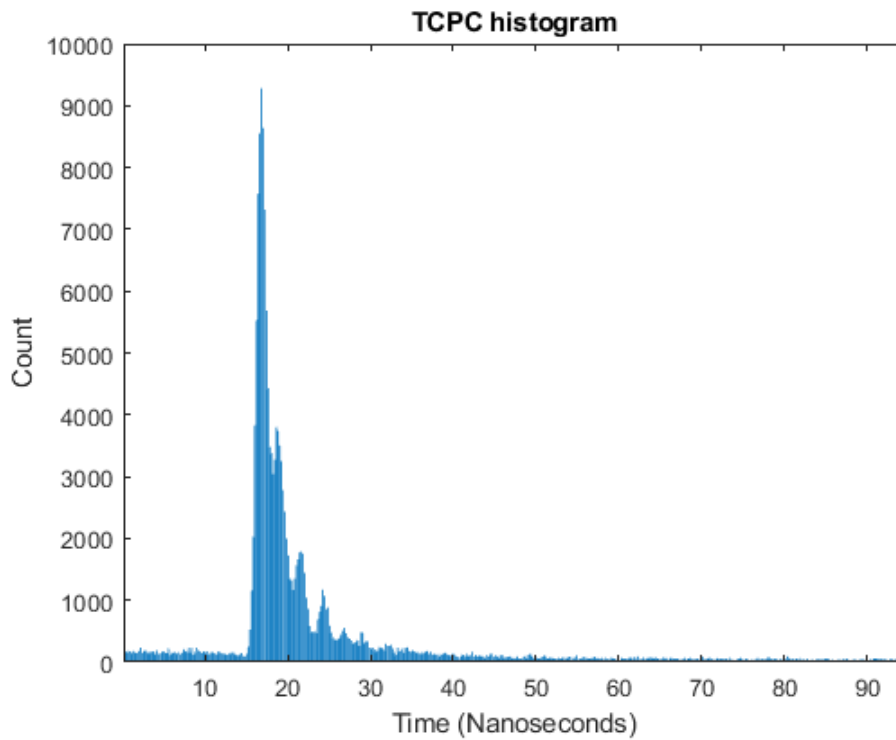
Figure 92: TCPC measurement with SiPM at Npp = 10.0, Biased at 34.9V

5.3.3 Comparison

When normalising the counts of the detectors to exclude the PDE, the SiPM saw a benefit of up to 140% in the count rates using TCPC when compared with TCSPC performed on the SPAD, along with a benefit of 40% in the count rates over the SPAD after the SiPM counts were further corrected for optical crosstalk. This comparison is shown in Figure 93 where the results have been corrected to ignore the PDE of the detectors which were measured at around 3% - 4.2% for the SPAD and 8% to 11% for the SiPM at a bias voltage of 33.4V (7V overvoltage).
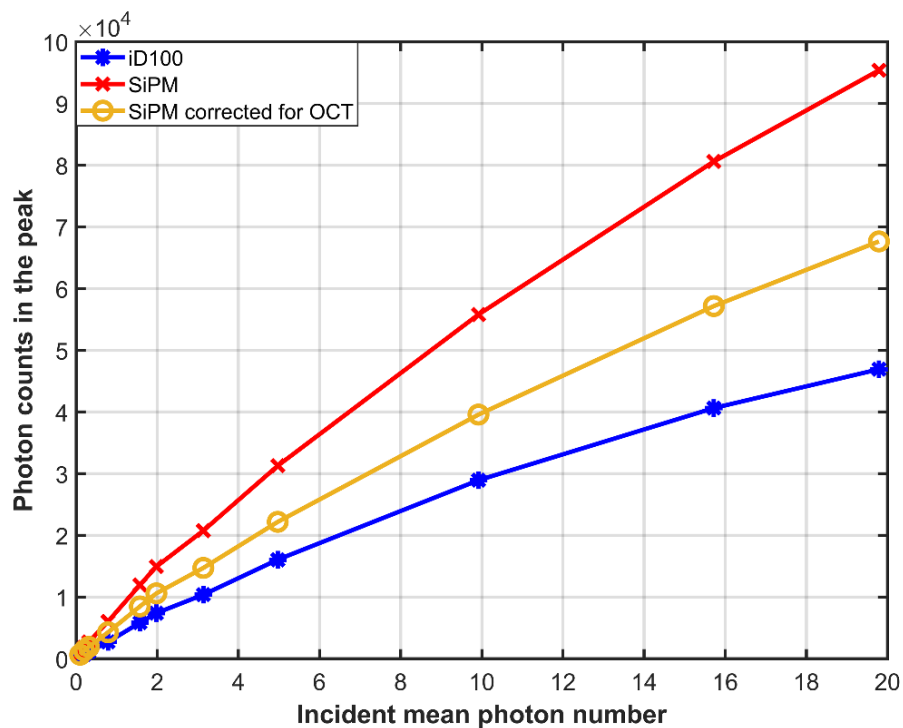
Figure 93: Measurement of Counts in the peak at varying mean photon numbers for the SiPM and iD100 SPAD with extra SiPM trace corrected for crosstalk. Values from the SiPM and SPAD shown have been corrected for PDE

Furthermore, the signal-to-noise ratios (SNR) of the two detectors were measured for various light levels with the results showing that the SPAD has a better overall SNR than the SiPM at lower light levels, which is expected due to the much lower dark count rate. The SNR of the two detectors behave very differently from each other, in the case of the SiPM the SNR is seen to improve almost linearly as the light levels are increased. However, in the case of the SPAD, logarithmic growth is observed in the SNR with the increasing light levels. This difference in SNR curves is due to the difference in the noise factors in the two detectors. The SPAD only suffers from noise in the form of dark count, whose value is not light dependent, and afterpulsing which

has a small probability of occurring (0.5% for the iD100) which is why an increase in the SNR of the detector is observed as the number of signal photons increase.
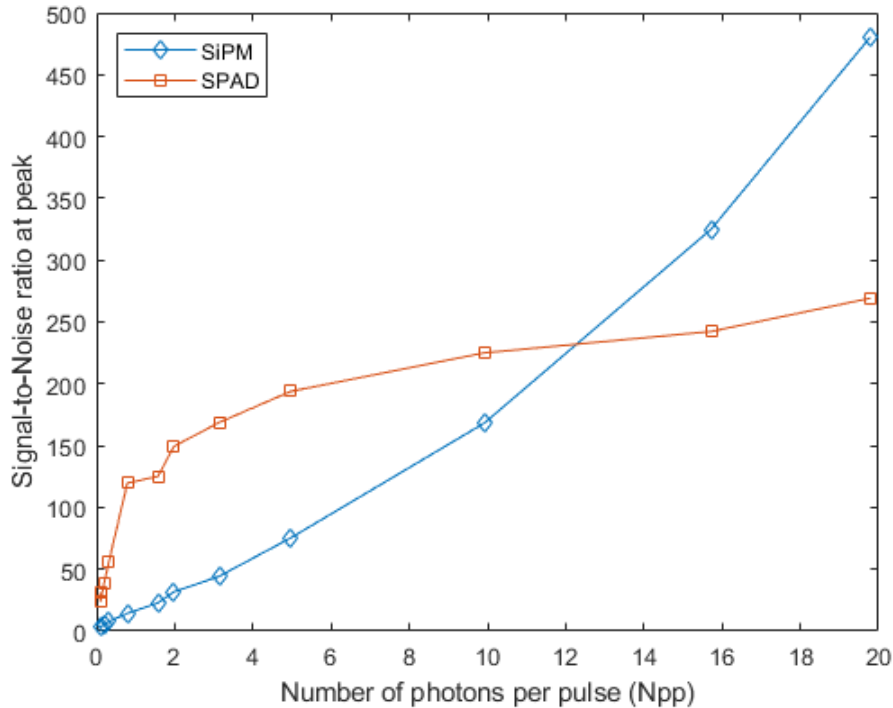
Figure 94: Signal-to-Noise ratios of the detectors measured from the peak of the histogram to the noise floor of the SiPM (biased at 33.4V) and the iD100 SPAD

While these noise factors also plague the SiPM, the detector also suffers from optical crosstalk which is a noise property that increases with incident light and is defined as a probability of a single incoming photon triggering a microcell which in turn triggers a secondary microcell. The crosstalk in the SiPM is the main noise factor in the detector and because of its increase with the amount of incident light we see a linear rise in the SNR of the SiPM. The SNR was measured for both the detectors as both a difference between the signals in the peak to the noise floor, shown in Figure 94, and as a difference between the total correlated signal photons to the total uncorrelated noise photons.
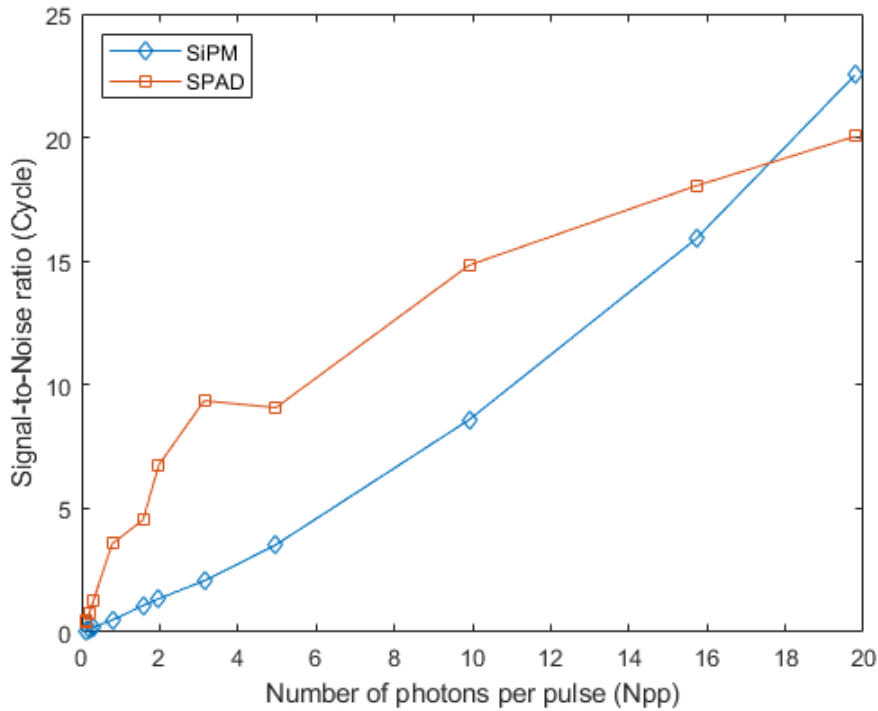
Figure 95: Signal-to-Noise ratios of the detectors measured from the counts of the valid signal to those of the noise in the histogram using the SiPM (biased at 33.4V) and the iD100 SPAD

5.4 Conclusion

In conclusion, this chapter looked at the SiPM correlations when using TCPC and compared them to TCSPC on a SPAD for varying incident mean photons per pulse. A significant benefit of 140% was observed in the count rates for TCPC with the SiPM when compared to those of TCSPC with the SPAD as well as an increase of up to 236% over the counts in TCSPC with the SiPM. Hence, confirming that there is a clear benefit in using TCPC with a photon number resolving detector in high mean photon per pulse or high light level return applications. However, at lower return light levels or mean photon number per pulse applications, TCSPC with a SPAD is advantageous due to the far better noise floor.

This is further evidenced by the signal to noise ratio analysis, where the SPAD in TCSPC mode offers a factor of 10 improvement over the SiPM for the peak to noise floor ratio. The result of this signal to noise ratio issue with the SiPM is also evident in the resultant correlations, where at low mean photon number levels, the peak in the correlation is barely visible and is of similar height to the noise floor (Figure 80, Figure 81 for the SiPM at 0.1 N_{pp}). However, the SPAD with TCSPC can clearly resolve the peak at such mean photon numbers (Figure 67). However, the

SiPM's resultant TCPC correlations at higher mean photon numbers show far improved peak to noise floor ratios (Figure 87 for example).

The SiPM operating in TCPC can outperform the SPAD regarding signal to noise ratio given high enough mean photon numbers. However, detector linearity will limit the maximum extent to which a SiPM can be operated at to ensure the correlations accurately reflect the optical time domain signal.

In regard to applications, the SiPM TCPC approach is likely to have little benefit in quantum optics experiments, quantum key distribution and similar fields due to the poor signal to noise ratio at low mean photon numbers, mostly caused by the high dark count rate of such detectors. This issue could be improved by reducing the number of microcells used in a SiPM, but this would also reduce the dynamic range of the detector in terms of photon number resolving capability and count rate.

However, TCPC could have considerable advantages in fields where high mean photon numbers are feasible. Potential applications include automotive LiDAR, medical imaging systems such as Positron Emission Tomography (PET), Fluorescence Lifetime Imaging (FLIM) and Photon Absorption Spectroscopy Systems. Photon absorption spectroscopy systems are of particular interest due to potential benefits TCPC offers to enable real-time monitoring of greenhouse gases such as Carbon Dioxide (CO_2) and Methane (CH_4). However, detection of such greenhouse gases would require different detectors to accommodate the absorption lines of such gases. However, Discrete Amplification Photon Detector (DAPD) arrays [121] offer an alternative using InGaAs, which might prove to be a line of future research.

6.0 Future work

6.1 Scalability using ASICs and greenhouse gas monitoring

The instrument developed is not limited to use with SiPMs, as any photon number resolving detector can be used with the correct thresholding values. However, there is considerable scope to utilise this technology in combination with detector arrays. This would offer considerable decrease in the required integration time in a typical imaging scenario, allowing for faster acquisition. However, when working with detector arrays, the cost of scaling up the front end circuitry used for amplitude quantisation will also rise significantly, as will the size and complexity of the associated circuit board.

For such an approach, SiPM readout ASICs might offer a possible solution, in particular the Citiroc 1A [122] which provides 32 channels of discriminators along with the included amplification required for SiPMs in a small footprint. Using such an ASIC would be a cost effective way for up to 32 photon number resolving detectors to be used with only 4 chips, with one for each photon threshold. This is required as each IC has a common fixed threshold voltage for all 32 channels. This would offer a considerable reduction in cost and circuit board complexity. A possible approach is proposed below in Figure 96 for a potential 5x5 detector array system (a common detector array size). However, 32 detectors could be utilised in a different detector array setup.

There will be a limit on the extent to which such ICs can be utilised to provide scalable interfaces to photon number resolving detectors. This is due to the signal being essentially divided by the splitter, there will be a point at which the detector's output reaches the noise floor.
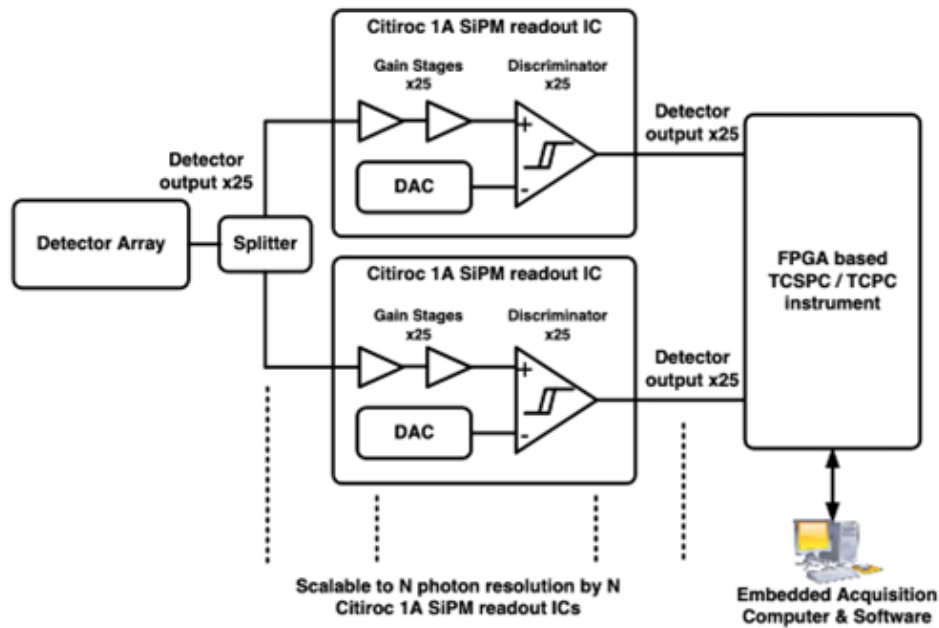
Figure 96: A proposed hardware architecture to create scalable photon number resolving systems

Such technology is also of interest with other types of photon number resolving detectors. In particular, the Discrete Amplification Photon Detector (DAPD) is a type of single photon sensitive detector possessing high gain factors and low noise. These detectors can be used in the near infrared wavelength along with a suitable laser system for gas absorption spectroscopy to measure the concentration of greenhouse gases such as Carbon Dioxide (CO_2) and Methane (CH_4).

The work presented in this thesis has formed a part of the SPLICE Innovate UK project (Single Photon Lidar Imaging of Carbon Emissions). Hence, there is a great potential for this technology to be taken further in gas imaging systems.

6.2 Mean shift mitigation for TCPC instrument

The TCPC instrument developed presents a mean shift across the various photon events as mentioned in section 4.4 due to the constant level thresholding of the comparators which result in a time offset for varying input thresholds. The observed mean shift is a thresholding effect of the hardware and is not related to the ringing seen from the oscilloscope data in Chapter 3 and Chapter 5. A method for mitigating this was introduced where the differences between the multi photon event means, and the single photon event mean is stored in a look up table with the

M. Sadik, PhD, Thesis, Aston University, 2023

differences being subtracted from the calculated time difference as shown in equation 4.1. This remains an area of interest for future implementation.

7.0 Conclusion

Chapter 2 provided a review into the concepts and techniques used throughout this work. A particular focus was given to TDCs and SiPMs as they were the main technologies explored during this work. An overview of various techniques used to implement TDCs on a FPGA was given along with methods used to calibrate TDCs and the common metrics used to identify a TDCs performance. A background into SiPMs is given detailing their structure that allows them to resolve photon numbers, the various noise factors which plague a typical SiPM, and the fast output mode which is a capacitively coupled output mode for onsemi SiPMs with faster rise time and shorter pulse widths over the standard SiPM output. A short introduction into LiDAR technologies is provided with single photon LiDAR, that typically uses TCSPC, being an area of interest for this work.

In Chapter 3, an onsemi MicroRB-10035 SiPM module is characterised for use as a single photon detector for TCSPC measurements. An enclosure for the SiPM is shown that has been designed for the SiPM module with the electronics required to operate the device so that it could be tested for various overvoltages while blocking out ambient light. The SiPM pulses were recorded through a high bandwidth digital oscilloscope along with the START reference and then post processed using MATLAB scripts to perform TCSPC.

The noise in the detector, in the form of dark count rate and crosstalk, was measured and presented. The photon number resolving capabilities of the SiPM have been characterised for a range of overvoltages. The SiPM was tested with various low pass filtering frequencies which was observed to improve the peak to trough ratio of the various photon peaks when histogramming the SiPM pulse amplitude spectrum. TCSPC measurements were performed on the SiPM for various mean photon numbers with the detector found to be unable to resolve the waveform properly at the lowest mean photon number of 0.1, where a SPAD is typically operated at. This is due to the high dark count rate of the SiPM as it is a summed array of SPADs which also sums the dark count of each of the SPAD microcells. Finally, the various photon event levels for the SiPM were determined for the full range of overvoltage values to be used later when performing TCPC measurements.

Chapter 4 presents a novel instrument for performing TCPC measurements in real time. The main difference with TCSPC is the use of photon number resolving detectors such as the SiPM to infer the number of photons within any detector pulse. The instrument was developed on a Xilinx Artix7-200T FPGA platform with both the TDCs and TCPC logic block being implemented. Extra care was given to the clock source for the TDC to be as jitter free as possible. The

circuitry used to quantise the number of photons within a given pulse uses four high speed comparators (one for each photon level being measured) along with the photon thresholds found in chapter 3 to determine the number of photons within a pulse. Single shot circuitry is used within the FPGA to keep the current state of the comparators until the FPGA can encode the thermometer code from the comparators into a 2-bit amplitude vector. The 2 bit vector is then passed to the correlator logic where it is used to add the appropriate number of counts to a particular bin representing the measured ΔT.

The TDC used was measured to have a SSP of 45ps RMS along with a DNL of (-1, 9.18) and INL of (-2.33, 23.1). The hardware was tested by simulating various photon event levels to make sure the 2-bit amplitude vector was being used correctly in the histogram formation. The instrument was then used to perform both TCSPC (only 1 comparator channel active) on the SiPM and TCPC on the SiPM, with the results showing a clear gain in the count rates when using TCPC. Such flexibility also offers the potential for such instruments to have considerable commercial potential.

In chapter 5, the SiPM's performance is experimentally evaluated and compared to an iD100 SPAD. The first of the comparisons was regarding the excitation rates able to be used with the detectors with the two detectors using the same experimental setup. An increase of 140% was observed in the SiPM count rates for TCPC over TCSPC using the SPAD along with a 236% increase over the count rates of TCSPC using the SiPM. This confirms that there is a benefit in using TCPC with photon number resolving detectors.

The signal to noise ratios of each of the detectors was measured and presented with the SNR of the SPAD being a factor of 10 greater than the SNR of the SiPM. The SiPM is found to be unable to resolve waveforms at a mean photon number of 0.1, where the peak of correlation is at the same height as the noise floor. The SNR of the SiPM does see significant improvement as the mean photon number is increased allowing for the optical waveform to be resolved. The SNR of the SiPM does surpass that of the SPAD eventually but only at very high mean photon numbers where the detector was measured to go nonlinear. Finally, possible applications for TCPC are mentioned with photon absorption spectroscopy and imaging systems being the best potential route as the TCPC technique can provide a significant benefit when used with high light levels and is not suited for quantum applications like a SPAD.

M. Sadik, PhD, Thesis, Aston University, 2023

8.0 References

[1] PicoQuant, "Time-Correlated Single Photon Counting Technical Note," 28/06/2022 ed, 2014, p. https://www.picoquant.com/images/uploads/page/files/7253/technote_tcspc.pdf.

[2] D. Tamborini, M. Buttafava, A. Ruggeri, and F. Zappa, "Compact, Low-Power and Fully Reconfigurable 10 ps Resolution, 160 μs Range, Time-Resolved Single-Photon Counting System," *IEEE Sensors Journal,* vol. 16, no. 10, pp. 3827-3833, 2016, doi: 10.1109/JSEN.2016.2535403.

[3] A. Cuccato *et al.*, "Complete and Compact 32-Channel System for Time-Correlated Single-Photon Counting Measurements," *IEEE Photonics Journal,* vol. 5, no. 5, pp. 6801514-6801514, 2013, doi: 10.1109/JPHOT.2013.2284250.

[4] J. S. Massa, G. S. Buller, A. C. Walker, S. Cova, M. Umasuthan, and A. M. Wallace, "Time-of-flight optical ranging system based on time-correlated single-photon counting," *Applied Optics,* vol. 37, no. 31, pp. 7298-7304, 1998/11/01 1998, doi: 10.1364/AO.37.007298.

[5] W. Becker, "The bh TCSPC handbook," 9th ed, 2021.

[6] J. L. Duligall, M. S. Godfrey, K. A. Harrison, W. J. Munro, and J. G. Rarity, "Low cost and compact quantum key distribution," *New Journal of Physics,* vol. 8, no. 10, pp. 249-249, 2006/10/24 2006, doi: 10.1088/1367-2630/8/10/249.

[7] D. Stucki, N. Brunner, N. Gisin, V. Scarani, and H. Zbinden, "Fast and simple one-way quantum key distribution," *Applied Physics Letters,* vol. 87, no. 19, p. 194108, 2005/11/07 2005, doi: 10.1063/1.2126792.

[8] D. L. D. Lowndes, "Low cost, short range free space quantum cryptography for consumer applications: pocket size for pocket change," Doctor of Philosophy (PhD), Department of Electrical & Electronic Engineering, University of Bristol, 2014.

[9] D. Perenzoni, L. Gasparini, N. Massari, and D. Stoppa, "Depth-range extension with folding technique for SPAD-based TOF LIDAR systems," in *SENSORS, 2014 IEEE*, 2-5 Nov. 2014 2014, pp. 622-624, doi: 10.1109/ICSENS.2014.6985075.

[10] A. S. Yousif and J. W. Haslett, "A Fine Resolution TDC Architecture for Next Generation PET Imaging," *IEEE Transactions on Nuclear Science,* vol. 54, no. 5, pp. 1574-1582, 2007, doi: 10.1109/TNS.2007.903183.

[11] B. K. Swann *et al.*, "A 100-ps time-resolution CMOS time-to-digital converter for positron emission tomography imaging applications," *IEEE Journal of Solid-State Circuits,* vol. 39, no. 11, pp. 1839-1852, 2004, doi: 10.1109/JSSC.2004.835832.

[12] K. Muhammad *et al.*, "The First Fully Integrated Quad-Band GSM/GPRS Receiver in a 90-nm Digital CMOS Process," *IEEE Journal of Solid-State Circuits,* vol. 41, no. 8, pp. 1772-1783, 2006, doi: 10.1109/JSSC.2006.877271.

[13] B. Wolfgang *et al.*, "High resolution TCSPC lifetime imaging," in *Proc.SPIE*, 2003, vol. 4963, doi: 10.1117/12.472866. [Online]. Available: https://doi.org/10.1117/12.472866

[14] W. Becker, *Advanced Time- Correlated Single Photon Counting Applications*, 1 ed. (Springer Series in Chemical Physics). Springer Cham, 2015, p. 624.

[15] S. Brown and J. Rose, "FPGA and CPLD architectures: a tutorial," *IEEE Design & Test of Computers,* vol. 13, no. 2, pp. 42-57, 1996, doi: 10.1109/54.500200.

[16] J. Kalisz, "Review of methods for time interval measurements with picosecond resolution," *Metrologia,* vol. 41, no. 1, pp. 17-32, 2003/12/10 2003, doi: 10.1088/0026-1394/41/1/004.

[17] P. Keunoh and P. Jaehong, "20 ps resolution time-to-digital converter for digital storage oscilloscopes," in *1998 IEEE Nuclear Science Symposium Conference Record. 1998 IEEE Nuclear Science Symposium and Medical Imaging Conference (Cat. No.98CH36255)*, 8-14 Nov. 1998 1998, vol. 2, pp. 876-881 vol.2, doi: 10.1109/NSSMIC.1998.774310.

[18] P. Chen, C. C. Chen, and Y. S. Shen, "A Low-Cost Low-Power CMOS Time-to-Digital Converter Based on Pulse Stretching," *IEEE Transactions on Nuclear Science,* vol. 53, no. 4, pp. 2215-2220, 2006, doi: 10.1109/TNS.2006.876051.

[19] S. Shin and H. J. Yoo, "A pipelined time stretching for high throughput counter-based time-to-digital converters," in *2016 International SoC Design Conference (ISOCC)*, 23-26 Oct. 2016 2016, pp. 57-58, doi: 10.1109/ISOCC.2016.7799706.

[20] M. Kanoun, Y. Berube-Lauziere, and R. Fontaine, "High precision time-to-amplitude converter for diffuse optical tomography applications," in *2008 3rd International Conference on Design and Technology of Integrated Systems in Nanoscale Era*, 25-27 March 2008 2008, pp. 1-4, doi: 10.1109/DTIS.2008.4540240.

[21] M. Crotti, I. Rech, and M. Ghioni, "Monolithic Time-to-Amplitude converter for TCSPC applications with 45 ps time resolution," in *2011 7th Conference on Ph.D. Research in Microelectronics and Electronics*, 3-7 July 2011 2011, pp. 21-24, doi: 10.1109/PRIME.2011.5966206.

[22] W. Yonggang, L. Chong, and Z. Wensong, "Two novel designs of multi-phase clocked ultra-high speed time counter on FPGA for TDC implementation," in *2013 IEEE Nuclear Science Symposium and Medical Imaging Conference (2013 NSS/MIC)*, 27 Oct.-2 Nov. 2013 2013, pp. 1-4, doi: 10.1109/NSSMIC.2013.6829534.

[23] A. M. Amiri, A. Khouas, and M. Boukadoum, "On the Timing Uncertainty in Delay-Line-based Time Measurement Applications Targeting FPGAs," in *2007 IEEE International Symposium on Circuits and Systems*, 27-30 May 2007 2007, pp. 3772-3775, doi: 10.1109/ISCAS.2007.378782.

[24] M. Palka *et al.*, "A novel method based solely on FPGA units enabling measurement of time and charge of analog signals in Positron Emission Tomography," *Bio-Algorithms and Med-Systems,* vol. 10, 11/24 2013, doi: 10.1515/bams-2013-0104.

[25] X. Qin *et al.*, "A high resolution time-to-digital-convertor based on a carry-chain and DSP48E1 adders in a 28-nm field-programmable-gate-array," *Review of Scientific Instruments,* vol. 91, no. 2, p. 024708, 2020/02/01 2020, doi: 10.1063/1.5141391.

[26] X. Qin, L. Wang, D. Liu, Y. Zhao, X. Rong, and J. Du, "A 1.15-ps Bin Size and 3.5-ps Single-Shot Precision Time-to-Digital Converter With On-Board Offset Correction in an FPGA," *IEEE Transactions on Nuclear Science,* vol. 64, no. 12, pp. 2951-2957, 2017, doi: 10.1109/TNS.2017.2768082.

[27] E. Bayer, P. Zipf, and M. Traxler, "A multichannel high-resolution (<5 ps RMS between two channels) Time-to-Digital Converter (TDC) implemented in a field programmable gate array (FPGA)," in *2011 IEEE Nuclear Science Symposium Conference Record*, 23-29 Oct. 2011 2011, pp. 876-879, doi: 10.1109/NSSMIC.2011.6154560.

[28] Y. Jia, M. Xu, and J. Kang, "Research of high precision time interval measurement base on carry chain," in *Proceedings 2013 International Conference on Mechatronic Sciences, Electric Engineering and Computer (MEC)*, 20-22 Dec. 2013 2013, pp. 742-745, doi: 10.1109/MEC.2013.6885160.

[29] S. Guo, Y. Wang, N. Li, J. Diao, and L. Chen, "Multi-chain time interval measurement method utilizing the dedicated carry chain of FPGA," in *2017 7th IEEE International Conference on Electronics Information and Emergency Communication (ICEIEC)*, 21-23 July 2017 2017, pp. 489-492, doi: 10.1109/ICEIEC.2017.8076612.

[30] M. Parsakordasiabi, I. Vornicu, R.-V. Á, and R. Carmona-Galán, "An Efficient TDC Using a Dual-Mode Resource-Saving Method Evaluated in a 28-nm FPGA," *IEEE Transactions on Instrumentation and Measurement,* vol. 71, pp. 1-13, 2022, doi: 10.1109/TIM.2021.3136267.

[31] S. S. Junnarkar, M. Purschke, J. F. Pratte, P. Sang-June, P. O. Connor, and R. Fontaine, "An FPGA-based, 12-channel TDC and digital signal processing module for the RatCAP scanner," in *IEEE Nuclear Science Symposium Conference Record, 2005*, 23-29 Oct. 2005 2005, vol. 2, pp. 919-923, doi: 10.1109/NSSMIC.2005.1596404.

M. Sadik, PhD, Thesis, Aston University, 2023

[32]   S. Jian, A. Qi, and L. Shubin, "A high-resolution time-to-digital converter implemented in field-programmable-gate-arrays," *IEEE Transactions on Nuclear Science,* vol. 53, no. 1, pp. 236-241, 2006, doi: 10.1109/TNS.2006.869820.

[33]   J. Wu and Z. Shi, "The 10-ps wave union TDC: Improving FPGA TDC resolution beyond its cell delay," in *2008 IEEE Nuclear Science Symposium Conference Record*, 19-25 Oct. 2008 2008, pp. 3440-3446, doi: 10.1109/NSSMIC.2008.4775079.

[34]   A. Aloisio, P. Branchini, R. Cicalese, R. Giordano, V. Izzo, and S. Loffredo, "FPGA implementation of a high-resolution time-to-digital converter," in *2007 IEEE Nuclear Science Symposium Conference Record*, 26 Oct.-3 Nov. 2007 2007, vol. 1, pp. 504-507, doi: 10.1109/NSSMIC.2007.4436379.

[35]   M. Perenzoni, L. Gasparini, and D. Stoppa, "Design and Characterization of a 43.2-ps and PVT-Resilient TDC for Single-Photon Imaging Arrays," *IEEE Transactions on Circuits and Systems II: Express Briefs,* vol. 65, no. 4, pp. 411-415, 2018, doi: 10.1109/TCSII.2017.2694482.

[36]   A. Annagrebah, E. Bechetoille, H. Chanal, H. Mathez, and I. Laktineh, "Time-To-Digital Converter with adjustable resolution using a digital Vernier Ring Oscillator," in *2018 Conference on Design of Circuits and Integrated Systems (DCIS)*, 14-16 Nov. 2018 2018, pp. 1-4, doi: 10.1109/DCIS.2018.8681494.

[37]   P. Chen, J. Lai, and Y. Chen, "FPGA Vernier Digital-to-Time Converter With 1.58 ps Resolution and 59.3 Minutes Operation Range," *IEEE Transactions on Circuits and Systems I: Regular Papers,* vol. 57, no. 6, pp. 1134-1142, 2010, doi: 10.1109/TCSI.2009.2028748.

[38]   R. Nutt, "Digital Time Intervalometer," *Review of Scientific Instruments,* vol. 39, no. 9, pp. 1342-1345, 1968/09/01 1968, doi: 10.1063/1.1683667.

[39]   K. Cui, Z. Liu, R. Zhu, and X. Li, "FPGA-based high-performance time-to-digital converters by utilizing multi-channels looped carry chains," in *2017 International Conference on Field Programmable Technology (ICFPT)*, 11-13 Dec. 2017 2017, pp. 223-226, doi: 10.1109/FPT.2017.8280146.

[40]   MaximIntegrated, "The ABCs of Analog to Digital Converters: How ADC Errors Affect System Performance," 29/09/2022 ed, pp. https://www.maximintegrated.com/en/design/technical-documents/tutorials/7/748.html.

[41]   F. Villa *et al.*, "SPAD Smart Pixel for Time-of-Flight and Time-Correlated Single-Photon Counting Measurements," *IEEE Photonics Journal,* vol. 4, no. 3, pp. 795-804, 2012, doi: 10.1109/JPHOT.2012.2198459.

[42]   M. G. C. Flores, M. Negreiros, L. Carro, and A. A. Susin, "INL and DNL estimation based on noise for ADC test," *IEEE Transactions on Instrumentation and Measurement,* vol. 53, no. 5, pp. 1391-1395, 2004, doi: 10.1109/TIM.2004.834096.

[43]   S. Cherubal and A. Chatterjee, "Optimal INL/DNL testing of A/D converters using a linear model," in *Proceedings International Test Conference 2000 (IEEE Cat. No.00CH37159)*, 3-5 Oct. 2000 2000, pp. 358-366, doi: 10.1109/TEST.2000.894225.

[44]   MaximIntegrated, "HISTOGRAM TESTING DETERMINES DNL AND INL ERRORS," ed, 2003.

[45]   P. Eckert, H.-C. Schultz-Coulon, W. Shen, R. Stamen, and A. Tadday, "Characterisation studies of silicon photomultipliers," *Nuclear Instruments and Methods in Physics Research Section A: Accelerators, Spectrometers, Detectors and Associated Equipment,* vol. 620, no. 2, pp. 217-226, 2010/08/11/ 2010, doi: https://doi.org/10.1016/j.nima.2010.03.169.

[46]   M. Mota and J. Christiansen, "A high-resolution time interpolator based on a delay locked loop and an RC delay line," *IEEE Journal of Solid-State Circuits,* vol. 34, no. 10, pp. 1360-1366, 1999, doi: 10.1109/4.792603.

[47]   Q. Shen *et al.*, "A multi-chain measurements averaging TDC implemented in a 40 nm FPGA," in *2014 19th IEEE-NPSS Real Time Conference*, 26-30 May 2014 2014, pp. 1-3, doi: 10.1109/RTC.2014.7097550.

M. Sadik, PhD, Thesis, Aston University, 2023

[48] P. Chen, Y. Hsiao, and Y. Chung, "A high resolution FPGA TDC converter with 2.5 ps bin size and −3.79~6.53 LSB integral nonlinearity," in *2016 2nd International Conference on Intelligent Green Building and Smart Grid (IGBSG)*, 27-29 June 2016 2016, pp. 1-5, doi: 10.1109/IGBSG.2016.7539437.

[49] J. Wang, S. Liu, L. Zhao, X. Hu, and Q. An, "The 10-ps Multitime Measurements Averaging TDC Implemented in an FPGA," *IEEE Transactions on Nuclear Science,* vol. 58, no. 4, pp. 2011-2018, 2011, doi: 10.1109/TNS.2011.2158551.

[50] R. Szplet, Z. Jachna, P. Kwiatkowski, and K. Rozyc, "A 2.9 ps equivalent resolution interpolating time counter based on multiple independent coding lines," *Measurement Science and Technology,* vol. 24, no. 3, p. 035904, 2013/02/19 2013, doi: 10.1088/0957-0233/24/3/035904.

[51] P. Kwiatkowski and R. Szplet, "Efficient Implementation of Multiple Time Coding Lines-Based TDC in an FPGA Device," *IEEE Transactions on Instrumentation and Measurement,* vol. 69, no. 10, pp. 7353-7364, 2020, doi: 10.1109/TIM.2020.2984929.

[52] A. McCarthy, R. J. Collins, N. J. Krichel, V. Fernández, A. M. Wallace, and G. S. Buller, "Long-range time-of-flight scanning sensor based on high-speed time-correlated single-photon counting," *Applied Optics,* vol. 48, no. 32, pp. 6241-6251, 2009/11/10 2009, doi: 10.1364/AO.48.006241.

[53] J. Bouchard *et al.*, "A Low-Cost Time-Correlated Single Photon Counting System for Multiview Time-Domain Diffuse Optical Tomography," *IEEE Transactions on Instrumentation and Measurement,* vol. 66, no. 10, pp. 2505-2515, 2017, doi: 10.1109/TIM.2017.2666458.

[54] P. Poulet, C.-V. Zint, M. Torregrossa, W. Uhring, and B. Cunin, "Comparison of two time-resolved detectors for diffuse optical tomography: photomultiplier tube--time-correlated single photon counting and multichannel streak camera," *Proc SPIE,* pp. 154-163, 07/01 2003, doi: 10.1117/12.476841.

[55] A. C. Ulku *et al.*, "A 512 × 512 SPAD Image Sensor With Integrated Gating for Widefield FLIM," *IEEE Journal of Selected Topics in Quantum Electronics,* vol. 25, no. 1, pp. 1-12, 2019, doi: 10.1109/JSTQE.2018.2867439.

[56] P. M. Wargocki *et al.*, "Imaging free and bound NADH towards cancer tissue detection using FLIM system based on SPAD array," in *2017 Conference on Lasers and Electro-Optics Europe & European Quantum Electronics Conference (CLEO/Europe-EQEC)*, 25-29 June 2017 2017, pp. 1-1, doi: 10.1109/CLEOE-EQEC.2017.8087784.

[57] A. Incoronato, M. Locatelli, and F. Zappa, "Statistical Model for SPAD-based Time-of-Flight systems and photons pile-up correction," in *2021 Conference on Lasers and Electro-Optics Europe & European Quantum Electronics Conference (CLEO/Europe-EQEC)*, 21-25 June 2021 2021, pp. 1-1, doi: 10.1109/CLEO/Europe-EQEC52157.2021.9541645.

[58] P. B. Coates, "The correction for photon `pile-up' in the measurement of radiative lifetimes," *Journal of Physics E: Scientific Instruments,* vol. 1, no. 8, pp. 878-879, 1968/08 1968, doi: 10.1088/0022-3735/1/8/437.

[59] D. E. Schwartz, E. Charbon, and K. L. Shepard, "A Single-Photon Avalanche Diode Array for Fluorescence Lifetime Imaging Microscopy," (in eng), *IEEE J Solid-State Circuits,* vol. 43, no. 11, pp. 2546-2557, Nov 21 2008, doi: 10.1109/jssc.2008.2005818.

[60] IDQuantique, "ID100 Visible Single-Photon Detector," 28/06/2022 ed, 2020, pp. https://marketing.idquantique.com/acton/attachment/11868/f-0236/1/-/-/-/-/ID100_Brochure.pdf.

[61] L. Turgeman and D. Fixler, "Photon Efficiency Optimization in Time-Correlated Single Photon Counting Technique for Fluorescence Lifetime Imaging Systems," *IEEE Transactions on Biomedical Engineering,* vol. 60, no. 6, pp. 1571-1579, 2013, doi: 10.1109/TBME.2013.2238671.

[62] S. Thomson, "Technical Note: Avoiding Dead Time Losses with Reverse Mode TCSPC in the FLS1000," E. Instruments, Ed., ed, 2021.

[63] R. W. Nock, "Flexible precision timing instrumentation and quantum key distribution," University of Bristol, 2013. [Online]. Available: https://ethos.bl.uk/OrderDetails.do?uin=uk.bl.ethos.658313

[64] D. Xiao, N. Sapermsap, M. Safar, M. R. Cunningham, Y. Chen, and D. D. U. Li, "On Synthetic Instrument Response Functions of Time-Correlated Single-Photon Counting Based Fluorescence Lifetime Imaging Analysis," *Frontiers in Physics,* Original Research vol. 9, 2021.

[65] C. Chunnilall, I. Degiovanni, S. Kück, I. Müller, and A. Sinclair, "Metrology of single-photon sources and detectors: A review," *Optical Engineering,* vol. 53, p. 081910, 08/01 2014, doi: 10.1117/1.OE.53.8.081910.

[66] Y. Liang and H. Zeng, "Single-photon detection and its applications," *Science China Physics, Mechanics & Astronomy,* vol. 57, no. 7, pp. 1218-1232, 2014/07/01 2014, doi: 10.1007/s11433-014-5450-0.

[67] I. Rech *et al.*, "Optical crosstalk in single photon avalanche diode arrays: a new complete model," *Optics Express,* vol. 16, no. 12, pp. 8381-8394, 2008/06/09 2008, doi: 10.1364/OE.16.008381.

[68] onsemi, "Introduction to the Silicon Photomultiplier (SiPM), AND9770/D," ed, 2011.

[69] B. K. Lubsandorzhiev, "On the history of photomultiplier tube invention," *Nuclear Instruments and Methods in Physics Research Section A: Accelerators, Spectrometers, Detectors and Associated Equipment,* vol. 567, no. 1, pp. 236-238, 2006/11/01/ 2006, doi: https://doi.org/10.1016/j.nima.2006.05.221.

[70] J. Xia *et al.*, "A performance evaluation system for photomultiplier tubes," *Journal of Instrumentation,* vol. 10, no. 03, pp. P03023-P03023, 2015/03/23 2015, doi: 10.1088/1748-0221/10/03/p03023.

[71] S. Donati and T. Tambosso, "Single-Photon Detectors: From Traditional PMT to Solid-State SPAD-Based Technology," *IEEE Journal of Selected Topics in Quantum Electronics,* vol. 20, no. 6, pp. 204-211, 2014, doi: 10.1109/JSTQE.2014.2350836.

[72] C. Bruschini *et al.*, "Monolithic SPAD Arrays for High-Performance, Time-Resolved Single-Photon Imaging," in *2018 International Conference on Optical MEMS and Nanophotonics (OMN)*, 29 July-2 Aug. 2018 2018, pp. 1-5, doi: 10.1109/OMN.2018.8454654.

[73] M. A. Itzler, X. Jiang, R. Ben-Michael, B. Nyman, and K. Slomkowski, "Geiger-Mode APD Single Photon Detectors," in *OFC/NFOEC 2008 - 2008 Conference on Optical Fiber Communication/National Fiber Optic Engineers Conference*, 24-28 Feb. 2008 2008, pp. 1-3, doi: 10.1109/OFC.2008.4528353.

[74] A. Gallivanoni, I. Rech, and M. Ghioni, "Progress in Quenching Circuits for Single Photon Avalanche Diodes," *IEEE Transactions on Nuclear Science,* vol. 57, no. 6, pp. 3815-3826, 2010, doi: 10.1109/TNS.2010.2074213.

[75] S. Cova, M. Ghioni, A. Lacaita, C. Samori, and F. Zappa, "Avalanche photodiodes and quenching circuits for single-photon detection," *Applied Optics,* vol. 35, no. 12, pp. 1956-1976, 1996/04/20 1996, doi: 10.1364/AO.35.001956.

[76] F. Nolet *et al.*, "Quenching Circuit and SPAD Integrated in CMOS 65 nm with 7.8 ps FWHM Single Photon Timing Resolution," *Instruments,* vol. 2, p. 19, 09/22 2018, doi: 10.3390/instruments2040019.

[77] V. Savuskan, M. Javitt, G. Visokolov, I. Brouk, and Y. Nemirovsky, "Selecting Single Photon Avalanche Diode (SPAD) Passive-Quenching Resistance: An Approach," *IEEE Sensors Journal,* vol. 13, no. 6, pp. 2322-2328, 2013, doi: 10.1109/JSEN.2013.2253603.

[78] D. Silvano, "Avalanche Photodiode, SPAD, and SiPM," in *Photodetectors: Devices, Circuits and Applications*: IEEE, 2021, pp. 175-220.

[79] onsemi, "Silicon Photomultipliers (SiPM), Red-Enhanced Second Generation RB-Series SiPM Sensors," ed, 2018.

[80] onsemi, "Silicon Photomultipliers (SiPM), Low-Noise, Blue-Sensitive C-Series SiPM Sensors," ed, 2014.

[81] T. Xu *et al.*, "Design and initial performance evaluation of a novel PET detector module based on compact SiPM arrays," in *2011 IEEE Nuclear Science Symposium Conference Record*, 23-29 Oct. 2011 2011, pp. 3038-3041, doi: 10.1109/NSSMIC.2011.6152548.

[82] M. Tétrault, A. C. Therrien, W. Lemaire, R. Fontaine, and J. Pratte, "TDC Array Tradeoffs in Current and Upcoming Digital SiPM Detectors for Time-of-Flight PET," *IEEE Transactions on Nuclear Science,* vol. 64, no. 3, pp. 925-932, 2017, doi: 10.1109/TNS.2017.2665878.

[83] M. Caccia, L. Nardo, R. Santoro, and D. Schaffhauser, "Silicon Photomultipliers and SPAD imagers in biophotonics: Advances and perspectives," *Nuclear Instruments and Methods in Physics Research Section A: Accelerators, Spectrometers, Detectors and Associated Equipment,* vol. 926, pp. 101-117, 2019/05/11/ 2019, doi: https://doi.org/10.1016/j.nima.2018.10.204.

[84] S. Dolinsky, G. Fu, and A. Ivan, "Timing resolution performance comparison for fast and standard outputs of SensL SiPM," in *2013 IEEE Nuclear Science Symposium and Medical Imaging Conference (2013 NSS/MIC)*, 27 Oct.-2 Nov. 2013 2013, pp. 1-6, doi: 10.1109/NSSMIC.2013.6829520.

[85] onsemi, "Biasing and Readout of ON Semiconductor SiPM Sensors AND9782/D," ed, 2018.

[86] P. Eraerds, M. Legré, A. Rochas, H. Zbinden, and N. Gisin, "SiPM for fast Photon-Counting and Multiphoton Detection," *Optics Express,* vol. 15, no. 22, pp. 14539-14549, 2007/10/29 2007, doi: 10.1364/OE.15.014539.

[87] L. Baicheng *et al.*, "Time-Correlated Photon Counting (TCPC) technique based on a photon-number-resolving photodetector," in *Proc.SPIE*, 2016, vol. 9858, doi: 10.1117/12.2222962. [Online]. Available: https://doi.org/10.1117/12.2222962

[88] S. Grollius, M. Ligges, J. Ruskowski, and A. Grabmaier, "Concept of an Automotive LiDAR Target Simulator for Direct Time-of-Flight LiDAR," *IEEE Transactions on Intelligent Vehicles,* pp. 1-1, 2021, doi: 10.1109/TIV.2021.3128808.

[89] J. Liu, Q. Sun, Z. Fan, and Y. Jia, "TOF Lidar Development in Autonomous Vehicle," in *2018 IEEE 3rd Optoelectronics Global Conference (OGC)*, 4-7 Sept. 2018 2018, pp. 185-190, doi: 10.1109/OGC.2018.8529992.

[90] G. Zhou, X. Zhou, J. Yang, Y. Tao, X. Nong, and O. Baysal, "Flash Lidar Sensor Using Fiber-Coupled APDs," *IEEE Sensors Journal,* vol. 15, no. 9, pp. 4758-4768, 2015, doi: 10.1109/JSEN.2015.2425414.

[91] D. Wang, C. Watkins, and H. Xie, "MEMS Mirrors for LiDAR: A Review," *Micromachines,* vol. 11, no. 5, 2020, doi: 10.3390/mi11050456.

[92] H. Yoo *et al.*, "MEMS-based lidar for autonomous driving," *e & i Elektrotechnik und Informationstechnik,* 07/31 2018, doi: 10.1007/s00502-018-0635-2.

[93] X. Zhang, R. Zhang, S. Koppal, L. Butler, X. Cheng, and H. Xie, "MEMS mirrors submerged in liquid for wide-angle scanning," in *2015 Transducers - 2015 18th International Conference on Solid-State Sensors, Actuators and Microsystems (TRANSDUCERS)*, 21-25 June 2015 2015, pp. 847-850, doi: 10.1109/TRANSDUCERS.2015.7181056.

[94] X. Zhang *et al.*, "A wide-angle immersed MEMS mirror and its application in optical coherence tomography," in *2016 International Conference on Optical MEMS and Nanophotonics (OMN)*, 31 July-4 Aug. 2016 2016, pp. 1-2, doi: 10.1109/OMN.2016.7565908.

[95] D. Mikel, R. Merrill, J. Colby, T. Footer, P. Crawford, and L. Alvarez-Aviles, *EPA Handbook: Optical Remote Sensing for Measurement and Monitoring of Emissions Flux*. 2011.

[96] B. Bundschuh, H. Richter, D. Althausen, D. Müller, and A. Ansmann, "On the Calculation of Received Power for LIDAR Imaging Systems," 01/01 1998.

[97] S. Banzhaf and C. Waldschmidt, "Phase-Coded FMCW Lidar," in *2021 29th European Signal Processing Conference (EUSIPCO)*, 23-27 Aug. 2021 2021, pp. 1775-1779, doi: 10.23919/EUSIPCO54536.2021.9616043.

M. Sadik, PhD, Thesis, Aston University, 2023

[98]   W. Gaughan and B. Butka, "Using an FPGA digital clock manager to generate sub-nanosecond phase shifts for lidar applications," in *2010 VI Southern Programmable Logic Conference (SPL)*, 24-26 March 2010 2010, pp. 163-166, doi: 10.1109/SPL.2010.5483021.

[99]   S. Gao and M. D. Xiong, "A New Approach to Improve the Performance of Phase Laser Range Finder," *Journal of Physics: Conference Series,* vol. 48, pp. 838-842, 2006/10/01 2006, doi: 10.1088/1742-6596/48/1/159.

[100]   L. Zhou, H. He, J. Sun, and B. Lin, "Phase-Shift Laser Ranging Technology Based on Multi-Frequency Carrier Phase Modulation," *Photonics*, vol. 9, no. 9*,* doi: 10.3390/photonics9090603.

[101]   G. Buller and A. Wallace, "Ranging and Three-Dimensional Imaging Using Time-Correlated Single-Photon Counting and Point-by-Point Acquisition," *IEEE Journal of Selected Topics in Quantum Electronics,* vol. 13, no. 4, pp. 1006-1015, 2007, doi: 10.1109/JSTQE.2007.902850.

[102]   Y. Liang *et al.*, "1550-nm time-of-flight ranging system employing laser with multiple repetition rates for reducing the range ambiguity," *Optics Express,* vol. 22, no. 4, pp. 4662-4670, 2014/02/24 2014, doi: 10.1364/OE.22.004662.

[103]   B. Du *et al.*, "High-speed photon-counting laser ranging for broad range of distances," *Scientific Reports,* vol. 8, no. 1, p. 4198, 2018/03/08 2018, doi: 10.1038/s41598-018-22675-1.

[104]   Y. Yu, B. Liu, Z. Chen, and Z. Li, "A Macro-Pulse Photon Counting Lidar for Long-Range High-Speed Moving Target Detection," *Sensors,* vol. 20, no. 8, 2020, doi: 10.3390/s20082204.

[105]   N. Takeuchi, N. Sugimoto, H. Baba, and K. Sakurai, "Random modulation cw lidar," *Applied Optics,* vol. 22, no. 9, pp. 1382-1386, 1983/05/01 1983, doi: 10.1364/AO.22.001382.

[106]   Tektronix, "MDO4000C Series Datasheet," ed, 2021.

[107]   Thorlabs, "PAF2-2A-Manual," 29/09/2022 ed, pp. https://www.thorlabs.com/_sd.cfm?fileName=TTN132194-D02.pdf&partNumber=PAF2-2A.

[108]   AnalogDevices, "LT3014B: 20mA, 3V to 80V Low Dropout Micropower Linear Regulator Data Sheet," 28/09/2022 ed, pp. https://www.analog.com/media/en/technical-documentation/data-sheets/3014bfb.pdf.

[109]   Mini-Circuits, "ZFL-1000LN+ Low Noise Amplifier, 0.1 - 1000 MHz, 50Ω," 28/09/2022 ed, pp. https://www.minicircuits.com/pdfs/ZFL-1000LN+.pdf.

[110]   F. Acerbi and S. Gundacker, "Understanding and simulating SiPMs," *Nuclear Instruments and Methods in Physics Research Section A: Accelerators, Spectrometers, Detectors and Associated Equipment,* vol. 926, pp. 16-35, 2019/05/11/ 2019, doi: https://doi.org/10.1016/j.nima.2018.11.118.

[111]   Thorlabs, "LPM-635-SMA - 635 nm, 7.5 mW, A Pin Code, Ø62.5 µm MM Fiber-Pigtailed Laser Diode, SMA905," 29/09/2022 ed, 2004, pp. https://www.thorlabs.com/_sd.cfm?fileName=5398-S01.pdf&partNumber=LPM-635-SMA.

[112]   iC-Haus, "iC-HS Series Ultra Short Pulse Laser Drivers," 29/09/2022 ed, p. https://www.ichaus.de/HS_factsheet_en.

[113]   Thorlabs, "FBP-A-FC - Adjustable Fiber-to-Fiber Coupler, 350 - 700 nm, FC/PC or FC/APC," 29/09/2022 ed, pp. https://www.thorlabs.com/thorproduct.cfm?partnumber=FBP-A-FC.

[114]   Thorlabs, "NEK02 - Box with 12 Absorptive Ø1/2" ND Filters, SM05-Mounted, 400 - 650 nm," 28/09/2022 ed, p. https://www.thorlabs.com/thorproduct.cfm?partnumber=NEK02.

[115]   A. Pediredla, A. Sankaranarayanan, M. Buttafava, A. Tosi, and A. Veeraraghavan, *Signal Processing Based Pile-up Compensation for Gated Single-Photon Avalanche Diodes*. 2018.

[116]   Xilinx, "Digital Clock Manager (DCM) Module Data Sheet(DS485)," ed, 2009.

M. Sadik, PhD, Thesis, Aston University, 2023

[117]   Renesas, "PCI Express™ Jitter Attenuator ICS874001I-05," 28/09/2022 ed, 2011, pp. https://www.renesas.com/us/en/document/dst/ics874001i-05-datasheet.

[118]   AnalogDevices, "ADCMP604/ADCMP605: Rail-to-Rail, Very Fast, 2.5 V to 5.5 V, Single-Supply LVDS Comparators Data Sheet (Rev. C)," 29/09/2022 ed, pp. https://www.analog.com/media/en/technical-documentation/data-sheets/ADCMP604_605.pdf.

[119]   Mini-Circuits, "ZFRSC-42-S+ 2 Ways Resistive Power Splitter, DC - 4200 MHz, 50Ω," 28/09/2022 ed, pp. https://www.minicircuits.com/pdfs/ZFRSC-42+.pdf.

[120]   H. Lim, "Constant Fraction Discriminator Involving Automatic Gain Control to Reduce Time Walk," *IEEE Transactions on Nuclear Science,* vol. 61, no. 4, pp. 2351-2356, 2014, doi: 10.1109/TNS.2014.2339362.

[121]   K. Linga, Y. Yevtukhov, and B. Liang, "Very high gain and low excess noise near infrared single photon avalanche detector: A NIR solid state photomultiplier," *Proceedings of SPIE - The International Society for Optical Engineering,* vol. 7320, 05/01 2009, doi: 10.1117/12.818580.

[122]   Weeroc, "Citiroc 1A - Scientific instrumentation SiPM read-out chip," 30/06/2022 ed, 2022, pp. https://www.weeroc.com/my-weeroc/download-center/citiroc-1a/16-citiroc1a-datasheet-v2-5.

M. Sadik, PhD, Thesis, Aston University, 2023